

Little Red Dots: One Photometric Tag Concealing Diverse Spectroscopic Flavors of Massive Star Formation and Black Hole Activity

PABLO G. PÉREZ-GONZÁLEZ ¹, GUILLERMO BARRO ², STEFANO CARNIANI ³, FRANCESCO D'EUGENIO ^{4,5},
GEORGE H. RIEKE ⁶, ROBERTA TRIPODI ⁷, ANDREW J. BUNKER ⁸, XIHAN JI ^{4,5}, RUI MARQUES-CHAVES ⁹,
DANIEL SCHAEER ⁹, GIACOMO VENTURI ³, FLOR ARÉVALO-GONZÁLEZ ⁷, SANTIAGO ARRIBAS ¹,
PIERLUIGI RINALDI ¹⁰, BRUNO RODRÍGUEZ DEL PINO ¹, JORIS WITSTOK ^{11,12}, RACHANA BHATAWDEKAR ¹³,
LEINDERT A. BOOGAARD ¹⁴, STEPHANE CHARLOT ¹⁵, JACOPO CHEVALLARD ⁸, LUCA COSTANTIN ¹,
MIRKO CURTI ¹⁶, EMMA CURTIS-LAKE ¹⁷, EMANUELE DADDI ¹⁸, KELCEY DAVIS ^{19,20}, MARK DICKINSON ²¹,
CALLUM T. DONNAN ²², FERGUS R. DONNAN ²³, JAMES S. DUNLOP ²⁴, DANIEL J. EISENSTEIN ²⁵,
HENRY C. FERGUSON ²⁶, ROMÁN FERNÁNDEZ ARANDA ¹, STEVEN L. FINKELSTEIN ^{27,28}, SEIJI FUJIMOTO ^{29,30},
GIOVANNI GANDOLFI ⁷, MAURO GIAVALISCO ³¹, NORMAN A. GROGIN ²⁶, MAHMOUD HAMED ¹,
MICHAELA HIRSCHMANN ³², JEYHAN S. KARTALTEPE ³³, DALE D. KOCEVSKI ³⁴, ANTON M. KOEKEMOER ¹⁰,
GENE C. K. LEUNG ³⁵, CRISTINA M. LOFARO ^{36,37}, RAY A. LUCAS ³⁸, DEREK J. MCLEOD ²⁴, JENS MELINDER ³⁹,
GÖRAN ÖSTLIN ³⁹, CASEY PAPOVICH ^{40,41}, LAURA PENTERICCI ⁴², BORJA PÉREZ-DÍAZ ⁷, MARCIA RIEKE ⁶,
JAN SCHOLTZ ^{4,5}, RACHEL S. SOMERVILLE ⁴³, THOMAS M. STANTON ²⁴, STRUAN D. STEVENSON ²⁴,
IRENE SHIVAEI ¹, SANDRO TACHELLA ^{4,5}, JONATHAN R. TRUMP ¹⁹, HANNAH ÜBLER ⁴⁴, XIN WANG ^{45,46,47},
CHRISTINA C. WILLIAMS ⁴⁸, CHRISTOPHER N. A. WILLMER ⁶, L. Y. AARON YUNG ³⁸ AND YONGDA ZHU ⁶

¹Centro de Astrobiología (CAB), CSIC-INTA, Ctra. de Ajalvir km 4, Torrejón de Ardoz, E-28850, Madrid, Spain

²University of the Pacific, Stockton, CA 90340 USA

³Scuola Normale Superiore, Piazza dei Cavalieri 7, I-56126 Pisa, Italy

⁴Kavli Institute for Cosmology, University of Cambridge, Madingley Road, Cambridge, CB3 0HA, UK

⁵Cavendish Laboratory, University of Cambridge, 19 JJ Thomson Avenue, Cambridge, CB3 0HE, UK

⁶Steward Observatory, University of Arizona, 933 North Cherry Avenue, Tucson, AZ 85721, USA

⁷INAF – Osservatorio Astronomico di Roma, via Frascati 33, 00078, Monteporzio Catone, Italy

⁸Department of Physics, University of Oxford, Denys Wilkinson Building, Keble Road, Oxford OX1 3RH, UK

⁹Department of Astronomy, University of Geneva, 51 Chemin Pegasi, 1290, Versoix, Switzerland

¹⁰Space Telescope Science Institute, 3700 San Martin Drive, Baltimore, Maryland 21218, USA

¹¹Cosmic Dawn Center (DAWN), Copenhagen, Denmark

¹²Niels Bohr Institute, University of Copenhagen, Jagtvej 128, DK-2200, Copenhagen, Denmark

¹³European Space Agency (ESA), European Space Astronomy Centre (ESAC), Camino Bajo del Castillo s/n, 28692 Villanueva de la Cañada, Madrid, Spain

¹⁴Leiden Observatory, Leiden University, PO Box 9513, NL-2300 RA Leiden, The Netherlands

¹⁵Sorbonne Université, CNRS, UMR 7095, Institut d'Astrophysique de Paris, 98 bis bd Arago, 75014 Paris, France

¹⁶European Southern Observatory, Karl-Schwarzschild-Strasse 2, 85748 Garching, Germany

¹⁷Centre for Astrophysics Research, Department of Physics, Astronomy and Mathematics, University of Hertfordshire, Hatfield AL10 9AB, UK

¹⁸CEA, IRFU, DAp, AIM, Université Paris-Saclay, Université Paris Cité, Sorbonne Paris Cité, CNRS, 91191 Gif-sur-Yvette, France

¹⁹Department of Physics, 196A Auditorium Road, Unit 3046, University of Connecticut, Storrs, CT 06269, USA

²⁰Los Alamos National Laboratory, Los Alamos, NM 87545, USA

²¹NSF National Optical-Infrared Astronomy Research Laboratory, 950 North Cherry Ave., Tucson, AZ 85719, USA

²²NSF's National Optical-Infrared Astronomy Research Laboratory, 950 North Cherry Ave., Tucson, AZ 85719, USA

²³Department of Astrophysics, University of California San Diego, 9500 Gilman Drive, San Diego, CA 92093, USA

²⁴Institute for Astronomy, University of Edinburgh, Royal Observatory, Edinburgh, EH9 3HJ, UK

²⁵Center for Astrophysics | Harvard & Smithsonian, 60 Garden St., Cambridge MA 02138 USA

²⁶Space Telescope Science Institute, Baltimore, MD, USA

²⁷Department of Astronomy, The University of Texas at Austin, Austin, TX, USA

²⁸Cosmic Frontier Center, The University of Texas at Austin, Austin, TX, USA

²⁹David A. Dunlap Department of Astronomy and Astrophysics, University of Toronto, 50 St. George Street, Toronto, Ontario, M5S 3H4, Canada

³⁰Dunlap Institute for Astronomy and Astrophysics, 50 St. George Street, Toronto, Ontario, M5S 3H4, Canada

³¹University of Massachusetts Amherst, 710 North Pleasant Street, Amherst, MA 01003-9305, USA

³²*Institute of Physics, Laboratory of Galaxy Evolution, Ecole Polytechnique Federale de Lausanne (EPFL), Observatoire de Sauverny, 1290 Versoix, Switzerland*

³³*Laboratory for Multiwavelength Astrophysics, School of Physics and Astronomy, Rochester Institute of Technology, 84 Lomb Memorial Drive, Rochester, NY 14623, USA*

³⁴*Department of Physics and Astronomy, Colby College, Waterville, ME 04901, USA*

³⁵*MIT Kavli Institute for Astrophysics and Space Research, 77 Massachusetts Ave., Cambridge, MA 02139, USA*

³⁶*Institute of Astrophysics, Foundation for Research and Technology–Hellas (FORTH), Heraklion, GR-70013, Greece*

³⁷*Department of Physics, University of Crete, 70013, Heraklion, Greece*

³⁸*Space Telescope Science Institute, 3700 San Martin Drive, Baltimore, MD 21218, USA*

³⁹*Department of Astronomy, Stockholm University, Oscar Klein Centre, AlbaNova University Centre, 106 91 Stockholm, Sweden*

⁴⁰*Department of Physics and Astronomy, Texas A&M University, College Station, TX, 77843-4242 USA*

⁴¹*George P. and Cynthia Woods Mitchell Institute for Fundamental Physics and Astronomy, Texas A&M University, College Station, TX, 77843-4242 USA*

⁴²*INAF, Osservatorio Astronomico di Roma, Via Frascati 33, 00078 Monteporzio Catone, Roma, Italy*

⁴³*Center for Computational Astrophysics, Flatiron Institute, 162 5th Avenue, New York, NY 10010, USA*

⁴⁴*Max-Planck-Institut für extraterrestrische Physik (MPE), Gießenbachstraße 1, 85748 Garching, Germany*

⁴⁵*School of Astronomy and Space Science, University of Chinese Academy of Sciences (UCAS), Beijing 100049, China*

⁴⁶*National Astronomical Observatories, Chinese Academy of Sciences, Beijing 100101, China*

⁴⁷*Institute for Frontiers in Astronomy and Astrophysics, Beijing Normal University, Beijing 102206, China*

⁴⁸*NSF National Optical-Infrared Astronomy Research Laboratory, 950 North Cherry Avenue, Tucson, AZ 85719, USA*

ABSTRACT

We compile JWST/NIRSpec prism and MIRI data for 249 Little Red Dots (LRDs) at $2.3 < z < 9.3$, forming a representative spectroscopic subset of NIRC*am*-selected LRDs. We derive a median stacked spectrum covering rest-frame 0.09–1.2 μm , with MIRI photometry extending the spectral energy distribution to 4 μm . Four additional stacks for subsamples defined by optical-to-UV luminosity ratios show that LRDs form a heterogeneous population spanning diverse continuum slopes and line properties. Assuming LRDs host super-massive black holes (BHs) surrounded by dense gas clouds, and stars accompany this core, we infer masses of $M_{\text{BH}} \sim 10^{6.0-6.5} M_{\odot}$ and $M_{\star} \sim 10^{8.3} M_{\odot}$, corresponding to BH-to-stellar mass ratios of 1–2%. The stacks show ubiquitous UV and optical FeII emission, indicating a direct view of the broad-line region and high (but sub-Eddington) accretion ($\lambda_{\text{Edd}} = 0.6 \pm 0.2$). We find a significant stellar contribution in the far-UV, reaching $\sim 80\%$ in the bluest systems. Possible Wolf–Rayet features (HeII λ 4687, nitrogen lines) are identified, tracing a young (3–7 Myr) compact starburst event. We also detect strong Balmer breaks and atypical Balmer, Paschen, [OIII], and optical and near-infrared HeI line ratios, and an absorption at $\sim 4550 \text{ \AA}$ (probably linked to FeII), all consistent with radiative-transfer effects in high-density gas with warm temperatures (4000–7000 K). We find a diversity of LRD flavors modulated by the luminosity ratio between between a short ($\lesssim 20$ Myr) and intense phase of BH activity, the most extreme stage lasting $\sim 3 - 7$ Myr, characterized by near-Eddington-limit radiation, and a nuclear and compact starburst dominated by massive stars (even super-massive, $M_{\text{SMS}} \sim 10^5 M_{\odot}$), all embedded in dense gas with modest dust content producing a variety of optical depths.

Keywords: Galaxy formation (595) — Galaxy evolution (594) — High-redshift galaxies (734) — Stellar populations (1622) — Broad band photometry (184) — Galaxy ages (576) — JWST (2291) — Active galactic nuclei(16)

1. INTRODUCTION

The James Webb Space Telescope (JWST, J. P. Gardner et al. 2006, 2023) has probed galaxy evolution in the first billion years ($z \gtrsim 5$) with unprecedented detail (see A. Adamo et al. 2025; D. P. Stark et al. 2026, and references therein). Based on the JWST observations gathered during the first two years of scientific opera-

tions, three closely related results of significant cosmological impact have emerged. First, many independent works identified a relatively large number, compared to expectations (see, e.g., S. L. Finkelstein et al. 2023; P. G. Pérez-González et al. 2023a; G. C. K. Leung et al. 2023; K. N. Hainline et al. 2024a; P. G. Pérez-González et al. 2025), of bright ultraviolet (UV) galaxies already

in place in the first 500 Myr of cosmic time ($z \gtrsim 10$; M. Castellano et al. 2023; C. T. Donnan et al. 2023; S. L. Finkelstein et al. 2022, 2023; Y. Harikane et al. 2023a; R. P. Naidu et al. 2022; P. G. Pérez-González et al. 2023a). Many of these candidates have been confirmed spectroscopically (A. J. Bunker et al. 2023; P. Arrabal Haro et al. 2023a; M. Castellano et al. 2024; S. Carniani et al. 2024; P. Arrabal Haro et al. 2023b; E. Curtis-Lake et al. 2023; Y. Harikane et al. 2024; B. Wang et al. 2023). These results prove that luminous galaxies were already in place 300 million years after the Big Bang pushing theories for galaxy formation back to earlier epochs than previously expected.

The resulting high UV luminosity density could arise from several physical phenomena. Some of these galaxies appear to be dominated by star formation (e.g., A. J. Bunker et al. 2023; J. M. Helton et al. 2025a). Another possibility is that many of the UV photons are linked to nuclear activity arising from the material surrounding supermassive black holes (SMBHs, or intermediate-mass black holes, IMBH, defined here as smaller than $10^6 M_\odot$), i.e., due to active galactic nuclei (AGN). This relates to the second highly relevant cosmological result presented in the JWST mission early years: a wealth of observational evidence of the presence of accreting SMBHs in many high-redshift galaxies. Indeed, spectroscopic data have revealed broad components in the emission lines detected in the spectra for many galaxies (D. D. Kocevski et al. 2023; Y. Harikane et al. 2023b; R. Maiolino et al. 2024; A. J. Taylor et al. 2025a). Complementary to this, optical line ratios also point to strong radiation fields in many high-redshift galaxies, consistent with photoionization from AGN (J. Scholtz et al. 2025; G. Mazzolari et al. 2025; M. Castellano et al. 2025).

The high abundance of AGN in the early Universe (e.g., R. Maiolino et al. 2024) may be related to another key result: the deviation of some of these early and very active galaxies from local relations between the masses of the SMBH and the host, with the former claimed to be overmassive (by, in some cases, more than a dex) compared to their stellar mass (R. Maiolino et al. 2024; F. Pacucci et al. 2023; F. Pacucci & A. Loeb 2024).

The high abundance of active (and possibly evolved) SMBHs in the early (< 1 Gyr old) Universe includes a previously unknown type of source known as Little Red Dots (LRDs). The name refers to their compact, point-like nature in the reddest NIRCcam filters and their relative faintness in the bluest NIRCcam bands. These two features have been used for efficient selection of these objects, showing them to be ubiquitous in all JWST imaging surveys (see, e.g., I. Labbé et al. 2023; P. G.

Pérez-González et al. 2023b; G. Barro et al. 2024; H. B. Akins et al. 2025a; D. D. Kocevski et al. 2025), with a space density making them a significant fraction of all quasars and AGNs (e.g., C. C. Williams et al. 2024; Y. Ma et al. 2025a; R. Maiolino et al. 2025a). Some LRDs were found to show broad emission lines with NIRSpec/PRISM spectra (J. E. Greene et al. 2024) and NIRCcam/WFSS (J. Matthee et al. 2024), leading to the conclusion that they contained, and were perhaps powered predominantly by, AGNs. Further follow-up spectroscopic observations of LRDs confirmed the presence of broad emission line components in a majority of LRDs (D. D. Kocevski et al. 2023; F. D'Eugenio et al. 2025; M. Killi et al. 2024; A. Torralba et al. 2025; R. E. Hviding et al. 2025; A. J. Taylor et al. 2025b).

The defining red nature of LRDs suggests the presence of dust. However, the presence of dust in all LRDs is not unequivocally confirmed (P. G. Pérez-González et al. 2024a; C. C. Williams et al. 2024), although some individual examples have been detected in the far-infrared (G. Barro et al. 2026) and small amounts of dust have been claimed based on stacks (C. M. Casey et al. 2024). And this is, in fact, the third highly relevant cosmological result provided by JWST: the significant amounts of dust formed in the very early Universe, not only revealed in LRDs but also in the attenuation seen in the highest-redshift galaxies (see, e.g., J. Witstok et al. 2023; J. M. Helton et al. 2025b; C. T. Donnan et al. 2025), as well as the floor in metallicity around 5–10% solar observed in most galaxies at high redshift (e.g., K. Nakajima et al. 2023; M. Curti et al. 2023; R. Tripodi et al. 2025a; J. M. Helton et al. 2025a; F. Cullen et al. 2025, but some lower metallicity galaxies have also been discovered, T. Y.-Y. Hsiao et al. 2025; E. Vanzella et al. 2025; T. Morishita et al. 2025a).

These three early results of JWST in the cosmological research area are not completely understood. We can identify four main aspects of the interpretations that need refining or even validation, and that particularly affect the interpretation of the nature of LRDs and might be biasing our view of the early Universe.

First, the physical conditions of the gas in high redshift galaxies have been demonstrated not to be exactly the same as in local star-forming galaxies (SFGs) at redshifts as low as $z \sim 2$. Consequently, the extreme line ratios observed for some high- z AGN candidates can still be linked to intense and concentrated bursty star formation (A. J. Cameron et al. 2023; K. Boyett et al. 2024; A. E. Shapley et al. 2025). Indeed, for most JWST-detected AGN the classic rest-optical emission line ratio diagnostic diagrams do not extrapolate easily to high redshifts, so star-forming galaxies and AGN are mixed

in the same region of the diagnostic diagrams due to the low gas metallicities and high ionization parameters (J. R. Trump et al. 2023; B. E. Backhaus et al. 2024; R. L. Sanders et al. 2023; N. J. Cleri et al. 2025; L. Clarke et al. 2026).

Directly related to the previous point, the AGN-nature of the broad components of LRDs have been challenged by alternative interpretations such as the presence of dense low-metallicity outflows linked to star formation (M. Kokubo & Y. Harikane 2025), extreme line broadening due to gas kinematics in very compact starbursts (J. F. W. Baggen et al. 2024), or significant effects linked to collisional excitation in dense gas clouds in the cores of high redshift galaxies (K. Inayoshi & R. Maiolino 2025). The proposal for dense gas clouds surrounding a compact ionizing source (e.g., E. R. Coughlin & M. C. Begelman 2024) to explain LRDs has now gained momentum in the so-called quasi-star, blackhole envelope (BHE) or blackhole star (BH*) models (e.g., D. Kido et al. 2025; R. P. Naidu et al. 2025; K. Inayoshi & L. C. Ho 2025; M. C. Begelman & J. Dexter 2026; A. de Graaff et al. 2025a; W. Q. Sun et al. 2026).

A second source of uncertainty in interpreting JWST results, particularly for LRDs and other AGN candidates, concerns the derivation of stellar and SMBH masses. Early analyses inferred very large stellar masses for some systems (I. Labbé et al. 2023), largely because the red rest-frame optical emission was modeled as purely stellar. Reproducing the observed colors under this assumption required substantial dust attenuation and high stellar masses, in some cases approaching or exceeding expectations from baryon abundances in early halos within the Λ CDM paradigm (M. Haslbauer et al. 2022; M. Boylan-Kolchin 2023; A. Dekel et al. 2023). Such estimates depend critically on modeling choices, including the adopted initial mass function (IMF); for example, a top-heavy IMF could further bias stellar masses high (S. Chon et al. 2022; C. L. Steinhardt et al. 2023; M. R. Bate 2025), as the warmer cosmic background radiation heats the interstellar gas and inhibits the formation of low-mass stars and brown dwarfs.

Conversely, stellar masses may be underestimated if the rest-frame optical and near-infrared emission is attributed predominantly to dust-attenuated accretion disks, bright tori (I. Labbe et al. 2025), or a BH*-like component with little or no stellar contribution, potentially leading to the interpretation of LRDs as hosting over-massive SMBHs. Ultimately, the relative contributions of stars and AGN to the global spectral energy distribution (SED) of LRDs remain uncertain, and assumptions about star-formation histories and dust attenuation can significantly affect the derived stellar and

black hole masses (e.g., G. Barro et al. 2024; P. G. Pérez-González et al. 2024a).

Similarly, SMBH mass estimates for LRDs introduce additional uncertainty. These are typically based on single-epoch calibrations derived from low-redshift AGN (J. E. Greene & L. C. Ho 2005; A. E. Reines & M. Volonteri 2015), whose applicability at high redshift is uncertain. Moreover, current spectroscopic samples are likely biased toward the most luminous and extreme systems (J. Li et al. 2025; M. Brooks et al. 2025), potentially skewing inferred black hole mass distributions.

A third open question for LRDs is how much dust they have, and whether their red nature can be linked to it, or only to the effects of dense gas clouds (i.e., obscuration only due to gas). As mentioned before, there is not a consensus about the amount of dust in LRDs. In fact, the latest modeling efforts in terms of BH* assign most of the red optical slopes and prominent Balmer breaks to opacity by gas, not dust (e.g., A. de Graaff et al. 2025a).

The fourth, and final, point to take with a grain of salt is the extrapolation of properties derived for some LRDs whose spectroscopy has been analyzed in a number of papers (D. D. Kocevski et al. 2023; M. Killi et al. 2024; B. Wang et al. 2024; J. E. Greene et al. 2024; A. de Graaff et al. 2025b) to a more general and numerous number of sources identified as LRDs with NIRCcam photometry (V. Kokorev et al. 2024; D. D. Kocevski et al. 2025; G. Barro et al. 2024). In this regard, the limited overlap between LRD samples, whose selection (and consequently, definition) is not standardized, is concerning (K. N. Hainline et al. 2025; R. E. Hviding et al. 2025; G. Barro et al. 2025). LRDs appear to be a heterogeneous group of sources in terms of their SED and spectral properties, and it is possible that their nature may not all be attributable to a single mechanism/scenario.

In this paper, we address these four debated topics by analyzing a complete sample of photometrically selected LRDs and gathering all the available spectroscopy provided by JWST, as well as MIRI imaging covering the rest-frame near- and mid-infrared (IR). The goal is to understand the nature of LRDs by, (1) investigating whether any heterogeneity in their (photometric, spectral) properties is linked to the different selection techniques, and (2) carefully understanding whether the LRDs with currently available spectroscopy are representative of the more general photometric sample. Our analysis technique aims to escape from the degeneracies introduced by the studies based on photometry alone (e.g., P. G. Pérez-González et al. 2024a) or bright emission line profiles and ratios alone (D. D. Kocevski et al. 2023, 2025; A. J. Taylor et al. 2025b; P. Rinaldi et al.

2025), by predominantly using the continuum emission, jointly with the faint emission lines, in a wide spectral range covering the UV, optical, and near-IR.

This paper is organized as follows. Section 2 presents the photometric and spectroscopic samples used in this paper, describing the NIRCam, NIRSpec and MIRI datasets gathered to analyze a statistically representative sample of LRDs. Section 3 introduces a stack of spectra for nearly 250 LRDs and discusses some interesting features in the UV, optical, and near-IR. Section 4 divides the full sample of LRDs in several subtypes and analyzes the heterogeneity of properties within the LRD population. Section 5 further analyzes the different subtypes of LRDs based on SED fitting performed on the NIRSpec and MIRI stacks. Section 6 discusses all our findings in comparison with the literature. Finally, Section 7 presents a summary of our work and conclusions.

In this paper, we assume a flat Λ CDM cosmology with $\Omega_M = 0.3$, $\Omega_\Lambda = 0.7$, and a Hubble constant $H_0 = 70 \text{ km s}^{-1} \text{ Mpc}^{-1}$. We use AB magnitudes (J. B. Oke & J. E. Gunn 1983). We presume a universal G. Chabrier (2003) initial mass function (IMF). We refer to all emission lines via their vacuum wavelengths.

2. DATA AND LITTLE RED DOT SELECTIONS

2.1. Photometric selection

Using the ASTRODEEP–JWST catalogs presented in E. Merlin et al. (2024), we construct a sample of 849 photometrically selected LRDs across six JWST deep fields (also used in G. Barro et al. 2025): GOODS-S and GOODS-N from JADES (M. Rieke 2020; A. J. Bunker et al. 2020; D. J. Eisenstein et al. 2023, 2025), EGS from CEERS (S. L. Finkelstein et al. 2025), COSMOS and UDS from PRIMER (Dunlop et al., in prep.), and A2744 from GLASS-JWST (T. Treu et al. 2022) and UNCOVER (R. Bezanson et al. 2024). The ASTRODEEP–JWST catalog provides NIRCam photometry measured in small apertures in PSF-matched images and then corrected to total R. G. Kron (1980) apertures.

Our LRD selection is designed to be as complete as possible by combining multiple, complementary photometric criteria. The full selection technique is illustrated in Figure 1. The core of the selection follows the color–color approach introduced by G. Barro et al. (2026), using the F115W–F200W versus F200W–F444W diagram to identify sources with blue rest-frame ultraviolet continua and red rest-frame optical slopes, i.e., utilizing the main distinctive feature of LRDs, the V-shaped SED. This method efficiently recovers the bulk of the LRD population over $z \sim 3$ –7 and captures a wide range of intrinsic UV–to–optical colors. To minimize contamination from brown dwarfs, we

apply an additional photometric cut of F115W–F200W > -0.5 (J. E. Greene et al. 2024; K. N. Hainline et al. 2024b). A small number of spectroscopically confirmed LRDs can scatter blueward of this threshold (see four galaxies with spectroscopy –i.e., in yellow– in the top left panel of Figure 1), but this cut effectively removes the bulk of stellar contaminants without significantly impacting completeness.

To improve completeness, particularly at higher redshifts, we additionally apply the F277W–F444W versus F444W color–magnitude selection used in G. Barro et al. (2024) and P. G. Pérez-González et al. (2024a), selecting LRDs with a color F277W–F444W > 1 . This criterion is effective at recovering LRDs that may fall outside the color–color selection, especially at $z \gtrsim 8$, where (i) the F150W–F200W color begins to trace the Lyman break; (ii) the bands redder than $4 \mu\text{m}$ can be heavily contaminated by [OIII]+H β emission, and (iii) the magnitudes become fainter, all resulting on the selection becoming increasingly uncertain, unreliable, and/or incomplete.

Finally, we supplement the photometrically selected sample with a small number ($\lesssim 5\%$) of additional LRDs drawn from the catalogs of V. Kokorev et al. (2024) and D. D. Kocevski et al. (2025). These sources are not recovered by the primary color selections but are included to ensure maximal completeness of the LRD population. The combined selection (adding sources selected with any of the methods above) therefore recovers nearly all previously reported LRDs while extending the earlier, more restrictive definitions to bluer UV–to–optical colors.

Morphological compactness in the rest-frame optical is enforced by requiring a small-aperture flux ratio of $F[\text{F444W}(d = 0''.5)]/F[\text{F444W}(d = 0''.2)] < 1.5$, ensuring that selected sources are unresolved or marginally resolved in the rest-frame optical (see, e.g., J. E. Greene et al. 2024; J. F. W. Baggen et al. 2024).

In summary, our work compiles the LRDs in GOODS-S and GOODS-N (from JADES), UDS and COSMOS (from PRIMER), EGS (from CEERS), and the A2744 cluster field (from UNCOVER), probing an approximate total area of 690 arcmin^2 . A total of 849 LRDs are included in our photometric sample. Field to field variations of the number density are found at a 25% level. The average and standard deviation of the densities for all fields is $1.2 \pm 0.3 \text{ sources arcmin}^{-2}$.

2.2. Spectroscopic observations of LRDs

Our parent sample of LRDs was matched with the list of spectroscopically observed sources in all fields. In this paper, we concentrate our analysis on the NIRSpec prism data only, due to our focus on the continuum and

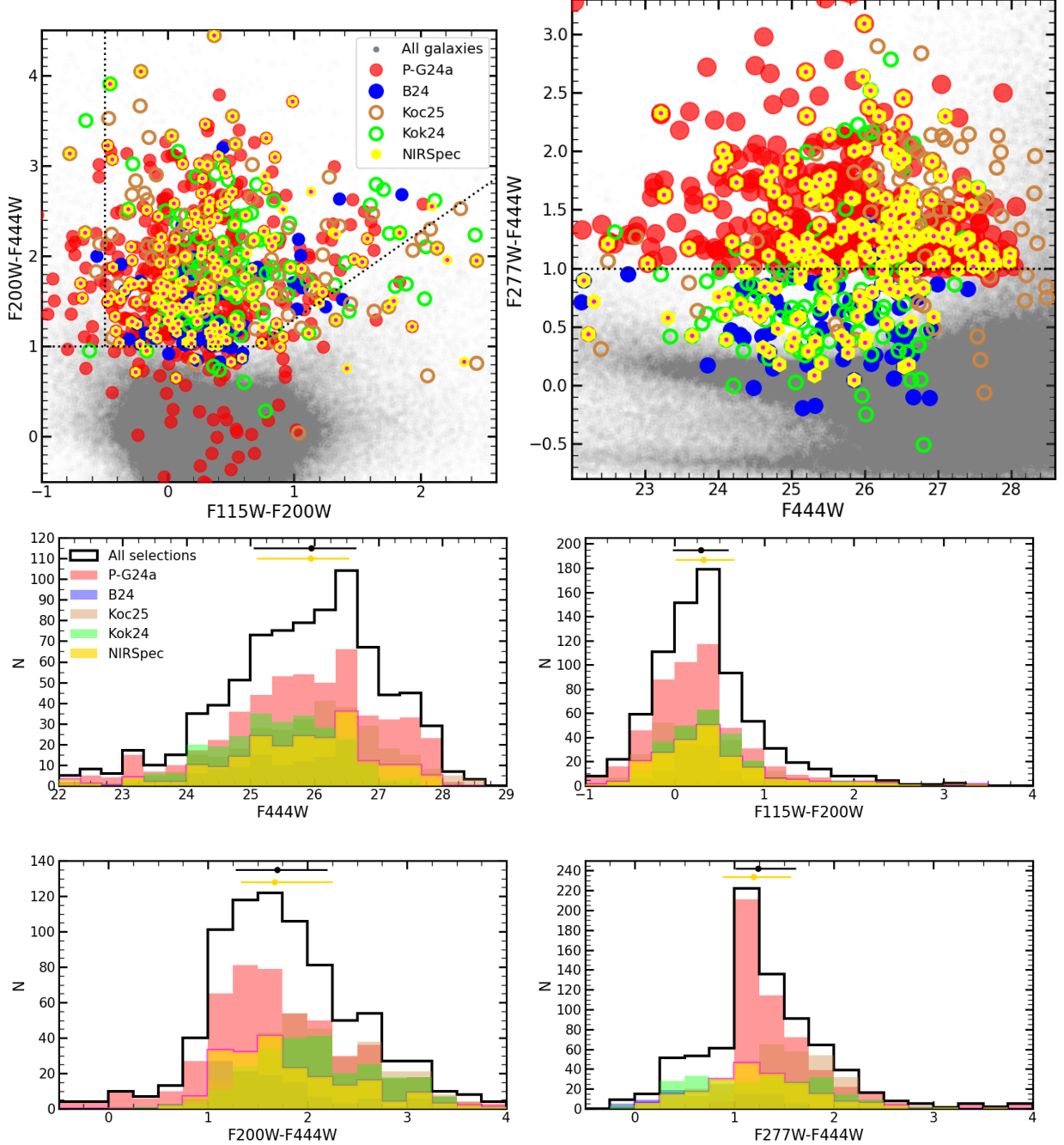


Figure 1. Photometric selection of LRDs, and the spectroscopic sample used in this work. *Top left:* Color-color diagram introduced by G. Barro et al. (2026), with the selection boundary represented by the dotted lines. The LRD selection criterion used in P. G. Pérez-González et al. (2024a) based on F277W-F444W colors is shown with red symbols, LRDs identified in D. D. Kocevski et al. (2025) and V. Kokorev et al. (2024) are shown as orange and lime symbols, respectively, while blue symbols depict the LRDs identified solely by G. Barro et al. (2026). Our spectroscopic sample (with NIRSpec prism observations) is depicted with yellow symbols. Gray symbols show the general NIRCcam sample (drawn from the ASTRODEEP–JWST catalogs presented in E. Merlin et al. 2024). *Top right:* Color-magnitude plot with LRD selection criterion used in P. G. Pérez-González et al. (2024a) based on F277W-F444W colors (marked with a dotted line). We use the same symbols described for the previous panel. *Middle left:* F444W magnitude distribution of the different samples of LRDs. *Middle right:* F115W-F200W color distribution of LRDs. *Bottom left:* F200W-F444W color distribution of LRDs. *Bottom right:* F277W-F444W color distribution of LRDs. In all the panels with histograms, the median and quartiles for the photometric (black) and spectroscopic (gold) samples are shown.

faint lines. We found a total of 249 observations with the NIRSpec prism carried out by a variety of programs. The program identifications and number of sources per field are given in Table 1.

We downloaded fully calibrated 2D spectra from MAST. The calibration was carried out with the JWST python package, pipeline version 1.20.2, reference files 1464.pmap. We extracted 1D spectra for all objects with a custom aperture that ranged from 3 to 5 pixels (for a few very bright objects we used 7 pixels) in the spatial direction (0.1 arcsec/pixel), determined to maximize the median signal-to-noise ratio of the final spectrum. The spectrum for each object was normalized to match its NIRCам broad-band fluxes, as extracted from the ASTRODEEP catalog, by applying a single multiplicative factor calculated as a weighted average of the ratios between the fluxes measured in photometry and in the spectra for the NIRCам passbands.

Virtually all of the spectra showed the emission lines [O III] $\lambda\lambda$ 4960, 5008 and, for sources at $z \lesssim 7$, H α . Several additional lines (Ly α , C III], [S II], [O II], H β , Paschen lines) were detected in many spectra. All were used to measure accurate (typical error < 0.005) spectroscopic redshifts.

2.3. MIRI data

All MIRI data publicly available in November 2025 for the six fields covered in this paper were reduced with the JWST Rainbow pipeline following the methodology described in P. G. Pérez-González et al. (2024a, see also P. G. Pérez-González et al. 2024b; G. Östlin et al. 2025). The observations come from different programs, PIDs provided in Table 1. Mosaics were constructed for filters F560W, F770W, F1000W, F1280W, F1500W, F1800W, F2100W, and F2550W. Details about this reduction will be presented in Pérez-González et al. (in prep.), while here we briefly describe the methodology. The JWST Rainbow reduction scheme uses the official JWST pipeline adding some extra bespoke reduction steps to deal with the background homogenization of the MIRI images. For this paper, the reduction was carried out with the JWST code, version v1.19.41, reference files in jwst_1413.pmap. A key component of this workflow is the ‘superbackground’ strategy, in which the background for each observation is flattened by constructing a template that combines all other images taken with the same filter within a 3-month period. Known sources are masked (after applying a dilation) to avoid background overestimates. This approach yields a highly homogeneous background in terms of both level and noise. This methodology has been demonstrated to improve depth by up to 0.8 mag in the final mosaics compared

to archive data. We refer the reader to Appendix A in P. G. Pérez-González et al. (2024a) for further details.

Photometry was performed by assuming LRDs are point-like sources and measuring in small apertures with diameters equal to the FWHM of the PSF for each filter. Correlated noise was taken into account in the estimation of uncertainties. See P. G. Pérez-González et al. (2024a,b) for more details. The MIRI fluxes for sources with SNR > 1 were added to the analysis in the rest of the paper by measuring a F444W-MIRI color in the aperture mentioned before, and applying it to the ASTRODEEP-JWST SED (which was used as a reference for the spectra).

The depth of the observations varies significantly in all filters from field to field and within each one of them. Typical (median for all fields of the medians for each filter) depths (5σ) in AB mag are 26.2 for F560W, 25.7 for F770W, 24.3 for F1000W, 24.1 for F1280W, 23.5 for F1500W, 22.8 for F1800W, 22.0 for F2100W, and 20.2 for F2550W.

The coverage of the MIRI observations for our spectroscopic sample is limited. The fraction of sources with MIRI data varies from 0% in F2550W to 60% in F770W, but the typical percentage is 30-40%, except for F560W, where only 12% of spectroscopic LRDs have data. The MIRI detection fraction among those LRDs in our spectroscopic sample with available data is high for wavelengths shorter than 10 μ m (50% detected in F1000W, 80% in F560W and F770W). The detection fraction is much smaller for the reddest wavelengths, ranging from 30% in F1280W to 10% in F2100W, 40% and 20% for F1500W and F1800W, respectively.

Very similar numbers are obtained for the photometric sample, with only a small bias in the reddest bands, in the sense that there is a lack of spectroscopy for photometrically selected LRDs detected in F1800W and F2100W.

2.4. Classification of LRDs

The full photometric and spectroscopic samples of LRDs were divided in different types. Given that the main distinctive spectral feature of LRDs is their V-shape SED (i.e., blue or flat UV and red optical slopes), we decided to sort them by spectral slope. More specifically, we use the optical-to-UV luminosity ratio as a proxy for the optical slope (as in, e.g., D. D. Kocevski et al. 2025 and K. N. Hainline et al. 2025), L_{5100}/L_{2500} (defined as luminosity densities in $\text{erg s}^{-1} \text{Hz}^{-1}$). We note that the use of L_{5100}/L_{2500} as an empirical classifier can be linked to both AGN and stellar population diagnostics, reflecting differences in, for example, dust

geometry, stellar age, and/or viewing angle. We refer the reader to Section 4 for more details.

Based on the optical-to-UV luminosity ratio, and using the photometric sample as a reference to avoid possible biases of the spectroscopic sample, we divided the list of LRDs with spectroscopy into four subsamples:

- *extreme* LRDs, ^xLRDs, defined as extremely red sources that are 1σ above the median ($L_{5100}/L_{2500} > 6.3$). Our sample has 29 ^xLRDs (12% of the whole sample).
- LRDs slightly above the median luminosity ratio, ⁺LRDs, which are above the median and 1σ ($3.1 < L_{5100}/L_{2500} < 6.3$). Our sample has 76 ⁺LRDs (31% of the whole sample).
- LRDs slightly below the median luminosity ratio, ⁻LRDs, which are between the median and -1σ ($1.8 < L_{5100}/L_{2500} < 3.1$). Our sample has 77 ⁻LRDs (31% of the whole sample).
- *blue* LRDs, ^bLRDs, defined as those with $L_{5100}/L_{2500} < 1.8$. Our sample has 67 ^bLRDs (27% of the whole sample).

2.5. Similarity of the spectroscopic and photometric samples

The observational properties of the spectroscopic sample compiled in this paper compared to photometrically selected LRDs are presented in Figure 1. The color-magnitude (I. Labbé et al. 2023; P. G. Pérez-González et al. 2023b; G. Barro et al. 2024; P. G. Pérez-González et al. 2024a) and color-color (G. Barro et al. 2026) diagrams used in the photometric selection of LRDs (see also D. D. Kocevski et al. 2025) show that our sample of LRDs with prism spectroscopy is representative of the whole photometric LRD selection down to F444W magnitude around 27 (with a few sources up to one magnitude fainter). In particular, by using the comprehensive selection technique presented in G. Barro et al. (2026), our spectroscopy compilation covers the selections of V. Kokorev et al. (2024) and D. D. Kocevski et al. (2025), which are biased towards blue and red LRDs, respectively.

The main photometric properties of the parent sample of photometrically selected LRDs and the sample with spectroscopy compiled for this paper are given in Table 2. Summarizing the properties of these samples, we consider spectroscopic LRDs with F444W magnitude around 26, median and quartiles $F444W =$

$25.9_{25.0}^{26.5}$ mag⁴⁹, consistent within 0.1 mag with the values for the photometric sample. Concerning colors, the photometric and spectroscopic samples of LRDs present F277W-F444W colors around 1.2 mag, and F115W-F200W colors around 0.3 mag (consistent with the V-shape SED selection); almost identical values are obtained for the photometric and spectroscopic samples. We conclude that, globally, the spectroscopic sample is representative of the photometric sample. Table 2 also provides statistical information for subsamples drawn from the LRD spectroscopic sample defined in Section 2.4, to be discussed in Section 3, and for which the similarity to the photometric sources is weaker.

In Figure 2, we present the redshift distribution of the different samples. The median redshift of our spectroscopic sample is slightly lower than that of the parent photometric sample. Median and quartiles are $z = 5.7_{4.5}^{7.0}$ for the NIRSpect sample, and $z = 6.4_{5.1}^{7.6}$ for the NIRCам one, both pointing to the fall of the LRD population at $z \sim 3$. We do not interpret this bias as a photometric redshift problem, but it is rather linked mainly to the low completeness of the spectroscopic sample at faint magnitudes (F444W magnitude fainter than 27). Indeed, if we cut the photometric sample to $F444W < 27$ mag, the redshift statistics, $z = 6.2_{4.8}^{7.5}$, become more similar to the spectroscopic sample. We conclude that the spectroscopic sample of LRDs is biased towards the lower redshift end of the photometrically selected population.

Figure 2 also shows redshift histograms for four different types of LRDs based on optical-to-UV luminosity ratios, from the reddest (top) to the bluest (bottom), presented in the previous subsection (see also Section 4). These histograms show that, generally, the spectroscopic samples are biased towards lower redshifts compared to photometric samples, the median redshifts being around $z = 6$ for the former and $z = 7$ for the latter in all subtypes except the bluest. For the bluest LRDs, the photometric sample distribution extends to lower values compared to the sources with spectroscopic observations. Remarkably, the bias in the spectroscopic samples is largest for the very reddest LRDs, median redshifts being $z \sim 6.9$ and $z \sim 5.2$ for the photometric and spectroscopic samples, respectively. Overall, the redshift distributions of the photometric subsamples are asymmetric, with the distance from the median to the 25% quartile being larger than to the 75% quartile. This

⁴⁹ In the rest of the paper, we distinguish in the nomenclature between median and scatter (represented by quartiles), given with sub- and super-script fonts and not showing any sign, and uncertainties, given as an upper and lower error with a sign.

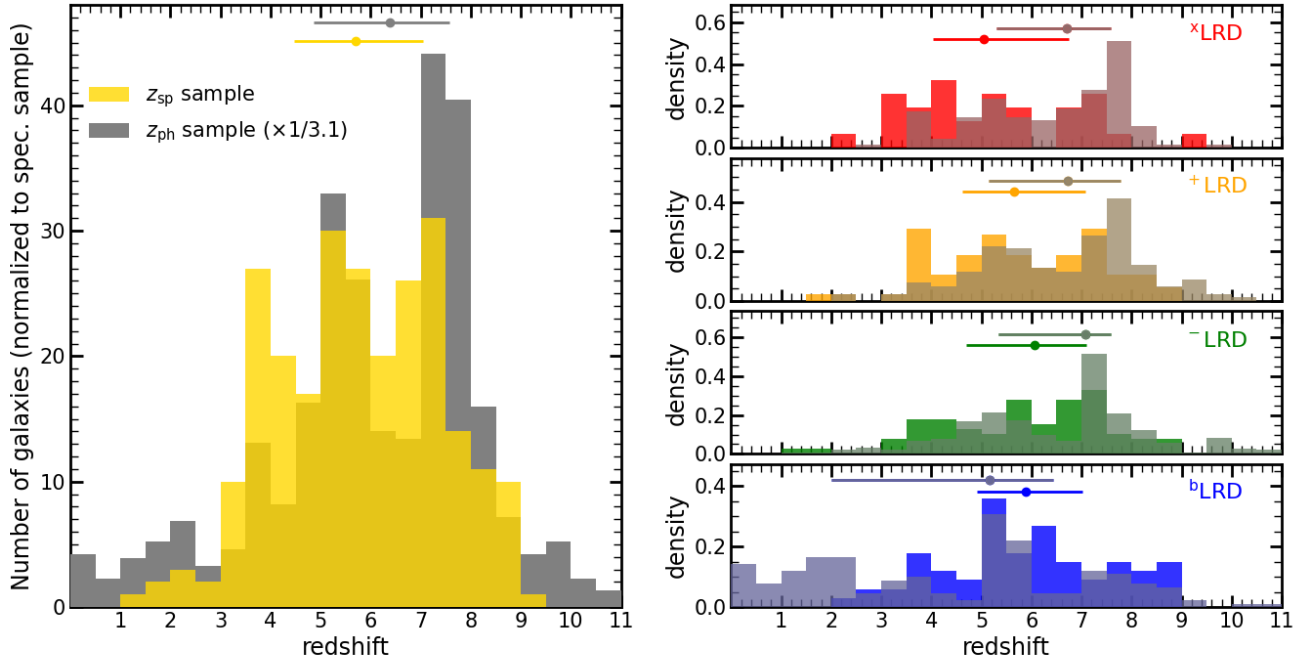


Figure 2. *Left:* Redshift distribution for the spectroscopic sample of LRDs characterized in this paper (gold histogram) and the general sample of photometrically selected LRDs presented in Figure 1 (gray histogram, scaled down by a factor of ~ 4 to make the comparison easier). *Right:* Same but for the different LRD subtypes defined in Section 2.4, based on optical-to-UV luminosity ratios, running from the reddest LRDs (top) to the bluest (bottom). The photometric sample plotted again in gray, and this time using normalized histograms. In all panels, the median and quartiles of the distributions are shown with dots and segments, the gray histograms refer to the photometric sample and the colored ones to the spectroscopic subsamples.

might indicate a selection effect against sources beyond $z \sim 8$, i.e., LRDs at higher redshifts than currently known (A. J. Taylor et al. 2025b), which will only be revealed with deep MIRI data (see, e.g., P. G. Pérez-González et al. 2024b; E. Iani et al. 2025; T. S. Tanaka et al. 2025).

Compared to the sample of LRDs with spectroscopy discussed in A. de Graaff et al. (2025b), our sample extends to higher redshifts and fainter magnitudes. The median and quartiles for their paper are $z = 5.0_{6,0}^{4,2}$ and $F444W = 25.4_{24,7}^{26,2}$ mag (after applying a 0.6 mag correction to their quoted values in Table 1), while we cover a median redshift of $z \sim 6$ and a median magnitude fainter by 0.5 mag. A similar result is obtained when comparing with the spectroscopic samples in G. Barro et al. (2025) and W. Q. Sun et al. (2026).

3. MEDIAN PROPERTIES OF LITTLE RED DOTS BASED ON A STACKED SPECTRUM

To characterize the typical properties of LRDs, we stacked all the spectra gathered in this work. We used two methods to stack, obtaining almost identical results on the analysis presented in the following sections.

For the first method, we built a rest-frame wavelength grid from 0.07 to 1.2 μm with a pixel spectral scale given

by the resolution of the NIRSpec prism (P. Jakobsen et al. 2022) for a $z = 6$ source (the median redshift of our sample). To calculate the sampling bins, we took into account two facts. First, we are stacking (almost) point-like sources, which lie at different redshifts and thus probe the rest-frame at a variety of nodes. Second, the spectral resolution of NIRSpec prism observations has been proven to be better than pre-launch expectations by up to 50% (A. J. Shajib et al. 2025). This improvement can be explained because the spectral resolution was measured for a uniformly illuminated shutter, compared to which point-like sources (such as LRDs) will have higher resolution values. With this in mind, and after some testing, we used a wavelength array with 0.5 times smaller bins compared to the fiducial grid (fiducial meaning the default pixel sampling of the 1D NIRSpec spectra output by the pipeline).

For the second method, we used a constant pixel spectral size, set to 5 \AA , found to be the optimal taking into account the considerations about spectral resolution presented before.

All the analysis presented in the remainder of this paper was performed in the stacks built with the two methods, obtaining almost identical results. We choose the

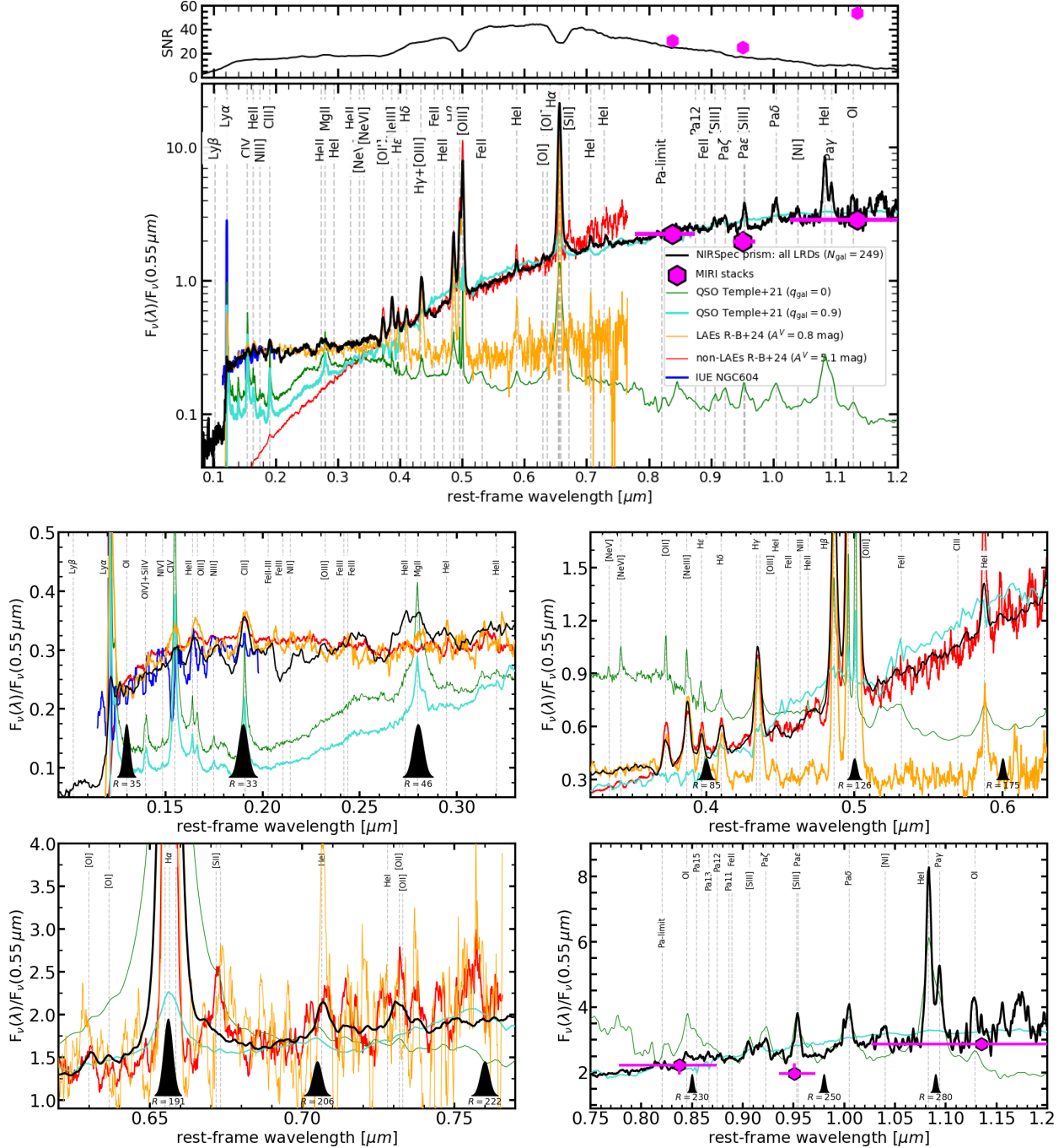


Figure 3. The *top panel* shows the stacked spectrum of the 249 LRDs with NIRSpec prism spectroscopy selected in this paper (black line). The MIRI stacks in the same rest-frame wavelength range are shown (including a horizontal error bar enclosing the wavelength range for 68% of the MIRI points entering the stack), to demonstrate that they agree with the spectroscopic stack (see next figure for redder MIRI stacks). The spectrum is compared with QSO models from *M. J. Temple et al. (2021)* for a pure AGN ($q_{\text{gal}} = 0$, green line) and 90% contribution from a host ($q_{\text{gal}} = 90\%$, cyan line). In orange and red, we show the stacked spectra for LAEs and non-LAEs presented in *G. Roberts-Borsani et al. (2024)*, after applying $A^V = 0.8$ and 5.1 mag attenuation, respectively, following a *D. Calzetti et al. (2000)* law. The QSO templates are normalized to the emission around the $\text{MgII}\lambda 2798$ line, the LAE template is normalized to the emission around $0.28 \mu\text{m}$, and the non-LAE template and median LRD SED are normalized at $0.55 \mu\text{m}$. The panels below the main one show zoomed-in versions (in linear scale for the flux axis) in the UV (*middle left panel*), optical around $[\text{OIII}]+\text{H}\beta$ and $\text{H}\alpha$ regions (*middle right and bottom left, respectively*), and the near-IR (*bottom right*). In these panels, the comparison spectra are normalized to the median in the spectral window covered by the plot. The Gaussians at the bottom of the panels show the spectral resolution at different wavelengths.

second method (constant pixel size) for the plots in the rest of the paper.

Since we are combining data for sources at different redshifts, we degraded all the individual spectra to a

common resolution, which varies significantly with wavelength for the prism. For this common resolution, we tested using the minimum and the median values of the distribution of resolutions of the individual sources entering the stack at a given wavelength. The test showed minor differences in the final spectra, with completely negligible effects on the results.

In summary, the spectra of individual sources were rebinned to a rest-frame wavelength array typically with constant spectral pixel size (5 Å), normalized to the flux at rest-frame 0.55 μm (averaged between 0.51 and 0.59 μm , a spectral region free of bright emission lines), and then stacked, calculating the 16%, 50% (i.e., we produced median stacks), and 84% quantiles. Following the method presented in G. Roberts-Borsani et al. (2024), the difference between the 16% and 84% quantiles, divided by the square root of the number of objects entering the stack at each wavelength, was used as the estimated error of the median. We note that this calculation is linked to two effects: the intrinsic diversity of the SEDs of LRDs, and the noise in the individual spectra. The stacks were scaled in flux to match the median optical luminosity density (at 5100 Å) of the different samples used in the analysis for $z = 7$ (approximate median redshift of the photometric sample).

The resulting stacked spectrum combines data for more than 200 LRDs spanning from Ly α to H α (both included), and more than 60 LRDs up to Pa γ . Beyond that wavelength, only 10 LRD spectra reached Pa β , so we cut the spectroscopic stack at 1.2 μm . However, we complement the stack with MIRI photometric data to probe the behavior of the median LRD up to 4 μm rest-frame wavelength. For the MIRI extension, we proceeded in the same way as for the spectra: we normalized the fluxes, and we calculated medians and uncertainties in bins constructed to at least have 20 observations.

The stacked spectrum of LRDs is presented in Figure 3. It is very similar to the median SED of LRDs constructed in P. G. Pérez-González et al. (2024a) with NIRCcam and MIRI data (see also the imaging stack in H. B. Akins et al. 2025a). The median LRD presents an optical-to-UV luminosity ratio, L_{5100}/L_{2500} , (defined as the ratio between L_ν values at 0.51 and 0.25 μm) of 2.7, which for the typical redshift of LRDs, $z \sim 6$, would translate to F200W – F356W ~ 1 mag and an optical slope $\beta_\nu^{\text{opt}} \sim 2.5$ (as defined in G. Barro et al. 2025). In the UV, the spectrum is quite flat, with a slope $\beta_\nu^{\text{UV}} \sim 0.2$. The median spectrum of LRDs presents a flattening and slight curvature in the near-infrared, at wavelengths beyond ~ 0.8 μm , as found in previous analyses of MIRI data (P. G. Pérez-González et al. 2024a; C. C. Williams et al. 2024). The SED rises slowly

at least up to 4 μm (see the discussion in the next subsection, pointing to Figure 6).

3.1. Comparison of the median LRD spectrum with other types of sources

The median LRD spectrum presented in Figure 3 is now compared to some relevant templates of different types of sources. We first compare with QSO templates from M. J. Temple et al. (2021). The colors of the pure QSO template are dominated by the accretion disk and broad line region (BLR) in the UV, and do not present the typical V-shaped SED of LRDs. If we normalize the LRD stack and the QSO template to the UV emission (at ~ 0.28 μm), we see that the QSO spectrum is much redder than LRDs in the UV and bluer in the optical and near-IR. A QSO template with 90% contribution from the host galaxy, which is still dominated by the AGN in the UV (the SED is very similar in both M. J. Temple et al. 2021 templates bluewards of 0.3 μm), would fit the continuum of LRDs quite nicely at all wavelengths redwards of 0.28 μm , but would not reproduce the UV either. Some relevant lines are present both in QSOs and in LRDs, for example, NIV] λ 1486, and very remarkably, redwards of 0.2 μm , Fe III emission complexes at wavelengths around 2030, 2105, or 2418 Å, or Fe II around 3150 and 3280 Å (A. Laor et al. 1997; M. Vestergaard & B. J. Wilkes 2001).

We also compare the LRD median spectrum with the stacks of star-forming galaxies presented in G. Roberts-Borsani et al. (2024) for both Ly α emitters (LAE) and non-LAEs. The general shape of the LAE template does not fit the LRD. The intrinsic UV slope of LAE is $\beta_\lambda^{\text{UV}} \sim -2.5$, which is bluer than the typical $\beta_\lambda^{\text{UV}} \sim -2$ for LRDs and star-forming galaxies at $z < 10$ (M. W. Topping et al. 2022; F. Cullen et al. 2024; A. M. Morales et al. 2025). Thus, in Figure 3, we apply some dust attenuation to the G. Roberts-Borsani et al. (2024) stacks based on the D. Calzetti et al. (2000) law ($A^V = 0.8$ mag). Apart from the general shape, the spectral features in the UV for LRDs are very similar to those from the LAE stack, as seen in the zoomed version of the spectrum comparison in the middle-left panel of Figure 3. Both the LRD and LAE spectra present some Ly α emission, fainter in the case of LRDs. Other relevant emission lines seen in both spectra are C III] λ 1908, He II] λ 1640 and Mg II] λ 2798. Although not covered by the LAE stack, we remark on the non-zero emission bluewards of Ly α .

The LRD composite is also remarkably similar to the IUE far-UV spectrum of NGC604, a famous H II region in the Triangulum galaxy (R. M. González Delgado & E. Pérez 2000; F. C. Bruhweiler et al. 2003), shown here

to represent a pure star-forming source (in fact, an OB association) with no contamination from an AGN. The comparison of the LRD and H II region spectra presents several distinct differences, e.g., a stronger Ly α emission and also stronger emission bluewards of it in NGC604 (which can be related to differences in the IGM absorption at low and high redshift), and a P-Cygni C IV absorption in NGC604 (typically linked to stellar winds and ISM absorption). Nevertheless, this absorption feature would be undetectable in our low spectral resolution spectrum and, interestingly, the peak emission around the C IV line (redshifted from the rest-frame value) coincides very well with the local H II region and the median LRD spectrum.

All these comparisons would point to a significant contribution of star formation to the continuum emission of the typical LRDs in the UV (0.1-0.4 μm), especially in the far-UV (bluewards of $\sim 0.2 \mu\text{m}$). Consequently, the UV emission lines (at least those bluewards of 0.35 μm) could have a more even contribution between star formation and an AGN.

While the LAE stacked spectrum in [G. Roberts-Borsani et al. \(2024\)](#) is remarkably similar to the UV spectrum of LRDs (after applying some attenuation, $A^V = 0.8$ mag) and even reproduces the emission lines bluewards of H β and [O III] $\lambda\lambda 4960, 5008$ (see middle right panel in [Figure 3](#)), it would not be able to explain the continuum redwards of $\sim 0.4 \mu\text{m}$. Some other component must contribute to these wavelengths, accounting for more than 70% of the flux at 0.6 μm , and even higher fractions at 0.75 μm (the limit of the LAE template). The spectra of LRDs in the optical and near-infrared present less structure than in the UV. The only prominent features (at the resolution of the prism) are the hydrogen Balmer lines, [O II] $\lambda 3728$, [O III] $\lambda 4960, 5008$ and [O III] $\lambda 4363$, [Ne III] $\lambda 3870$, the He I lines at 5877, 7067, and 10833 \AA , [NI] $\lambda 10400$ (seen in low ionization AGN, [R. Riffel et al. 2006](#)). The whole optical spectrum is very similar to the non-LAE stack in [G. Roberts-Borsani et al. \(2024\)](#), after applying a significant amount of reddening to reproduce the continuum ($A^V \sim 5$ mag using a [D. Calzetti et al. 2000](#) law). However, this large attenuation would produce a spectrum which is too red to fit the LRD beyond H α . The spectral slope for LRDs there would need a significantly lower attenuation to be reproduced by the non-LAE spectrum, around $A^V \sim 1.5$ mag.

We conclude that the UV part of the spectrum of LRDs seems dominated by star formation, more clearly in the far-UV, given the similarity with the H II region spectrum. The UV spectrum does not show the typical features and profile of QSOs. We cannot exclude

a priori emission from accretion disk and BLR in the near-UV (around 2600-3000 \AA). An AGN with a hotter accretion disk could be brighter than the [M. J. Temple et al. \(2021\)](#) template in the far-UV and reproduce the LRD UV slope more closely. The nature of the optical and the near-infrared emission is elusive, we cannot find a convincing agreement with empirical or theoretical single-component templates.

In the following sections, we analyze each spectral range separately, looking for clues about the nature of the typical (median) LRD.

3.2. UV range

As remarked in the previous section, the most prominent emission lines detected in the UV (i.e., the ones with higher equivalent width, EW), are C III] $\lambda 1908$, Mg II $\lambda 2798$, Ly α $\lambda 1216$, or He II $\lambda 1640$. Some fainter peaks might be identified with He II $\lambda 2733$, or C IV $\lambda 1549$.

In [Figure 4](#) we show a diagnostic diagram involving the most prominent of these UV lines, typical of both AGN and star-forming galaxies ([D. E. Vanden Berk et al. 2001](#)). The fluxes and equivalent widths of the lines in this plot were measured with the LIME software ([V. Fernández et al. 2024](#)), first determining the continuum with a spline fitting a set of anchor points constructed with the 5% lowest flux values in the 1200 to 2400 \AA region and using Gaussians with widths larger than those corresponding to the spectral resolution of the stack at each specific wavelength (see [Figure 3](#). For the He II measurement, a O III] $\lambda\lambda 1661, 1666$ component was also considered, which would be unresolved in our stacks given that the nominal spectral resolution is $R \sim 35$, $R \sim 50$ considering the improvement for point-like sources, corresponding to a FWHM of 33 \AA . The measurements include uncertainties in the determination of the continuum, which in fact are the main contributor given that the UV spectrum of LRDs (especially the reddest) presents significant structure.

The point for the stack of all LRDs (and also for the subtypes) lies near the boundary region between star-formation and AGN dominated galaxies according to the models presented in [K. Nakajima et al. \(2018\)](#). For the reddest LRDs (red hexagon), He II is not detected, so we provide a lower limit for the C III]/He II ratio. In general, all LRD types have very similar C III] and He II line emission as super star clusters at Cosmic Noon ([D. P. Stark et al. 2014](#); [E. Vanzella et al. 2017](#)).

3.3. Optical range

The optical range exhibits strong emission lines of the hydrogen Balmer series, [Ne III] at 3870 and 3969 \AA ,

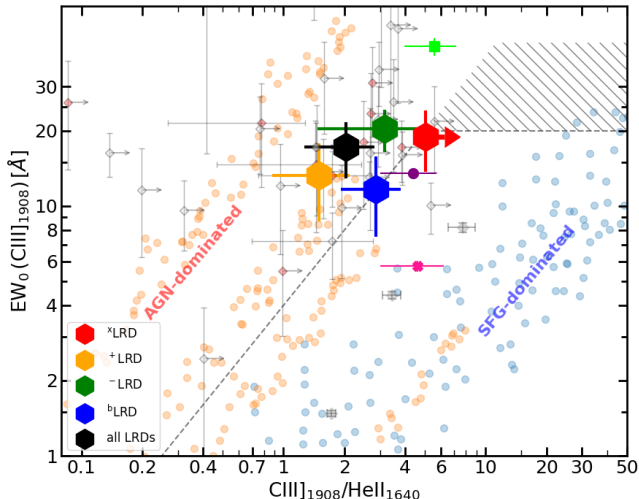


Figure 4. Position of the LRD median (black hexagon) in a UV line diagnostic plot comparing C III] EW *vs.* C III]/He II intensity ratio. We also show the measurements for different subtypes of LRDs (colored hexagons) based on optical-to-UV luminosity ratios, L_{5100}/L_{2500} , as defined in Section 2.4. We compare with a compilation of measurements for $z > 2$ galaxies, extracted from F. Arevalo-Gonzalez et al. (2025). In gray, we depict individual sources at $5 < z < 7$ (from that same paper -dots-) and at $2 < z < 4$ (from M. Llerena et al. 2022 -diamonds-). In lime, magenta and deep pink, stacks for strong, weak and non-detection C III] emitters are shown with crosses (F. Arevalo-Gonzalez et al. 2025). Models from K. Nakajima & R. Maiolino (2022) of AGN-dominated and star formation-dominated sources are shown with orange and blue symbols, also depicting the separation lines between them, as well as the hybrid region (dashed).

[O II] at 3728 Å (the doublet is not resolved), and [O III] at 4364, 4960, and 5008 Å, as well as He I at 5877 Å, and [O I] at 6302 and 6366 Å. There is also a very peculiar feature at 4555 Å, which we describe in the second subsection below.

3.3.1. Prominent emission in the WR blue bump

Apart from the bright lines, our stack shows some fainter lines in key spectral ranges. Figure 5 shows the region around the blue bump typical of Wolf Rayet (WR) stars. Several papers have claimed the detection of WR features at $2.5 \lesssim z < 6$ with JWST (T. E. Rivera-Thorsen et al. 2024; T. Morishita et al. 2025b; D. A. Berg et al. 2025). Our spectrum shows peaks at wavelengths consistent with N III $\lambda\lambda 4634, 4640$, N V $\lambda\lambda 4605, 4620$, and N III $\lambda 4511$ (also N IV $\lambda 1486$, not shown in Figure 5, but see Figure 3), as well as a strong bump which would correspond to broad He II $\lambda 4687$ emission. The detection of this line for LRDs has also been reported in B. Wang et al. (2025a), where they discuss a possible coexistence of an AGN and nu-

clear starbursts, a scenario supported and quantified in this section. Three even fainter lines compatible with Fe II $\lambda 4590$ and [Ar IV] $\lambda\lambda 4711, 4740$ are observed in the same region, although higher-resolution spectroscopy is required to confirm the identity of each individual feature in the prism blend. Some indication of faint carbon lines in this bump are visible, but are weaker than the nitrogen features. The potential presence of carbon could be confirmed by studying the WR red bump at around 5800 Å, produced by carbon emission, but our stack is inconclusive, due to the contamination of He I $\lambda 5877$ in our low spectral resolution data (see Figure 3).

Tentatively interpreting the spectral region around 4650 Å as a WR signature (i.e., the typical WR blue bump), and using all the lines mentioned above, we fitted the spectrum shown in Figure 5 with the LIME software (V. Fernández et al. 2024; we also checked the results obtained with the FANTASY code, D. Ilić et al. 2023). The continuum was measured in two ways. First, we used a power law between 4550 and 4770 Å. We repeated the power-law fit, this time using the 5% lowest flux values in the 4000 to 5650 Å range, given that there were indications of an absorption at ~ 4550 Å (see next section), and also because the red end of the WR bump is could be affected by the H β broad component. We show and discuss results with the second method, pointing that line fluxes change by $\sim 15\%$ when using the first continuum determination. We warn the reader that, even though the continuum in the optical shows less structure than in the UV, the determination of the continuum is the main uncertainty contributor to the line flux errors.

After the determination of the continuum, Gaussians placed at the wavelengths for emission lines in this spectral range. The widths of the lines were fitted for each line separately, allowing the He II line to have a wide and narrow component, while for the remaining lines only one narrow component was used. Fixing the width of all the narrow lines to be the same reached almost identical results. Based on the nominal NIRSpec spectral resolution, the instrumental σ we used is 16 Å, FWHM 38 Å, i.e., $R \sim 120$ (which is the median of all sources entering the stack at these wavelengths, the scatter being 30). However, the GTO Team is typically applying a $1./0.7 \sim 1.4$ multiplicative correction to the nominal NIRSpec spectral resolution (i.e., the one corresponding to the uniformly illuminated shutter), consistent with the findings by A. J. Shajib et al. (2025). Assuming the spectral resolution is indeed better than nominal (which should be the case for our point-like sources), the instrumental σ would be 12 Å (resolution $R \sim 170$).

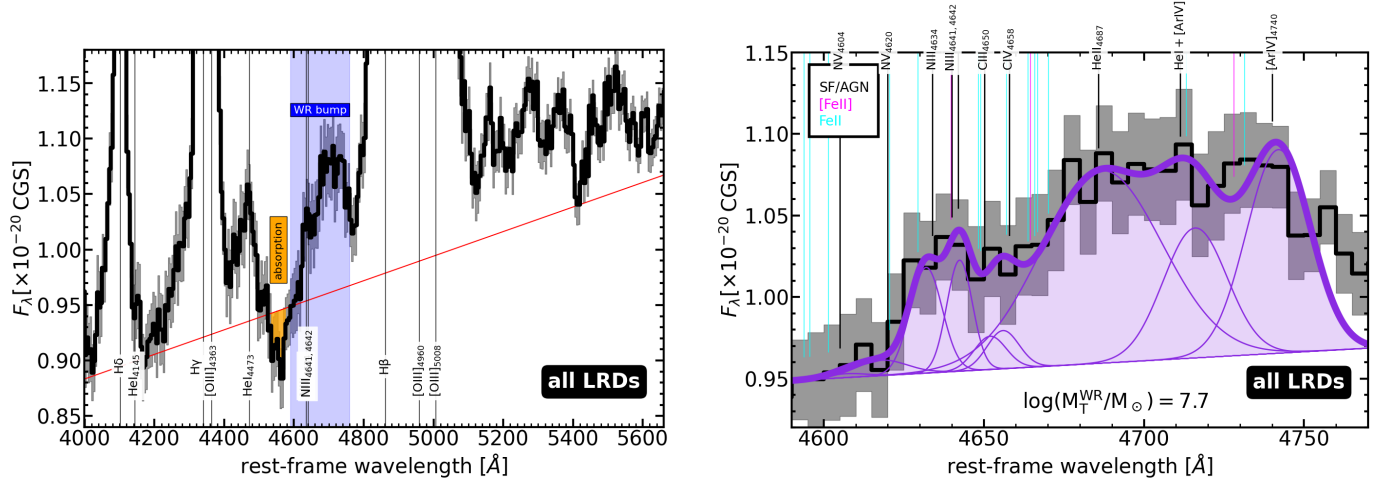


Figure 5. *Left:* Plot showing the estimation of the continuum emission around the WR blue bump (marked with a blue shade) for the stack of all LRDs, scaled in rest-frame flux to match the optical luminosity density at 5100 Å of the full spectroscopic sample for $z = 7$ (approximate median redshift of the photometric sample). The estimated continuum is shown with a red line. Several relevant spectral features are marked, including an absorption at 4550 Å (see Section 3.3.2 for details). *Right:* Spectral region around the WR blue bump. The stack of spectra for all LRDs (black line with errors represented by the gray shading) is fitted with Gaussians placed at the wavelengths of emission lines typical of this kind of massive stars and from AGN (marked with black vertical lines in the plot). The He II 4687 line is allowed to have a narrow and a wide component (the latter defined as $FWHM > 2000 \text{ km s}^{-1}$), and the intrinsic widths of the remaining lines are free. The continuum is measured as shown in the left panel. In cyan, we also depict the wavelengths for the Fe II line forest, and in pink the [Fe II] lines. The plot gives the calculated total mass of a starburst explaining the He II emission in terms of WR stars (WN subtype).

As a reference, for the [O III] $\lambda\lambda 4960, 5008$ lines, for which we have very good signal-to-noise ratio (SNR), we measure σ around 13 Å, which gives $R \sim 160$. The nominal resolution for the stack at 0.5 μm is $R = 130$, 1/0.9 with respect to the 160 value given before. If we consider the 0.7 correction in A. J. Shajib et al. (2025), those narrow lines would be slightly resolved (or close to resolved). In any case, we conclude that the calculations about the resolution used for Figure 5 (and throughout the rest of the paper) are robust, running on the conservative side.

The fits shown in Figure 5 would favor the presence of nitrogen-rich Wolf-Rayet (WN) stars rather than carbon-rich WC stars (P. A. Crowther 2007), which could be linked to the high nitrogen abundances seen in many high redshift galaxies (A. J. Bunker et al. 2023; A. J. Cameron et al. 2023; R. Marques-Chaves et al. 2024; D. Schaerer et al. 2024; X. Ji et al. 2024; D. A. Berg et al. 2025), also in the LRD in X. Ji et al. (2026a). This characteristic has been claimed to be linked to spatial compactness (M. W. Topping et al. 2024). Our fits indicate $\sigma = 1130 \pm 310 \text{ km s}^{-1}$ (intrinsic) for the He II line, which is a typical value in nearby and intermediate redshift WR galaxies (J. Brinchmann et al. 2008; Á. R. López-Sánchez & C. Esteban 2010; X. H. Han et al. 2010). This value is 25% smaller than the broad component we measure for H β , compatible within errors, thus we cannot rule out that the He II line is linked to an

AGN (if the Balmer lines are dominated by nuclear activity). The rest-frame equivalent width is $\sim 6 \text{ Å}$. The width is comparable to some of the highest values measured for WR galaxies in the local Universe by W. D. Vacca & P. S. Conti (1992); the galaxy with the most extreme line in this paper has twice the EW of our stack. We also compare with J. Brinchmann et al. (2008), who studied WR galaxies based on the “blue bump” EW, adding all lines together; in our case we measure an EW of 13 Å for the whole “blue bump” (although we also include He I and Ar IV lines in the calculation, so not directly comparable), comparable to the most extreme WR galaxies in this work. Finally, our measurements can also be compared with D. Schaerer & W. D. Vacca (1998), who find that our “blue bump” EW could only be reached in a very narrow range of ages (around 4 Myr) for $0.4 Z_{\odot}$ galaxies and for more extended periods at higher metallicities.

Translating the flux of this broad emission line to stellar content by using the typical luminosity of local low metallicity late-type Wolf-Rayet nitrogen stars (WNL, P. A. Crowther & L. J. Hadfield 2006), assuming the WNL to O-type stellar ratio in (D. Schaerer & W. D. Vacca 1998), and a Chabrier IMF to calculate the total mass of the starburst responsible for this emission, we would obtain a total mass of $M_{\star} = 10^{7.7 \pm 0.3} M_{\odot}$. This stellar mass is consistent with the values obtained from clustering analysis in J. Matthee et al. (2025),

$10^{7.7 \pm 0.3} M_{\odot}$, as well as with dynamical mass constraints (B. Wang et al. 2024; I. Juodžbalis et al. 2024; F. D’Eugenio et al. 2026a, 2025).

We note that the WR interpretation would need a detection of broad He II $\lambda 1640$, with a typical Case-B ratio with respect to He II $\lambda 4687$ of 7.8 (C. Leitherer et al. 2019). The He II $\lambda 1640$ is well detected in our stack (SNR ~ 10), but the spectral resolution of the prism is low in the rest-frame UV, so we cannot study the line profile. Assuming the entire line flux comes from a broad component, we obtain $F(\text{He II}_{1640})/F(\text{He II}_{4687}) = 3.5 \pm 0.4$, which would imply 0.9 mag attenuation between the two wavelengths, translating to $A^V \sim 1$ mag with the D. Calzetti et al. (2000) dust law. This value is similar to that applied to the LAE stacks discussed in Figure 3, and the SED fitting exercise described in Section 5.1.

3.3.2. Unknown absorption feature at 4550 Å

Our stack and spectral analysis (including the fit of the continuum in the 3000-6000 Å range) also highlight the presence of a strong absorption feature near 4550 Å (Figure 5, left). This feature can be observed in most LRDs with adequate SNR (I. Labbé et al. 2024; R. Tripodi et al. 2025b), but was initially interpreted as lack of emission infill from the broad permitted Fe II (see e.g. the models presented in I. Labbé et al. 2024). However, deep higher-resolution spectroscopy confirmed the surprising absorption nature of this dip (X. Ji et al. 2026b; F. D’Eugenio et al. 2025), even though both works did not report a clear identification.

While LRDs are known to display strong hydrogen and helium absorption (e.g., J. Matthee et al. 2024; B. Wang et al. 2025b; I. Juodžbalis et al. 2024; F. Loiacono et al. 2025; F. D’Eugenio et al. 2025), no known H or He feature matches 4550 Å. Metal absorption features have been observed in many individual LRDs, both in the rest-frame optical starting from Na I and Ca II at $z \sim 2$ (I. Juodžbalis et al. 2024), to Ca I, Fe I, Fe II, Ba II, K I at $z \sim 0.1$ (X. Lin et al. 2025; X. Ji et al. 2026b), and Ca II and Na I at $z \sim 7$ (F. D’Eugenio et al. 2025); as well as in the rest-frame UV (Fe II UV1–UV3, F. D’Eugenio et al. 2025; A. Torralba et al. 2025).

The widespread observation of metal absorption in the spectra of LRDs suggests that the 4550-Å dip may also be related to metal absorption. Given the common presence of neutral and low-ionization species, an identification with one or more of Fe II, Ba II, Fe I may be credible, even though it remains to be seen whether these transitions are consistent with what is seen (or absent) in other regions of the optical spectrum.

Among the possibilities, the most plausible alternative is a link to Fe II emission. The region around

4550 Å is covered by the Fe II F-band (e.g., J. Kovačević-Dojčinović et al. 2025), which in fact is used (compared to H β emission) to estimate Eddington ratios (T. A. Boroson & R. F. Green 1992). The Fe II emission at these wavelengths have been claimed to be very weak and possibly a sign of metal-poor BLRs at high redshift (B. Trefoloni et al. 2025). However, we identify with Fe II some strong emission in the UV and in the 5300 Å region (the G band in J. Kovačević-Dojčinović et al. 2025), thus the absorption would be rather linked to high gas densities, low ionization parameters (J. Kovačević et al. 2010), or depletion of iron into dust grains (G. A. Shields et al. 2010). Weak F-band emission compared to the G-band is common in AGN with high Balmer decrements (J. Kovačević et al. 2010), as is observed for LRDs.

An intriguing alternative is represented by molecular absorption, since at least two studies reported the presence of G-band absorption at 4300 Å (X. Ji et al. 2026b), a feature typical of low-temperature stars and attributed to CH. However, we found no suitable match with equally abundant diatomic molecules, NH, OH, and H₂. Strong absorption in this region is also found in supergiants (see, e.g., S. A. Korotin et al. 2015).

Currently, the main hurdle preventing a secure identification is the trade-off between high-SNR, low-resolution prism data (as seen in our stack) and high-resolution, low-SNR grating data. Deep, higher resolution spectroscopy is required to securely identify this feature. In any case, its omnipresent appearance over most of the LRD range $z = 0.1$ –7 strongly supports the presence of metals, as well as a warm or cool gas medium capable of supporting low-ionization species.

3.4. Near-infrared range

Our NIRSpec stack is significantly noisier in the near-infrared compared to bluer wavelengths. However, significant peaks are detected in several Paschen lines, in He I at 1.083 μm , and [S III] at 9071 and 9533 Å.

Using MIRI imaging, we extend the stacked SED of the full LRD sample to rest-frame wavelengths of $\sim 4 \mu\text{m}$, as shown in Figure 6 (magenta points). The stacked SED with the MIRI extension shows a clear flattening beyond $\sim 2 \mu\text{m}$, in excellent agreement with, and smoothly extending, the NIRSpec continuum (see also Figure 3 for a zoom-in to $\sim 1.2 \mu\text{m}$). This trend confirms previous photometric results indicating that LRDs exhibit moderate near-IR colors (e.g., P. G. Pérez-González et al. 2024a; C. C. Williams et al. 2024; H. B. Akins et al. 2025b; C. M. Casey et al. 2024; K. Ronayne et al. 2025), in contrast to the steeply rising continua of

obscured type-1 QSOs. The trend is now verified in a sample of spectroscopically confirmed LRDs.

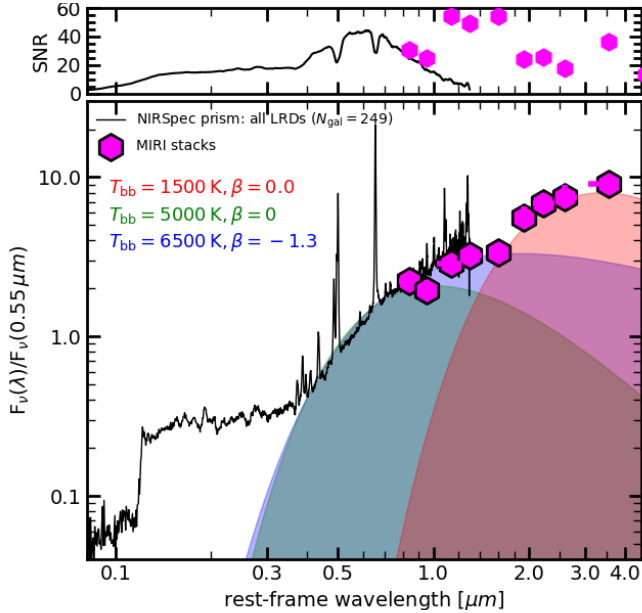


Figure 6. Same as Figure 3, showing the LRD stacked spectrum extended to $\sim 4 \mu\text{m}$ using MIRI data (magenta points and error bars, showing the median and scatter). The shaded blue and green regions illustrate two MBBs fitting the rest-frame optical part of the spectrum, as in A. de Graaff et al. (2025b) and H. Umeda et al. (2025); we use representative parameters for the variety of LRDs, from the hot (6500 K) to the cold end (5000 K). Neither can reproduce the MIRI photometry at $\lambda > 1.5 \mu\text{m}$, suggesting the presence of hot dust emission. This spectral region covered by MIRI is fit to another MBB, at 1500 K (in red).

At longer wavelengths, the MIRI detections reveal a mild upturn beyond $\sim 2 \mu\text{m}$, producing a rest-frame color of $[1-3 \mu\text{m}] \sim 1.25 \text{ mag}$, comparable to the median $[1-3 \mu\text{m}] = 1.5 \text{ mag}$ measured for the F1800W-detected LRDs in G. Barro et al. (2026). While these colors are not extremely red, they suggest the presence of hot dust, with characteristic temperatures of $T \sim 1500 \text{ K}$. As discussed in G. Barro et al. (2026, see also G. C. K. Leung et al. 2025 and K. Ronayne et al. 2025), in the absence of dust, the near-infrared continuum of either a stellar population or a standard AGN accretion disk would be significantly bluer, with $[1-3 \mu\text{m}] \sim -0.5 \text{ mag}$. The emission of a dust torus, represented in Figure 6 by a $T \sim 1500 \text{ K}$ blackbody, peaks around $3 \mu\text{m}$ (in f_ν , $2 \mu\text{m}$ in f_λ), making the SED redder. The observed colors therefore imply a substantial hot-dust contribution, corresponding to a fraction of the total emission of $f_{3\mu\text{m}}^{\text{HD}} \sim 50-80\%$ (see Figure 8 of G. Barro et al. 2026).

In the context of more recent black hole star (BH^{*}) or black-hole-envelope (BHE) models (R. P. Naidu et al.

2025; D. Kido et al. 2025; A. de Graaff et al. 2025b, see also K. Inayoshi & R. Maiolino 2025 where the argue in favor of the presence of dense gas in LRDs, but not necessarily as a BHE or BH^{*}), which mathematically parameterize the continuum using modified blackbodies (MBBs), the requirement for hot dust becomes even stronger. Note that MBBs are generally employed to model dust emission, where dust-grain emissivity in the Rayleigh-Jeans tail behaves like a powerlaw (B. T. Draine 2006), while – in the context of LRDs and optical emission – a MBB has to be considered as an effective shape function, given that for $T \sim 5000 \text{ K}$, thermal emission is dominated by gas, not dust. The MBB SED with temperatures $T \sim 5000 \text{ K}$ declines rapidly toward the near-infrared, predicting much bluer $[1-3 \mu\text{m}]$ colors. This is illustrated in Figure 6 by two MBB models: first, a true blackbody model with $T = 5000 \text{ K}$, $\beta = 0$ (green shaded region), representative of the best-fit results in A. de Graaff et al. (2025b) for spectroscopic LRDs at $z < 4.5$; and second, a MBB $T = 6500 \text{ K}$, $\beta = -1.3$ model (purple shaded region). These MBBs correspond to our best fits to the stacked NIRSpec spectrum using the optical regions described in A. de Graaff et al. (2025b), i.e., without using the MIRI photometry. While the latter reproduces the flattening at $\lambda \sim 1-2 \mu\text{m}$, it predicts a near-zero $[1-3 \mu\text{m}]$ color, significantly bluer than observed. This discrepancy demonstrates that even within MBB-based BH^{*} frameworks, an additional hot-dust emission component (or another emitting source with cooler temperatures) is required to match the MIRI constraints (see, e.g., G. Barro et al. 2026; I. Juodžbalis et al. 2024; I. Delvecchio et al. 2025; X. Ji et al. 2026b). We illustrate this effect in Figure 6 by plotting a $T \sim 1500 \text{ K}$, $\beta = 0$ MBB (in fact, a pure BB) fitting the MIRI data. This dust emission with small β is typical of very large grains, commonly found in dense environments such as AGN tori given that they can survive in harsh environments (e.g. R. Maiolino et al. 2001), as well as iron bearing grains (E. Dwek 2016). This type of dust typically produces gray attenuation laws, which have been claimed to be needed to reproduce the (UV) SED of LRDs (e.g., G. Barro et al. 2024; P. G. Pérez-González et al. 2024a). See the Discussion section for more details about the possible presence of dust in LRDs.

4. THE DIVERSITY OF LITTLE RED DOTS: STACKS OF DIFFERENT SUBTYPES

To advance our understanding of LRDs, in this section we analyze stacked spectra of the several subsamples presented in Section 2.4 constructed in terms of the optical-to-UV luminosity density ratio, L_{5100}/L_{2500} .

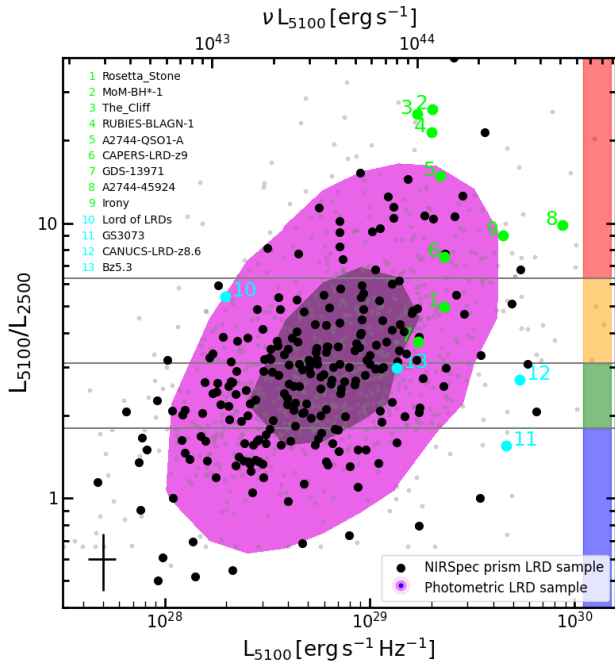


Figure 7. Optical-to-UV luminosity density ratio *vs.* optical luminosity density for the parent sample of photometrically selected LRDs (gray dots, purple regions showing $1,2\sigma$ loci) and the spectroscopic sample of LRDs characterized in this paper (black and lime points). A scale in energy units νL_ν for the x-axis is given. The gray lines separate the sample as a function of optical-to-UV luminosity ratio in 4 subtypes, which are represented by vertical shaded rectangles: extreme L_{5100}/L_{2500} LRDs (x LRDs, red shade), above-median L_{5100}/L_{2500} LRDs ($^+$ LRD, orange), sub-median L_{5100}/L_{2500} LRDs ($^-$ LRDs, green), and blue L_{5100}/L_{2500} LRDs (b LRD, blue). Some interesting LRDs presented and characterized in individual papers are marked in lime (for sources included in our sample) and cyan (for sources not in our sample because they are not in our fields or do not have MSA data -but IFU observations-), identified with a number. The Rosetta Stone LRD comes from I. Juodžbalis et al. (2024), MoM-BH*-1 from R. P. Naidu et al. (2025), The Cliff from A. de Graaff et al. (2025a), RUBIES-BLAGN-1 from B. Wang et al. (2024), A2744-QSO1-A from L. J. Furtak et al. (2023, see also X. Ji et al. 2025), CAPERS-LRD-z9 from A. J. Taylor et al. (2025b), GDS-13971 from J. Matthee et al. (2024), A2744-45924 from I. Labbé et al. (2024), Irony from F. D’Eugenio et al. (2025, also in B. Wang et al. 2024; E. Lambrides et al. 2025; M. Tang et al. 2025; K. Ronayne et al. 2025; B. Wang et al. 2025a), GS3073 from H. Übler et al. (2023, see also X. Ji et al. 2024 and G. Venturi et al. 2025), CANUCS-LRD-z8.6 (R. Tripodi et al. 2025a), and Bz5.3 (R. Tripodi et al. 2025b).

Figure 7 shows this ratio compared to the optical luminosity density, L_{5100} . The median value and 1σ scatter of L_{5100}/L_{2500} for the whole spectroscopic sample is $3.1_{1.8}^{6.3}$. The figure clearly shows that there is a trend for more luminous LRDs to be redder, and the bias of LRDs

discussed individually in different papers (see caption for references) to be at the bright end of the distribution.

The stacked spectra for the four subsamples defined in Section 2.4, x LRD, $^+$ LRD, $^-$ LRD, and b LRD, are shown in Figure 8.

In the following subsections, we quantify and discuss some relevant spectroscopic properties of LRDs based on our general stack and the stacks for the different subtypes. We present an analysis of some interesting spectral regions. The main measurements used in the rest of the paper are compiled in Table 3.

The spectra shown in Figures 9 to 11 were fitted to nebular emission from hydrogen, helium, and metals with the FANTASY code (D. Ilić et al. 2023). Among those metals, we emphasize that FANTASY considers iron line complexes, which are very relevant in the analysis of AGN. The fitting procedure follows. First, we subtracted a continuum calculated from anchor points identified among the 5% lowest fluxes in the spectral region of interest. Then, the fits were performed by considering a narrow component for hydrogen, helium, and all metals except iron (e.g., oxygen for Figure 9), an independent broad component for hydrogen and helium, and a final independent (with their own width) component for Fe II lines, all sharing the same velocity shift.

4.1. Ubiquitous iron emission

The ubiquity of singly ionized iron, Fe II, lines in AGN in the optical was discovered in the very first QSOs and prototypical AGNs such as I Zw 1 (E. J. Wampler & J. B. Oke 1967; W. L. W. Sargent 1968; B. J. Wills et al. 1985). There are several other spectral regions where these emission complexes are very prominent in type-1 AGN, including the UV, red optical, and near-infrared.

Figure 9 shows the spectra of the different types of LRDs in the region around the $H\beta$ emission line, covered by the “optical Fe II lines”⁵⁰. This spectral range shows a distinctive signal from multiple Fe II lines forming a pseudo-continuum in AGN (e.g. J. Kovačević et al. 2010). The lines (marked with vertical cyan lines in the plot) are organized in this region in three groups, one for each of the lower transition levels of Fe II: the F lines around 4550 Å (also found in AGN at high redshift observed with JWST; B. Trefoloni et al. 2025), the S lines around 5000 Å, and the G lines around 5200 Å. Further Fe II emission extends bluewards down to 4100 Å, in a group that J. Kovačević-Dojčinović et al. (2025) quali-

⁵⁰ We note that this spectral region includes the WR blue bump treated in Section 3.3, which will be discussed for LRD subtypes in the next section.

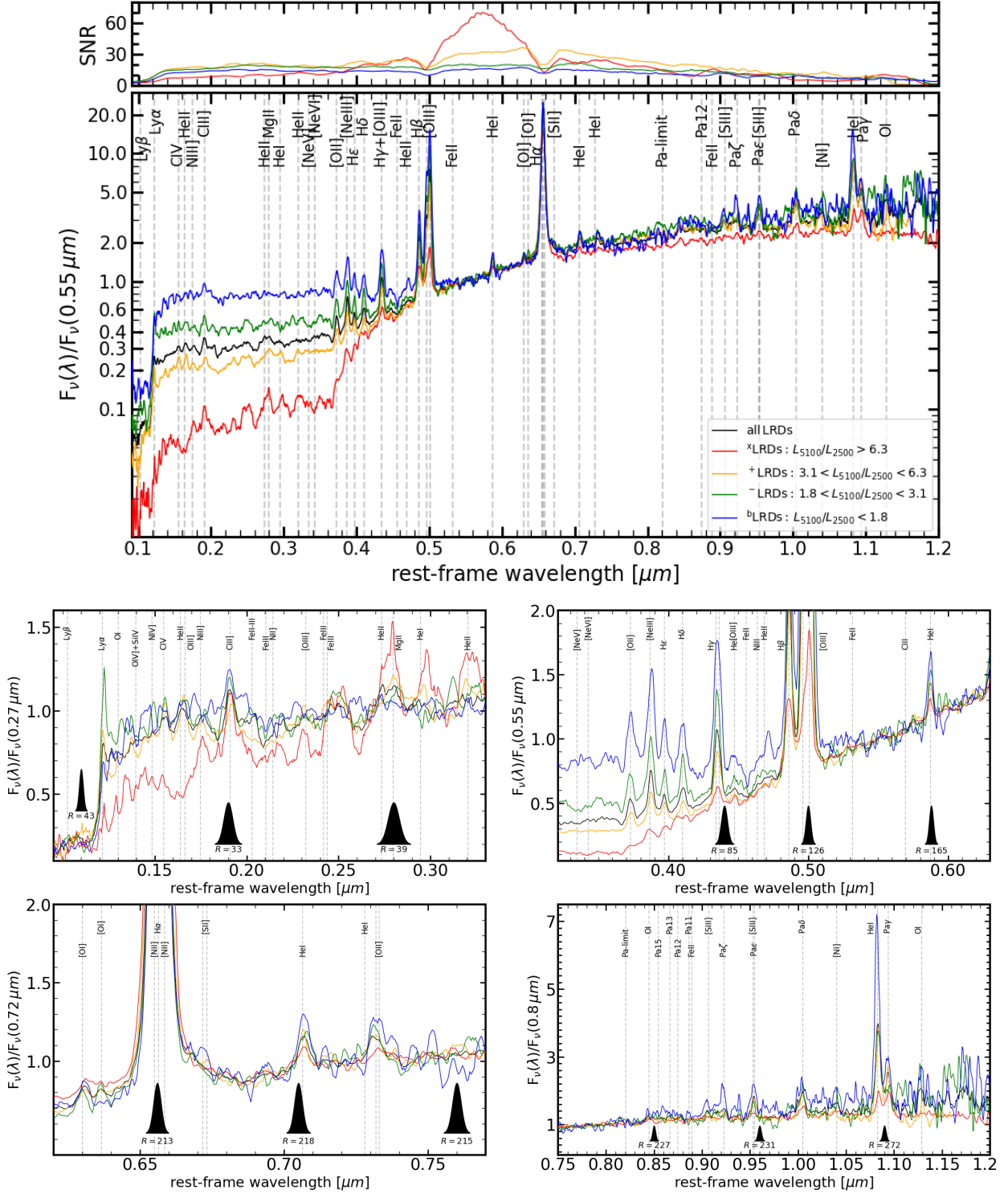


Figure 8. Stacks of LRDs divided by their optical-to-UV luminosity ratio, L_{5100}/L_{2500} . x LRDs, ($L_{5100}/L_{2500} > 6.3$), are shown in red; $^+$ LRDs, $2.7 < L_{5100}/L_{2500} < 6.3$, are shown in orange; $^-$ LRD, $1.4 < L_{5100}/L_{2500} < 2.7$, are shown in green; and b LRDs, $L_{5100}/L_{2500} < 1.4$, are shown in blue. In the main panel, all spectra are normalized to $0.55 \mu\text{m}$. In the bottom panels, we zoom into several spectral ranges. To make the comparison easier, we normalize the four spectra to different wavelengths in each panel (specific value shown in the y-axis label). The varying spectral resolution is shown with Gaussians in each zoomed-in panel, providing the average of the four stacks at each wavelength.

fies as inconsistent Fe II lines based on the fact that they are clearly seen in spectra of AGN despite their low transition probabilities (H. Netzer & B. J. Wills 1983; E. M. Verner et al. 1999; F. Bruhweiler & E. Verner 2008), and also jointly with some semi-forbidden and forbidden lines of Fe arising from higher levels of excitation. In our low spectral resolution data, the consistent lines around 5300 Å are the most visible, given that the spectral region from 4000 to 5000 Å is dominated by strong nebular lines from hydrogen and oxygen and the identification of iron lines is more challenging.

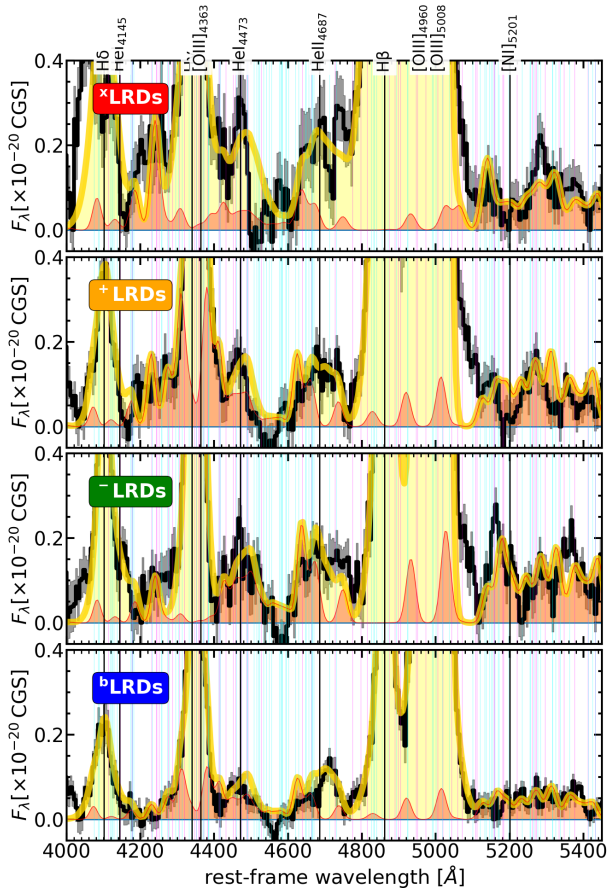


Figure 9. Spectra of the different types of LRDs in the optical Fe II region. The continuum has been subtracted by fitting a spline to a set of anchor points constructed with the 5% lowest flux values in the region. The spectra have been expanded in intensity to emphasize the faint lines, mainly forming a pseudo-continuum created by Fe II emission. As the legend on the top right indicates, the main hydrogen, helium and oxygen lines (typical of SFG and AGN) are marked in black, and the Fe II lines (consistent, inconsistent, semi-forbidden, and forbidden, see J. Kovačević-Dojčinović et al. 2025) are marked in cyan and magenta. The fit to the spectra performed with the FANTASY code (D. Ilić et al. 2023) is shown in gold (all components) and red (Fe contribution).

4.2. Fe II and Eddington Ratios

All different LRD types present Fe II emission, which is more prominent in the reddest sources. The Fe II emission has been shown to correlate with the Eddington ratios in nearby AGN and QSOs (see, e.g., D. Ilić et al. 2023). For the reddest LRDs, information about Eddington ratios can be extracted from UV line ratios involving Fe II and Mg II, as shown in Figure 10. For the \times LRDs, we measure a line ratio Fe II/Mg II = 11.3 ± 2.8 ⁵¹. This value is comparable to the most luminous QSOs (e.g., R. Maiolino et al. 2003; M. Dietrich et al. 2003). Using the compilation of different types of AGN presented in X.-B. Dong et al. (2011, see also J. Shin et al. 2019, 2021), that line ratio would translate to $\lambda_{\text{Edd}} = 0.6 \pm 0.2$. A similar Eddington ratio is obtained for the $+$ LRDs and $-$ LRDs, for which we measure Fe II/Mg II = 10.2 ± 2.7 and 12.0 ± 3.0 , translating to $\lambda_{\text{Edd}} = 0.5 \pm 0.2$ and 0.6 ± 0.2 , respectively. We conclude that LRDs present relatively high accretion ratios, but not super-Eddington (see Y. Pang et al. 2026).

Another estimation of the Eddington ratio can be performed using the results in J. Kovačević-Dojčinović et al. (2025), who present a correlation between the Eddington ratio and the ratio of the Fe II intensities in the UV and the optical. We find a optical-to-UV intensity ratio (using only the consistent lines in the optical, and the group-60 Fe II lines in the UV, as done in the paper referenced above) of 3.8 ± 1.5 for \times LRDs (this is a direct measurement without any correction for dust attenuation). This would translate to $\lambda_{\text{Edd}} \sim 0.6$ based on Figure 10 in J. Kovačević-Dojčinović et al. (2025), given that our value would be in between group 4 and 5 in that plot. Similar calculations place $+$ LRDs and $-$ LRDs in groups 3-4 in the figure in J. Kovačević-Dojčinović et al. (2025), which implies $\lambda_{\text{Edd}} = 0.2 - 0.6$.

LRDs are very weak in the X-ray (e.g., M. Yue et al. 2024; D. D. Kocevski et al. 2025; R. E. Hviding et al. 2026). This property is shared with high-redshift moderate-luminosity AGNs in general (e.g., R. Maiolino et al. 2024), for which a median Eddington ratio of ~ 0.4 has been found (e.g., Y. Harikane et al. 2023b; V. Kokořev et al. 2023; R. L. Larson et al. 2023; R. Maiolino et al. 2024). This value is consistent with the ones we have deduced for LRDs from their Fe II emission.

As an alternative, F. Pacucci & R. Narayan (2024) have suggested that the weak X-rays may indicate mildly super-Eddington emission with Eddington (mass) ra-

⁵¹ Following X.-B. Dong et al. (2011), the Fe II emission is integrated from 2200 to 3090 Å.

the He II $\lambda 4687$ line are similar in all the LRD subtypes except for the bluest. If interpreted as a WR signature, the stellar masses of a recent burst would range from $10^{7.4}$ to $10^{8.0} M_{\odot}$.

4.4. Line ratios and Balmer break

Figure 12 shows how the optical-to-UV luminosity ratios used in our paper to distinguish different types of LRDs correlate with spectral features.

The most extreme LRDs (around 15% of the population) are characterized by large Balmer breaks (not compatible with stellar properties, see A. de Graaff et al. 2025a, R. P. Naidu et al. 2025 or A. J. Taylor et al. 2025b). The rest show more moderate values of the Balmer break amplitude, around 1.0-1.5 with a slight trend for redder sources to present larger Balmer breaks; all the values around 1.0-1.5 could in principle be explained with stars.

The hydrogen line ratios also correlate with L_{5100}/L_{2500} . Interpreted as dust attenuation, the Balmer decrements would mean an increasing dust content as we move to redder LRDs, with A^V values changing from 0.2 to nearly 3 mag. However, in the scenario invoking dense gas enshrouding a SMBH to explain LRDs (see, e.g., K. Inayoshi & R. Maiolino 2025), the Balmer line ratios are significantly affected by radiative transfer processes such as Thomson, Raman, and resonance scattering (S.-J. Chang et al. 2026), so this dust content estimate should be taken with caution. Indeed, in a few cases where accurate narrow-broad line decomposition has been performed, the observed line ratios seem inconsistent with standard dust attenuation (F. D'Eugenio et al. 2025; G. P. Nikopoulos et al. 2025), favoring instead collisional excitation.

In our stacks, the behavior of the hydrogen line ratios is not-standard for case-B and dust interpretations. As noted by several authors (A. de Graaff et al. 2025b; G. Barro et al. 2025), the $H\alpha/H\beta$ ratios is larger for the reddest LRD, reaching values as high as 10 and above. We measure the same increase for $H\beta/H\gamma$ and $H\beta/H\gamma$. In our stacks, we are able to measure the $H\beta/Pa\gamma$ ratio, obtaining values around 2–3, which are very different from the ~ 11 value expected for case-B recombination. Taking the results from (S.-J. Chang et al. 2026), we infer that the small values we measure for $H\beta/Pa\gamma$ would be consistent with column densities of hydrogen atoms in the 2s state of nearly 10^{14} cm^{-2} , consistent with the high Balmer decrements.

A further interesting measurement in our stacks linked to radiative transfer effects is the relationship between $H\alpha$ and $H\beta$ widths. For x LRDs, we $H\beta$ is broader than $H\alpha$ by 20%, a very similar value to that observed for

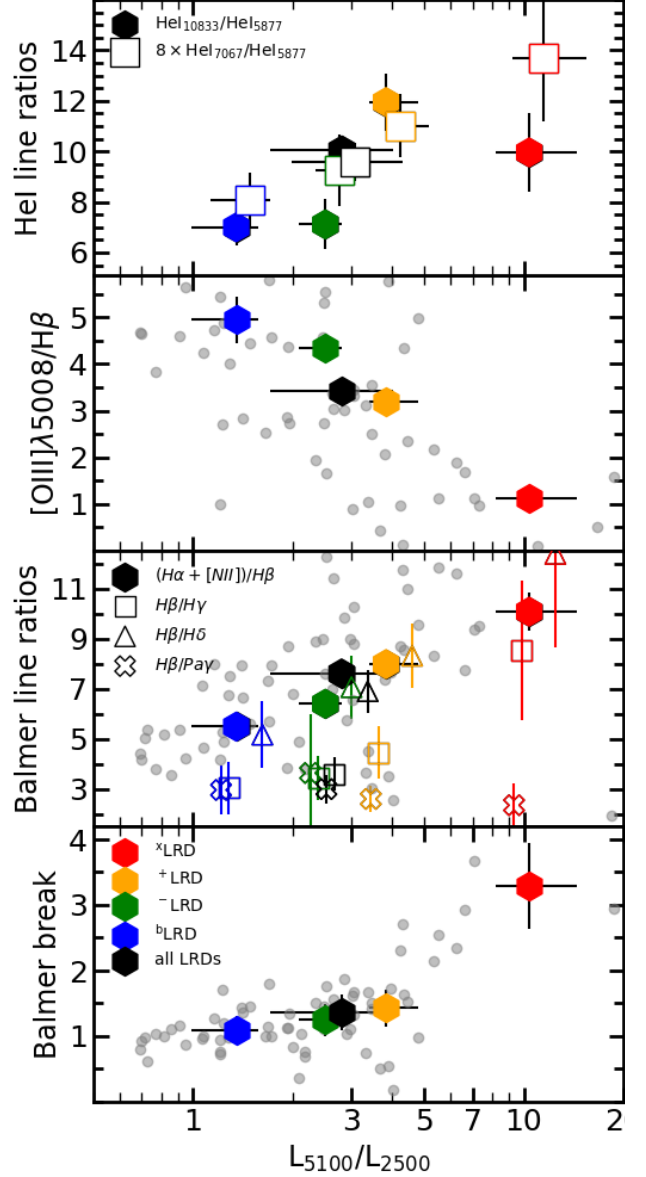


Figure 12. Correlation of spectroscopic features with the optical-to-UV continuum luminosity ratios. x LRDs are shown in red, $^+$ LRDs in orange, $^-$ LRDs in green, and b LRDs in blue. In the panels showing several point sets, each one of them is offset in the x-axis for clarity. Top panel shows the ratio between several He I lines in the optical and infrared (multiplied by a factor to plot them in the same scale). The panel below depicts the ratio between $[OIII]\lambda 5008$ and the integrated flux of $H\beta$ (including broad and narrow components). The middle panel shows the Balmer decrement for the full flux of the hydrogen lines and for the broad component alone (symbols with thick black edge, artificially offset in the x-axis for clarity). Errors in the y-axis depict measurement uncertainties, in the x-axis they refer to scatter of the luminosity ratio. The bottom panel shows the Balmer break. In all panels, measurements for individual LRDs based on DJA catalogs and presented in G. Barro et al. (2025) are shown as grey dots.

QSOs and classical AGN (J. E. Greene & L. C. Ho 2005). However, for the bulk of the LRD population, $^+$ LRDs and $^-$ LRDs, we measure larger widths for $H\alpha$, the average ratio being $\text{FWHM}(H\beta)/\text{FWHM}(H\alpha) = 0.6 \pm 0.1$. As discussed in S.-J. Chang et al. (2026), this level of discrepancy in the width of the two brightest Balmer lines is expected in Raman scattering (see M. Kokubo & Y. Harikane 2025). We, however, warn the reader that disentangling and interpreting the different line components in a stacked spectrum is complex, given that objects with different line widths and contributions from narrow and broad components are mixed together, and some other effects such as self-absorption might be present for some sources entering the stack and affect the measurements in low spectral resolution data.

Figure 12 also shows the correlation between $[\text{O III}]\lambda 5008/H\beta$ and L_{5100}/L_{2500} , revealing a clear trend in which redder LRDs exhibit systematically lower $[\text{O III}]/H\beta$ ratios. At face value, this behavior could be interpreted in terms of metallicity variations or density effects, particularly if the gas density exceeds the critical density of $[\text{O III}]$ ($\sim 10^5 \text{ cm}^{-3}$), leading to collisional suppression of the line. Variations in ionization state and in the relative contributions of broad and narrow $H\beta$ components may also contribute.

An alternative, and likely complementary, explanation is that the observed line-ratio trend reflects the changing relative contribution of the galaxy host and the LRD core along the color sequence. In this picture, $[\text{O III}]/H\beta$ increases toward bluer LRDs as the stellar host contributes more strongly to both the continuum and the narrow-line emission. As shown in A. de Graaff et al. (2025b), G. Barro et al. (2025), and W. Q. Sun et al. (2026), this interpretation is supported by the systematic rise in the equivalent width of $[\text{O III}]$ toward bluer systems, consistent with a growing prominence of host-galaxy emission relative to the LRD core. Within this framework, the low $[\text{O III}]/H\beta$ ratios observed in the reddest LRDs arise primarily from strong broad $H\beta$ emission combined with weak or suppressed narrow-line emission from the host, rather than requiring extreme metallicity or density conditions alone.

The effect of dense gas is also noticeable in the He I line ratios plotted in the top panel of Figure 12. Our stacks show high-SNR detections of three He I lines in the optical and near-IR, namely $\text{He I}\lambda 5877$, $\text{He I}\lambda 7067$ and $\text{He I}\lambda 10833$. These lines, especially the latter, but also $\text{He I}\lambda 7067$, are highly sensitive to electron density and temperature, as well as optical depth (see D. A. Berg et al. 2026, , and also R. L. Porter et al. 2012). The LRD subtypes differ significantly in the He I, which are, in general, relatively high. Qualitatively (a quantitative

approach is delayed to a future publication), they indicate high electron densities, $n_e > 10^5 \text{ cm}^{-3}$, optically thick material for He I lines, and temperatures around 5000-7000 K.

5. MODELING THE BH AND STELLAR CONTINUUM PROPERTIES OF THE LRDS

In this section, we model the spectral stacks to infer stellar and black hole masses, as well as monochromatic and bolometric luminosities, and examine the correlations among these properties. We use two approaches, described in the next two subsections.

5.1. The two-component LRD-core plus galaxy-host SED model

We model the SEDs of LRD subtypes using a two-component framework consisting of a stellar host and an “LRD core”. The latter captures the red, steep optical continuum, the strong Balmer break, and the characteristic V-shaped UV–optical slope observed in LRDs. This Balmer-break component is likely associated with a dense gas envelope that helps reddening the intrinsic emission, even with little or no dust extinction. The detailed nature of this LRD core remains uncertain and may be linked to a BH* or BHE, or very compact and intense gas-rich starburst with the possible presence of a super-massive star (or several). In our analysis, we remain agnostic about its physical nature, and use a template for this component (see below).

The primary motivation for this approach is that previous two-component SED models combining stellar hosts with standard AGN templates (such as those from, e.g., M. J. Temple et al. 2021) failed to reproduce the strong (large amplitude) yet smooth Balmer break observed in LRDs (e.g.; Y. Ma et al. 2025b). In fact, stellar atmospheres have either smooth but weak breaks (with microturbulence up to $10\text{--}15 \text{ km s}^{-1}$; K. C. Smith & I. D. Howarth 1998), or strong but sharp breaks (typical of A-type stars; see F. D’Eugenio et al. 2026a for a discussion in the context of LRDs). In contrast, models where the Balmer break is due to dense gas (K. Inayoshi & R. Maiolino 2025) can reproduce both the observed break strength in LRDs, as well as its smoothness, provided the break itself is smoothed by high turbulence ($v \sim 100 \text{ km s}^{-1}$; X. Ji et al. 2025; R. P. Naidu et al. 2025; A. de Graaff et al. 2025a). Models combining a stellar host with an LRD core exhibiting a pronounced break successfully reproduce the composite spectra (see, e.g., R. P. Naidu et al. 2025; H. Umeda et al. 2025; G. Barro et al. 2025).

We use an empirical LRD-core template based on the x LRD spectrum, which exhibits the most pronounced

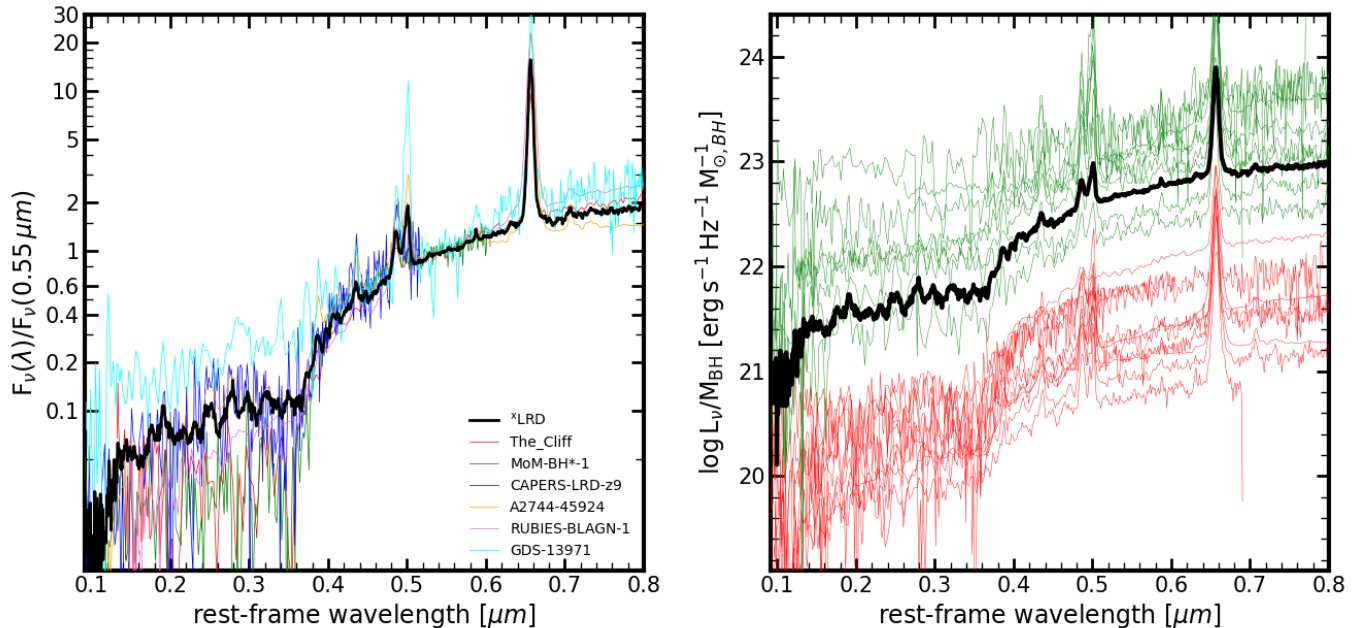


Figure 13. *Left:* Spectrum of the extreme LRDs in our paper (in black), compared to individual sources (see caption of Figure 7 for references), all normalized to $0.55 \mu\text{m}$. *Right:* Same spectra but normalized to the BH mass. All spectra for individual sources shown in the left panel, also including the galaxies in both the [B. L. Jones et al. \(2025\)](#) paper and our sample, are now plotted in red. Their BH masses come from single-epoch estimations based on $\text{H}\alpha$ or $\text{H}\beta$ lines. The BH masses for our stacks come from bolometric luminosities (Equation 1). In green, we show the ten sources in common between our sample and the sources for which the BH mass has been calculated by [V. Rusakov et al. \(2026\)](#) based on high spectral resolution data (mainly $R = 1000$) and a using single-epoch BH-mass estimator applied to the intrinsic narrow component, which yields up to an order of magnitude smaller SMBH masses compared to using the observed line width.

V-shaped continuum (Figure 13; black line). To allow for possible variations in the optical continuum shape among LRDs, we include a dust attenuation parameter (following a [D. Calzetti et al. 2000](#) law) that may reflect the presence of a developing torus, an external dust screen, or a higher gas column density relative to the fiducial LRD core. We note that indeed the most extreme of the $^x\text{LRDs}$, some individual examples are shown in Figure 13, are well represented by this approach when adding an extra opacity of $A^V \sim 1$ mag. Jointly with the LRD core, we consider a galaxy host with a composite stellar population.

Consistent with the inclusion of dust, we also model the associated mid-IR re-emission using a compact torus viewed at 45° – 60° , following [R. Siebenmorgen et al. \(2015\)](#). While rest-frame mid-IR wavelengths are only loosely constrained by the NIRSpec spectra, they are effectively probed by the available MIRI photometry (see Section 3.4 and Figure 6).

The stellar host component is modeled using SYNTHESIZER ([P. G. Pérez-González et al. 2003, 2008, 2024a](#)), following a similar approach to that adopted in [P. G. Pérez-González et al. \(2024a\)](#). We allow for two stellar populations: a very young component (< 10 Myr) to account for emission lines and WR features (see

Section 3.3), and an older population with a free age and independent dust attenuation, representing either an underlying stellar population or a deeply embedded burst. The star-formation history is parameterized as a delayed-exponential burst, with metallicities ranging from 2 to 20% solar, a [G. Chabrier \(2003\)](#) IMF with mass limits of 0.1 – $100 M_\odot$, and dust attenuation described by a [D. Calzetti et al. \(2000\)](#) law. We use [G. Bruzual & S. Charlot \(2003\)](#) models.

The combined host + LRD-core SED model depends on a total of 12 free parameters. Three parameters describe the LRD core: its normalization, attenuation, and the normalization of the mid-IR torus component. The remaining nine parameters describe the stellar populations, including the timescale, age, metallicity, and attenuation of each stellar component, as well as the relative burst strength, defined as the fraction of the total stellar mass associated with the youngest population. The main results of this SED-fitting analysis are compiled in Table 3.

5.2. The two-component modified blackbody plus galaxy-host SED model

An alternative SED modeling approach for LRDs has recently been presented by [A. de Graaff et al. \(2025b\)](#)

and [H. Umeda et al. \(2025\)](#), in which the LRD core is described using a parametric MBB model rather than an empirical template. We refer the reader to [Section 3.4](#) for caveats about the MBB model in the context of $T \sim 5000$ K gas. Nevertheless, given its relevance for comparison and interpretation, we apply this approach to our stacked spectra as well.

Specifically, we model the LRD core using the MBB formulation of [A. de Graaff et al. \(2025b\)](#), consisting of a Planck function modified by a power-law slope, β , relative to a pivot wavelength at $\lambda = 5500$ Å. This parameterization introduces three free parameters: the temperature T , the slope β , which primarily affects the Rayleigh–Jeans tail, and a normalization. Following [H. Umeda et al. \(2025\)](#), we additionally include a sharp drop at the Balmer limit, which cannot be reproduced by a pure blackbody. Rather than a Heaviside function, we adopt a sigmoid profile centered at the Balmer edge with a width of $0.05 \mu\text{m}$ to allow for a smoother transition.

For consistency with our default SED modeling, we combine the MBB LRD-core component with a stellar host contribution, resulting in a two-component model analogous to that described in the previous subsection. This differs from the single-component MBB approach adopted in [A. de Graaff et al. \(2025b\)](#). The impact of including an explicit host-galaxy component is discussed in the following sections.

5.3. BH and stellar masses and luminosities of LRDs

Under the assumption that the LRD core traces a black-hole-powered component, whether in the form of a BH* or a BHE, the best-fit SED models provide estimates of both stellar and black hole masses and luminosities. For the stellar component, the stellar mass M_{\star} is obtained directly from the population synthesis modeling, while the infrared luminosity associated with stars, L_{\star}^{IR} , is inferred from the fitted attenuation A_{\star}^{V} , assuming that the absorbed energy is re-emitted by dust in the infrared.

For the LRD core, the bolometric luminosity $L_{\text{BH}}^{\text{bol}}$ is obtained by integrating the core SED. The black hole mass M_{BH} is not a direct fit parameter, but is instead inferred from $L_{\text{BH}}^{\text{bol}}$, also including an Eddington ratio, λ_{Edd} , through the relation:

$$M_{\text{BH}}/M_{\odot} = 0.81 \times 10^5 \lambda_{\text{Edd}}^{-1} \left(\frac{L_{\text{BH}}^{\text{bol}}}{10^{43} \text{ erg s}^{-1}} \right), \quad (1)$$

As discussed in [Section 4.2](#), we adopt Eddington ratios of $\lambda_{\text{Edd}} = 0.6$ for all LRDs. We note that this method is similar to that presented in [H. Umeda et al. \(2025\)](#), but they obtain the bolometric emission with a constant

correction applied to optical luminosities, and we use SED fitting, resulting on different bolometric corrections for each subtype.

A different (but not completely independent) BH mass estimation is obtained by using the normalized $^{\times}$ LRD spectrum presented in [Figure 13](#) (right panel). The factor that should be applied to that spectrum to fit the SED of the different subtypes of LRDs, after correcting for attenuation A_{BH}^{V} , provides an estimation of M_{BH} .

5.4. Discrepancies between the emission line width and bolometric luminosity-based M_{BH} estimates

Black hole masses inferred from our bolometric-luminosity-based approach, assuming a gas-enshrouded SMBH and accretion disk, are systematically smaller than the median values obtained from single-epoch estimates based on emission-line widths and luminosities (e.g., [B. L. Jones et al. 2025](#)), as also noted by [H. Umeda et al. \(2025\)](#). This difference is illustrated in the right panel of [Figure 13](#), where the $^{\times}$ LRD stack is plotted in luminosity-density units normalized by the inferred black hole mass. Individual sources with black hole masses derived from H α line widths using classical single-epoch calibrations (e.g., [A. E. Reines et al. 2013](#)) are shown in red. We find that the mass-normalized LRD stacks differ from the individual single-epoch estimates by ~ 1 – 2 dex, with a scatter of ~ 1 dex among individual sources.

Additional insight is provided by the comparison with the high-SNR NIRSpect analysis of [V. Rusakov et al. \(2026\)](#), who derived black hole masses for a sample of 12 LRDs using $R = 1000$ – 2700 spectroscopy and a detailed H α profile decomposition that includes an intrinsic narrow component and line broadening due to electron scattering. In the right panel of [Figure 13](#), the ten sources in common between their sample and ours are shown in green, normalized by their black hole mass estimates. The SMBH-mass normalized LRD-core empirical template lies in between the spectra in [V. Rusakov et al. \(2026\)](#) and those for LRDs normalized by the single-epoch SMBH masses obtained by [B. L. Jones et al. \(2025\)](#). This might reflect uncertainties in [Equation 1](#), for example, linked to some non-negligible contribution to the LRD-core emission from processes not directly related to AGN accretion (e.g., a recent intense starburst). The latter would imply that our SMBH masses would be overestimated by a factor of 0.5 dex. As caveats to this statement, we can mention that additional uncertainties arise from our assumptions, such as the uniform $\lambda_{\text{Edd}} \sim 0.6$, the radiative efficiency and/or SED assumption (following [J. E. Greene et al. 2026](#)). Nevertheless, also the alternative premise about virial equilibrium and

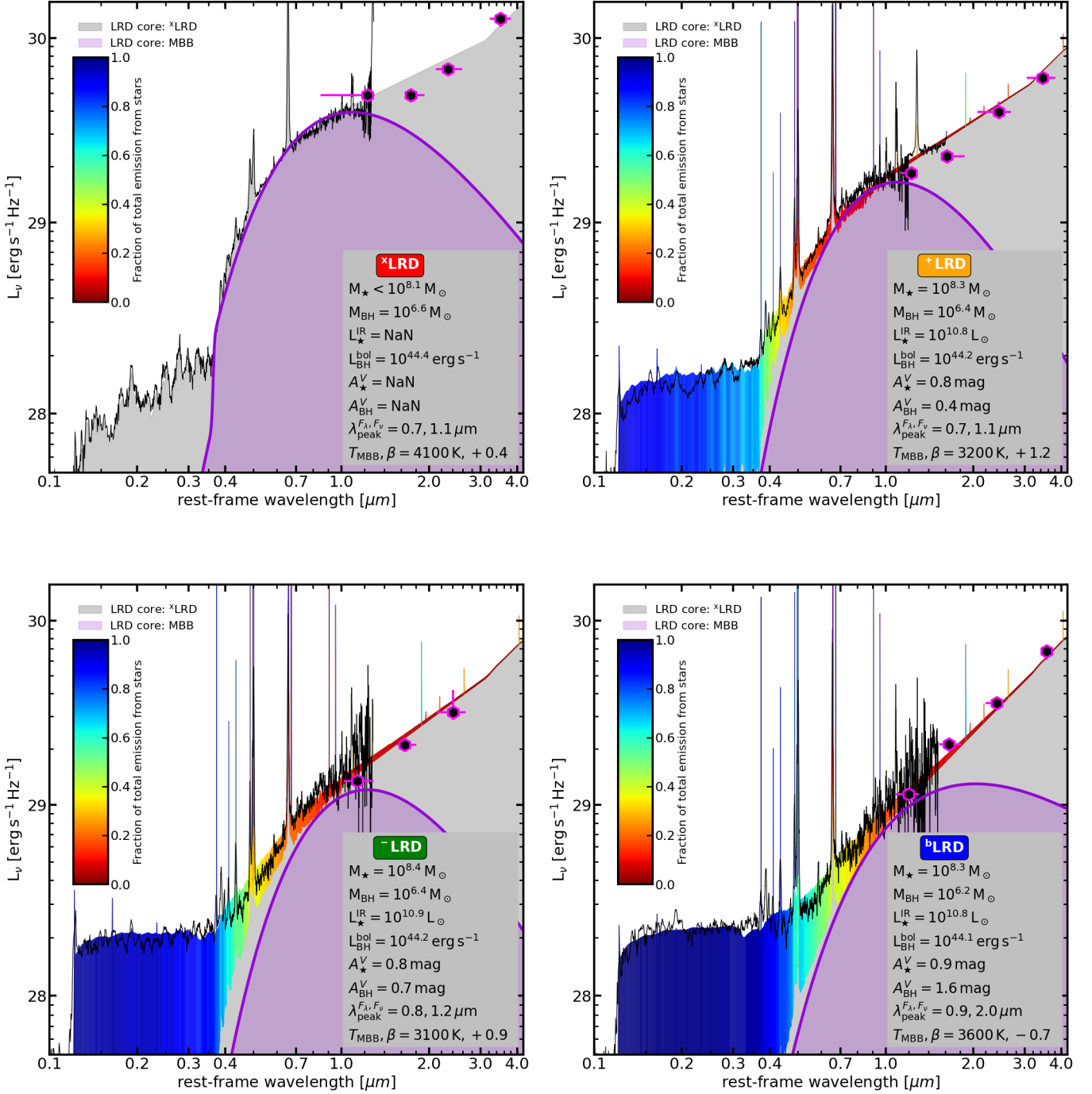


Figure 14. SED fitting results for the LRs subtypes. In all panels, we show in black the stacked spectrum and the MIRI stacks with black data points and errors in magenta. The shaded areas depict the LRD core component modelled with the two SED-fitting methods outlined in the text, i.e., using the ^xLRD stack as the LRD core (gray), or using an MBB (magenta). The rainbow-palette colored regions represent the contribution from stellar emission as a function of wavelength (as given in the scale on the left of each panel). We provide the main physical properties obtained with this SED fitting exercise, namely the stellar mass M_\star , the BH mass M_{BH} , the power emitted by the stars and absorbed by dust L_\star^{IR} , the bolometric luminosity of the AGN obtained by integrating the LRD core component $L_{\text{BH}}^{\text{bol}}$, and the A_\star^V attenuation applied to the BH and stellar components, A_{BH}^V and A_\star^V , respectively, the peak of the MBB emission, and its temperature and emissivity (β).

size-luminosity scalings underlying single-epoch calibrations (e.g., J. E. Greene & L. C. Ho 2005; A. E. Reines & M. Volonteri 2015) may not be warranted in LRDs.

5.5. Best-fit BH and stellar properties of the LRD subtypes

Figure 14 shows the results of the SED fitting for the stacked spectra of the individual subtypes. The full sample stack analysis provides similar results to those obtained for the ⁺LRD and ⁻LRD subtypes. We note that the ^xLRD subtype is adopted as our template “naked” LRD core and is therefore not fitted with an explicit stellar component. Integrating its SED yields a characteristic black hole mass of $M_{\text{BH}} \sim 10^{6.6 \pm 0.3} M_{\odot}$.

We examine trends in the best-fit properties from the reddest to the bluest LRD subtypes (top-left to bottom-right panels), spanning $L_{5100}/L_{2500} = 10.4, 3.8, 2.5,$ and 1.4 , corresponding to optical slopes (in f_{λ}) $\beta_{\text{OPT}} = 1.52, 0.53, 0.0,$ and -0.6 , respectively.

The color scale, which traces the fractional stellar contribution as a function of wavelength, shows that the primary driver of the declining L_{5100}/L_{2500} ratios and optical slopes is the increasing contribution of the host galaxy, strongest in the UV but extending into the optical. The host-to-core luminosity ratio at 5100 \AA increases sharply from $L_{\star}/L_{\text{core}} = 0.3$ to 0.6 and 2.0 from the ⁺LRD to the ^bLRD subtypes. For the ^xLRD, adopted as our “naked” core template, the ratio is set to zero by construction, as its UV emission is assumed to arise entirely from the BH or its immediate surroundings.

The overall SED shape of the LRD subtypes also evolves systematically with decreasing L_{5100}/L_{2500} . The UV continua become progressively bluer (flatter), with slopes $\beta_{\text{UV}} = -1.6, -1.8,$ and -2.0 , while the optical continua become more power law like compared to the intrinsically curved LRD-core template (black line in Figure 13). As noted in G. Barro et al. (2025), this behavior is driven primarily by the growing contribution of the host-galaxy continuum (see also W. Q. Sun et al. 2026), but also by increasing attenuation of the LRD core, with A_{BH}^{V} rising from 0.4 to 1.6 mag toward the bluest subtypes.

Additional support for enhanced dust attenuation comes from the steep MIRI fluxes extending the NIR-Spec SEDs, which follow a similar power-law trend and suggest the presence of dust re-emission (Section 3.4). In terms of intrinsic properties, the black hole mass exhibit a mild decrease toward bluer subtypes, with $M_{\text{BH}} \sim 10^{6.6} - 10^{6.2} M_{\odot}$ and $L^{\text{bolBH}} = 10^{44.4} - 10^{44.1} \text{ erg s}^{-1}$, a change consistent with the smaller optical luminosities for bluer LRDs. The stellar masses are quite constant

$M_{\star} \sim 10^{8.3} M_{\odot}$. The stellar attenuation is also very similar for all LRD subtypes, $A_{\star}^{\text{V}} \sim 0.8$ mag.

As a complement to our default host+LRD-core fits, Figure 13 presents two-component models combining a stellar host with an MBB core, allowing direct comparison with the approaches of A. de Graaff et al. (2025b) and H. Umeda et al. (2025). The MBB component closely resembles the ^xLRD template and shows a similar decline in L_{\star}/L_{MBB} at 5100 \AA toward bluer subtypes, consistent with host-galaxy growth driving the observed color diversity. However, as discussed in Section 3.4, the MBB models fail to reproduce the steepening of the rest-frame near-IR SED traced by the MIRI photometry, which suggests the presence of an additional dust re-emission component in all LRD subtypes, or a mix of emitting components with a variety of temperatures.

From the MBB fits we also estimate the wavelength of the SED peak in f_{λ} , which varies across the subtypes from $\lambda_{\text{peak}} = 0.7$ to $0.9 \mu\text{m}$ (corresponding to 1.1 to $2.0 \mu\text{m}$ in F_{ν}). This range is consistent with A. de Graaff et al. (2025b), who find $\lambda_{\text{peak}} \sim 0.60 - 0.80 \mu\text{m}$ and report a mild anti-correlation between λ_{peak} and Balmer-break strength. Agreeing with this trend, the LRD core, which has the highest L_{5100}/L_{2500} and strongest Balmer break among the subtypes, peaks just bluewards of $\lambda_{\text{peak}} \simeq 0.7 \mu\text{m}$, while bluer subtypes peak at progressively longer wavelengths.

5.6. The M_{BH}/M_{\star} relation for LRD subtypes

The stellar and BH masses are compared in Figure 15. As also obtained by H. Umeda et al. (2025), the BH-to-stellar mass ratio for LRDs are above the local relationship but only moderately. Typically BH masses are $0.8 - 3\%$ of the stellar values. This ratio is more similar to the values obtained for AGN which do not qualify as LRDs (e.g., R. Maiolino et al. 2024; B. L. Jones et al. 2025), and significantly smaller than the ratios obtained by combining the observed width of the broad lines with single-epoch BH mass estimations. Figure 15 also shows a comparison of masses if 50% of the bolometric emission of the ^xLRD spectrum, assumed to be the LRD core and identified with a BH surrounded by dense gas, had instead a stellar origin, linked to a massive young burst, consistent with the WR features tentatively identified in all LRD subtypes, including the most extreme ones. The open hexagons shows the results after applying this correction. BH-to-stellar mass ratios would decrease by a factor of $2 - 3$ compared to our fiducial estimations (filled hexagons).

We compare our masses to the aforementioned V. Rusakov et al. (2026), who use single-epoch estimations based on the *intrinsic* line widths. The BH masses of

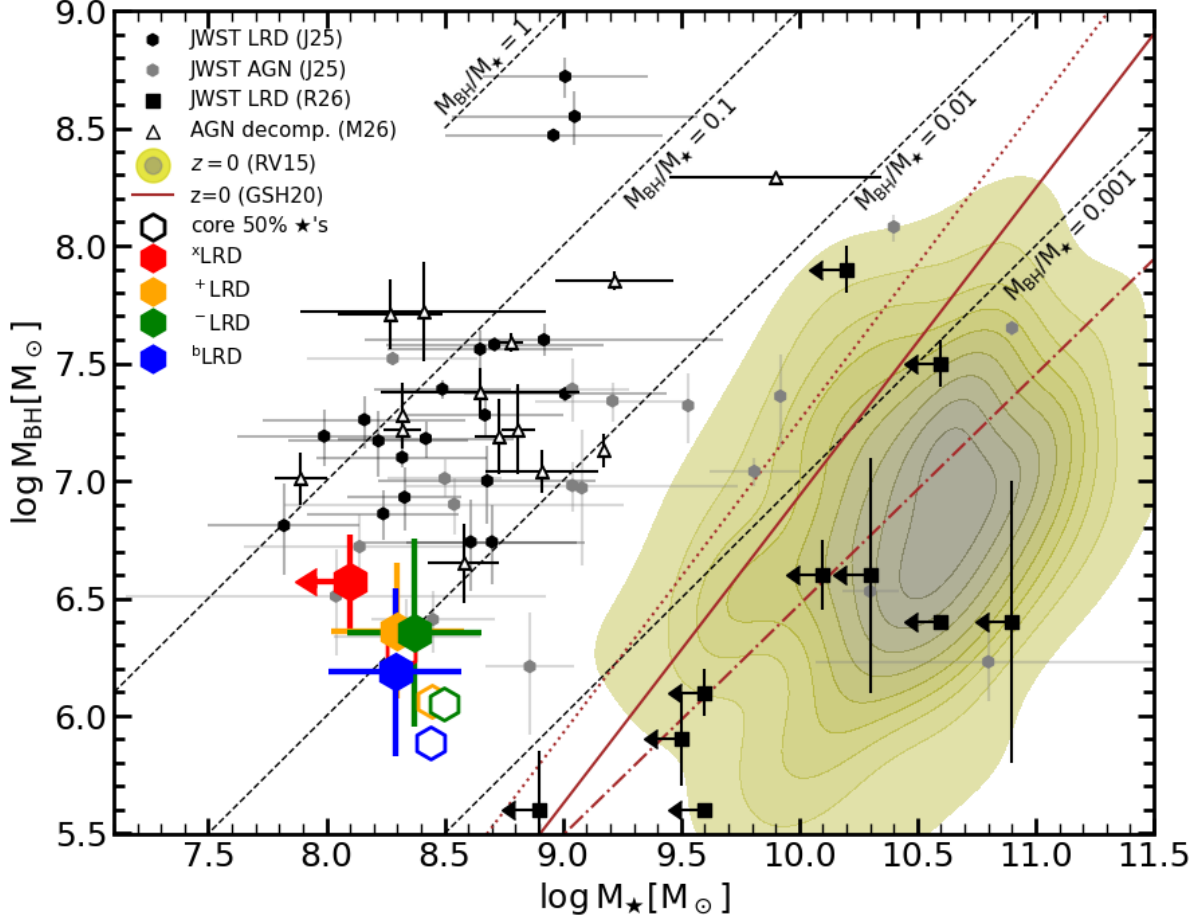


Figure 15. Comparison of the BH and stellar masses for our stacks are shown with filled hexagons in colors, each one representing a different LRD subtype. Open hexagons show results if we consider that 50% of the bolometric luminosity of the LRD core is linked to stellar emission (see text for details). Open hexagons show results for our stacks using a calibration based on BH masses from single-epoch Balmer line data. We also show with a shaded area the $z = 0$ AGN in [A. E. Reines & M. Volonteri \(2015\)](#), and with brown lines the relationships found by [J. E. Greene et al. \(2020\)](#) for all (continuous line), early-type (dotted), and late-type (dash-dot) $z = 0$ galaxies. The dots in black and gray depict the AGN in [B. L. Jones et al. \(2025\)](#), LRDs and non-LRDs, respectively. The squares are the AGN in [V. Rusakov et al. \(2026\)](#). The open triangles depict the AGN in [Z. Ma et al. \(2026\)](#). Dashed oblique lines mark specific BH-to-stellar mass ratios.

our stacks are slightly larger than the values obtained for their 12 individual LRDs (most of their sources would be classified as x LRDs and $^+$ LRDs). They report relatively large upper limits ($10^{9-11} M_{\odot}$) for the stellar masses for these sources, given that they fit the whole UV-to-near-infrared SED with stellar population, but they acknowledge the optical range might be dominated by an AGN, so most of their host masses can be regarded as upper limits.

6. DISCUSSION

We organize the discussion around eight different open questions, presenting our results in the context of our current knowledge about LRDs.

6.1. Are LRDs AGN?

Evidence for AGN activity in LRDs is primarily based on the detection of broad Balmer emission lines at high incidence across the population, most notably $H\alpha$ (e.g., [D. D. Kocevski et al. 2023](#); [J. E. Greene et al. 2024](#)), with reported FWHM values of $2000-4000 \text{ km s}^{-1}$ ([D. D. Kocevski et al. 2025](#); [G. Barro et al. 2025](#)). The stacked

spectra presented here similarly reveal broad $H\beta$, $H\alpha$, and $\text{He II } \lambda 4687$ emission, with $H\beta$ FWHM values of $3000\text{--}5000 \text{ km s}^{-1}$ that systematically decrease toward bluer LRD subtypes. Interestingly, for $H\alpha$ we find the opposite trend. i.e., bluer LRDs present larger values for the $H\alpha$ FWHM, although this could arise in part from [NII] contamination, which we cannot measure reliably with the spectral resolution of the prism. The $H\beta$ FWHM is 20% larger than that for $H\alpha$ for the reddest LRDs, but $\sim 60\%$ smaller for the two median and the bluest LRD subtypes.

In this paper, we explicitly test whether the observed diversity of LRD spectra (bright and faint emission lines and continuum) and optical-to-UV luminosity ratios can be reproduced by combining the core LRD template and varying host-galaxy contributions. We base our analysis on SED fitting using the SYNTHESIZER-AGN code, and on the assumption that the LRD core can be modeled with the \times LRD stack, which is weak in the UV. We find that stellar emission contributes non-negligibly to the continuum, and to some emission lines, including those of hydrogen. The stellar contribution is strongest in the UV continuum, exceeding 50% bluewards of $0.4 \mu\text{m}$ and 80% at $< 0.25 \mu\text{m}$ for all but the extremely red LRDs, which comprise $\sim 15\%$ of the population. This is consistent with the findings in Z. Ma et al. (2026), based on image decomposition (see also J. F. W. Baggen et al. 2026). At optical continuum wavelengths, stars contribute $\sim 40\%$ of the flux at $0.5 \mu\text{m}$ for the median LRD, reaching up to 60% for the bluest half of the population (Figure 14). Our analysis do not consider that different types of LRDs could still present some UV-bright AGN component, especially in the near-UV, where the emission from the accretion disk and the BLR peak (in F_ν), and in contrast with the far-UV.

Additional evidence for the presence of a luminous AGN is provided by FeII emission, which is ubiquitous in nearby AGN and QSOs (see Section 4.1 for references). Our stacked spectra show that optical FeII emission, in the $4100\text{--}5500 \text{ \AA}$ region as well as around 6500 \AA , is common in nearly all LRDs, consistent with previous detections in both the UV (I. Labbé et al. 2024) and the optical (A. Torralba et al. 2025; F. D’Eugenio et al. 2025; E. Lambrides et al. 2025; R. Tripodi et al. 2025b). In the UV, FeII emission is also detected in all but the bluest LRDs.

The location of LRDs in diagnostic diagrams based on emission-line ratios further supports the presence of AGN activity in most systems. The bulk of the population exhibits high $[\text{Ne III}]_{3870}/[\text{O II}]_{3728}$ ratios in the OHNO diagram (L. Trouille et al. 2011; G. R. Zeimann et al. 2015, see measurements in our stacks in Table 3),

consistent with ionization by an intrinsically hard source such as an AGN. The reddest LRDs, however, occupy a different region of this diagram, showing low $[\text{O III}]/H\beta$ ratios (Figure 12), which may reflect lower metallicities (see discussion in R. Maiolino et al. 2025b about near pristine gas in an AGN) or additional competing effects (e.g., linked to dense gas clouds). Further evidence for a powerful ionizing source is provided by the widespread detection of HeII and HeI lines discussed in this work. However, we find that UV lines such as CIII] and HeII $\lambda 1640$ point to a significant contribution, if not a dominant one, of stars in this spectral regime (consistent with measurements for sources identified as super star clusters or globular clusters in lensed galaxies, D. P. Stark et al. 2014; E. Vanzella et al. 2017). In contrast, MgII and FeII emission in the near-UV might indicate that this range, where the (F_ν) SED of QSOs typically peak (see Figure 3), could be more dominated by an AGN (in particular, the accretion disk and BLR).

6.2. Do LRDs host overmassive SMBHs?

SMBH masses in LRDs have been estimated using single-epoch spectroscopy based on relations calibrated on local AGN and QSOs, linking broad emission-line widths and optical luminosities (J. Kormendy & L. C. Ho 2013; A. E. Reines & M. Volonteri 2015). Such estimates have been reported for both individual sources (e.g., M. Killi et al. 2024; R. P. Naidu et al. 2025; A. de Graaff et al. 2025a; R. Tripodi et al. 2025a) and statistical samples (J. Matthee et al. 2024; J. E. Greene et al. 2024; B. L. Jones et al. 2025). Claims of overmassive black holes at high redshift, with SMBH-to-stellar mass ratios of order 0.1 or higher, are common in the literature (Y. Harikane et al. 2023b; F. Pacucci et al. 2023; R. Maiolino et al. 2024), with some LRDs inferred to reach even larger ratios (C.-H. Chen et al. 2025; B. L. Jones et al. 2025; I. Juodžbalis et al. 2025).

Using the bolometric luminosities derived from the SED modeling of the stacked NIRSpectra spectra from UV to near-IR wavelengths (Section 5.1), and the Eddington ratios inferred from FeII emission as discussed in Section 4.1, we estimate black hole masses following H. Umeda et al. (2025), as well as with a mass-normalized empirical template. The resulting bolometric luminosities, $L_{\text{BH}}^{\text{bol}} = 10^{44.1\text{--}44.4} \text{ erg s}^{-1}$, combined with typical Eddington ratios of $\lambda_{\text{Edd}} \sim 0.6$, imply black hole masses of $M_{\text{BH}} \sim 10^{6.0\text{--}6.5} M_\odot$. When compared to typical stellar masses of $M_\star \sim 10^{8.3} M_\odot$, these values correspond to SMBH-to-stellar mass ratios of $\sim 0.07\text{--}3\%$. This is at least an order of magnitude higher than observed in nearby AGN at similar stellar masses, and a factor

of $\sim 3\text{--}4$ above the highest ratios seen in massive local galaxies (J. E. Greene et al. 2020).

We remark several points about this comparison. First, we are comparing total stellar masses for galaxies with BH masses. If LRDs probe the early formation of bulges, we should compare with results in, e.g., J. Kormendy & L. C. Ho (2013), which obtain larger BH-to-stellar mass ratios (as high as 0.7%). These ratios would be more consistent with our measurements for LRDs, especially if the LRD core is not completely dominated by an AGN but has some stellar contribution (cf. open hexagons in Figure 15).

Indeed, our calculations assume that the LRD core emission is powered exclusively by a SMBH. However, we find spectral features consistent with massive WR stars even in the most luminous and reddest LRDs, which otherwise appear AGN-dominated in the UV. This would therefore introduce a non-negligible correction to the inferred bolometric luminosities and SMBH masses, which would be smaller. We would move, consequently, into the intermediate-mass regime ($M_{\text{BH}} < 10^6 M_{\odot}$; see J. E. Greene et al. 2020). On the opposite direction, an underestimation of the bolometric luminosities (i.e., if the intrinsic SED has considerable missing flux), that might depend on LRD subtype, would make BH masses larger than our estimations. The effect of Eddington ratios (assumed to be constant for all LRDs) is also a caveat to consider.

Considering all the evidence – and under the assumptions outlined above –, we conclude that the BHs in LRDs could be mildly overmassive. But within the uncertainties the BH-to-stellar mass ratios appear to be similar to those of other AGN at similar redshifts.

6.3. *How can we reconcile single-epoch BH mass estimates with measurements based on bolometric luminosities?*

Several explanations may account for the discrepancy between BH mass estimates obtained with measurements based on bolometric luminosities compared to single-epoch spectroscopy. The latter are based on empirical relations between optical (5100 \AA) continuum luminosity and $H\alpha$ or $H\beta$ line emission calibrated for local AGN and QSOs (J. E. Greene & L. C. Ho 2005; A. E. Reines et al. 2013). However, those relationships provide predicted line luminosities which are 0.2–0.6 dex lower than those observed in LRDs, even when the full line profiles are considered (i.e., not only the broad components) and considering all the emission in the optical is associated with the AGN (i.e., there is a negligible contribution from other emitting sources such as a nuclear starburst). If the bolometric-luminosity-based masses

are closer to the true values, this would imply that black holes in LRDs are unusually efficient at producing Balmer-line emission, or that a significant fraction of the observed SED is not directly associated with AGN accretion (Y.-X. Chen et al. 2026). Notably, this tension largely disappears for bluest LRD subtypes, for which black hole masses derived from emission-line widths and from bolometric luminosities agree to within ~ 0.2 dex. Jointly with the higher efficiency in producing line photons, part of the widening of emission lines might be associated with radiative transfer effects, rather than with virial motions (V. Rusakov et al. 2026; S.-J. Chang et al. 2026).

6.4. *Physical size scales of the central engine in LRDs*

Within the BH* or BHE framework, the radius of the emitting photosphere can be estimated from the Stefan–Boltzmann law (H. Umeda et al. 2025). Using the measurements for the different LRD subtypes presented here, together with the temperature–luminosity relation from A. de Graaff et al. (2025b), we infer photospheric radii of $\sim 7\text{--}13$ light-days (1200–2300 AU) from the reddest to the bluest LRDs, with a typical value of ~ 9 light days, consistent within a factor of ~ 2 with independent estimates (A. de Graaff et al. 2025b; Y. Pang et al. 2026).

An independent size estimate is obtained by applying the reverberation-mapping relation between optical luminosity and BLR size found in S. Kaspi et al. (2000), after correcting the optical luminosities using our SED fitting results. This yields BLR sizes of $\sim 37\text{--}7$ light days (6500–1200 AU) from the reddest to the bluest LRDs, with a typical value of ~ 16 light days.

6.5. *Are LRDs quasi-stars (aka black hole stars)?*

The red optical slopes of LRDs and the strong Balmer breaks observed in the $\sim 16\%$ of the LRD population with the highest L_{5100}/L_{2500} values ($^{\times}$ LRDs) can be reproduced by models invoking a very luminous source embedded in dense gas, as proposed in several studies (M. C. Begelman & J. Dexter 2026; R. P. Naidu et al. 2025; A. de Graaff et al. 2025a,b; H. Umeda et al. 2025; K. Inayoshi & L. C. Ho 2025). However, a number of observational features are difficult to reconcile with a stable black-hole star scenario.

To start, the high-EW emission lines such as $H\alpha$ cannot arise from within the blackbody, which by definition needs to be optically thick at all wavelengths. To power these lines, some models invoke intense star formation outside the BH* envelope, but this scenario makes it hard to reconcile the correlation between the continuum and line luminosity (A. de Graaff et al. 2025b).

In addition, several LRDs, all belonging to the $^{\times}$ LRD subtype, show clear evidence for self-absorption in the

brightest emission lines (e.g., J. Matthee et al. 2024; A. Torralba et al. 2025; F. D’Eugenio et al. 2026a, see also G. Barro et al. 2025). While not in direct contradiction with BH* models, these features point to the presence of warm, dense gas with complex kinematics, including signatures of outflowing (A. Torralba et al. 2025) or possibly inflowing material – sometimes both blueshifted and redshifted absorption are seen simultaneously in the same object (e.g., F. D’Eugenio et al. 2025). This complexity is indicative of a dynamically evolving rather than stable configuration (see section 6.7 for a discussion about timescales), clumpy gas, and/or a non-isotropic configuration.

The near-UV spectral region (i.e., bluewards of the Balmer break) shows emission lines that are characteristic of typical AGN, such as strong Mg II and Fe II emission, generally associated with the BLR (especially with regions near the accretion disk). This would suggest that there is not an isotropic envelope around the BH, but rather the covering factor is lower than one, due to holes/channels in the dense envelope or a more classical accretion disk (maybe with a thick inner region, see P. Marziani et al. 2018) and torus structure. Emission in the far-UV is also present in the most extreme, reddest LRDs, including Ly α emission and flux bluewards of it, which is difficult to reconcile with a pure BH*/BHE scenario, and is typically identified with star formation (again, even in the most extreme LRDs). This would mean that pure naked SMBHs do not exist or are very rare in LRDs.

Apart from the fact that our stacked spectra is consistent with a young stellar population dominating the UV emission in the majority of LRDs, we have found indications that massive stars may also contribute at optical wavelengths, where black-hole star models predict the embedded source should outshine stellar emission. These stellar contributions further challenge a purely black-hole star interpretation, and are discussed in more detail in the following subsection.

Other weaknesses of the BH*/BHE hypothesis have been presented in this paper. First, the larger H α width compared to H β for virtually all LRDs except for \times LRDs, except for the reddest, points to Raman scattering playing a role, something that would need some strong UV source (S.-J. Chang et al. 2026) near the dense gas emitting cloud (Y.-X. Chen et al. 2026). Second, a single BH* characterized by a MBB is not able to reproduce the emission in the near-IR, as probed by our MIRI stacks.

6.6. Do LRDs have dust?

Our SED modeling indicates an increasing contribution from young stellar populations to the UV emission of LRDs toward bluer subtypes. The fits favor very young ages (< 10 Myr) to reproduce part of the observed emission-line fluxes, consistent with the possible presence of Wolf–Rayet stars discussed in this work. To match the observed flat UV slopes, these models typically require moderate dust reddening ($A_{\star}^V \sim 1$ mag). Alternatively, some studies fit the UV continuum using constant star formation models with ages of ~ 10 – 20 Myr, which intrinsically produce flatter spectra and therefore require less dust ($A^V \sim 0.2$ mag; e.g., G. Barro et al. 2025).

In either case, the stellar populations dominating the UV are expected to contribute non-negligibly to the optical continuum, particularly around H β and even H α . This implies that the compact LRD core component must be redder than the fiducial template adopted for it, namely the stacked spectrum of \times LRDs. In our modeling, this effect is parameterized through dust attenuation, although it could also reflect increased opacity or a lower effective temperature of the source responsible for the red optical SED in progressively bluer subtypes.

As shown in Figure 14, the inferred reddening of the core component increases systematically across the LRD subtypes, from $A_{\text{BH}}^V = 0$ mag in \times LRDs, the subtype used as template (however, the \times LRDs might have some dust themselves) to $A_{\text{BH}}^V \sim 1.5$ mag in the bluest LRDs, in agreement with similar BH* modeling presented by G. Barro et al. (2025). If the core is instead modeled as a modified blackbody (MBB), the best-fit temperatures are around $T \sim 3000$ – 4000 K, but with varying β values to reproduce the SED behavior up to $\sim 1 \mu\text{m}$. Single-component MBB models are not able to reproduce the emission redwards of that value in any case. From SED modeling alone, it is difficult to determine whether attenuation or temperature primarily drives this evolution. However, there is a clear systematic change in SED shape, from strong curvature for the reddest LRDs to more power-law-like behavior in F_ν for blue ones (G. Barro et al. 2025), or equivalently a shift in the peak of the SED in F_λ , as reported by H. Umeda et al. (2025) and A. de Graaff et al. (2025b).

While SED fitting provides indirect constraints that depend on modeling assumptions, MIRI photometry offers a direct probe of dust re-emission, as discussed in Section 3.4. The stacked LRD SED shows a relatively flat rest-frame near-infrared continuum with a mild upturn beyond $\sim 2 \mu\text{m}$, inconsistent with pure stellar populations or $T \sim 4000$ K MBBs, both of which predict declining spectra and negative $[1 - 3 \mu\text{m}]$ col-

ors. Figures 13 and 14 show that this behavior persists across all LRD subtypes. Notably, the rest-frame near-infrared slope becomes progressively redder from x LRDs to b LRDs, with $[1 - 3 \mu\text{m}]$ color increasing from ~ 0.6 to ~ 1.6 mag. This trend supports increasing attenuation in the core component and suggests that changes in SED shape are more naturally driven by reddening rather than by decreasing temperature. It is also consistent with the findings of G. Barro et al. (2026), who reported redder $[1 - 3 \mu\text{m}]$ colors toward bluer UV-to-optical LRDs, and with those of I. Delvecchio et al. (2025), who demonstrate the need for hot (~ 800 K) dust to explain stacks of photometry for LRDs up to $3 \mu\text{m}$, with colder dust dominating at longer wavelengths (see also I. Juodžbalis et al. 2024 and M. Brazzini et al. 2026). We note that, under the hypothesis of increasing host contribution from x LRD to b LRD, a natural prediction is the increased presence of dust as we move to bluer systems.

Independent evidence for dust in LRDs comes from their Balmer decrements, which typically imply $A^V \gtrsim 0.5$ mag across all subtypes. For the reddest LRDs, however, interpreting these decrements purely in terms of dust is not straightforward, as their line emission may deviate from Case B recombination (G. P. Nikopoulos et al. 2025; F. D'Eugenio et al. 2025), for example, due to collisional excitation or resonant scattering in dense gas environments (S.-J. Chang et al. 2026; A. Torralba et al. 2025).

Finally, the presence of dust is consistent with the clear non-negligible metal enrichment observed in LRDs. All subtypes show strong oxygen, neon, and carbon emission lines, and many also exhibit features from iron, nitrogen, and sulfur, indicating chemically evolved gas even in these compact, high-redshift systems. However, the very low $[\text{OIII}]/\text{H}\beta$ ratios for the reddest LRDs might imply low metallicities, which would conflict with the presence of large amounts of dust.

6.7. What timescales govern the evolution of the LRD population?

There are five types of inferred physical properties for LRDs that can be used as a clock to estimate the timescales of the LRD phenomenon and even establish an evolutionary sequence within the different LRD subtypes defined in this paper. These are:

- The stellar mass, which, leaving aside yields and mass loss by winds, and disregarding the effect of interactions (not likely to affect the compact LRDs), should increase with time.

- The supermassive black hole mass, which should also increase with time.
- The presence of WR features, which point to a specific range of ages. And within those features, the evolution from nitrogen-rich WR to carbon-rich WR, which are typically claimed to follow a time sequence (P. A. Crowther 2007).
- Number density considerations, which should be linked to duty-cycle timescales.
- The redshift distribution of the different subtypes of LRDs.

Out of the five clocks above, the mass of the supermassive black hole is the most uncertain, since it depends on the accretion mode as discussed in Sections 6.2 and 6.3. With this in mind, Figure 15 shows no clear evolutionary sequence among the LRD sub-populations; all of them present very similar BH masses.

At least for the bulk of the LRD population, the stellar mass may be a more reliable measure of evolution. The stellar masses for all types except for the x LRDs are directly linked to the rest-frame UV emission. The relative contribution of stars and AGN to the continua in this spectral region is uncertain, but the line ratios ($\text{CIII}]$ over HeII) point to a non-negligible contribution from stars. In addition, the SEDs are always flat but present emission lines, so the stars should be young (if some flux in the emission lines is linked to stars). The only way to make young stars have a flat SED is dust. Our SED fitting calculations point to modest amounts of dust, with $A^V \sim 1$ mag. This dust attenuation would translate to mid-to-far infrared dust thermal emission consistent with a LIRG ($L_{\text{IR}}^{\star} \sim 10^{11} L_{\odot}$), which is consistent with upper limits imposed by ALMA data (see, e.g., C. Grupponi et al. 2020; C. C. Williams et al. 2024; C. M. Casey et al. 2024).

Our stellar mass estimation for x LRD is an upper limit, calculated by imposing that only the UV might have some contribution from stellar emission. In such case, x LRD would correspond to an early evolutionary phase, and then the evolution would then progress to bluer LRDs. The most worrisome caveat for this discussion about evolution based on stellar masses is the unknown contribution of stars to the rest-frame optical and near-IR, and to a lesser extent to the near-UV (with respect to the far-UV). If the optical/near-IR spectral regions are dominated by or present a significant contribution from highly embedded stars or supermassive stars (see Section 6.8), instead or jointly with an accreting SMBH, the stellar masses presented in Figure 15 should be considered as lower limits. However,

the amount of mass hidden there would not be large compared to the mass calculated from the UV emission, as we will discuss next, and consistent with clustering arguments, which give stellar masses around $10^8 M_{\odot}$, (J. Matthee et al. 2025; E. Pizzati et al. 2025).

Figures 5 and 11 show the spectral region around HeII λ 4687. Our fits of this region in terms of the WR blue bump has interesting implications. All subtypes of LRDs present a broad HeII component. That would mean that LRDs should have ages around 3-6 Myr. In general, all LRD subtypes present brighter nitrogen compared to carbon lines, which would imply a spectrum dominated by WN stars, ages around 3-5 Myr (P. A. Crowther 2007). The WR signatures are weakest in ^bLRDs, indicating a more evolved state, dominated by more evolved stars. The link between WR and LRD subtype would imply a strong synchronization between the SFH and the black-hole accretion activity and/or black-hole evolutionary stage.

Not much can be inferred from the redshift distribution of the different types of LRDs except for the bluest, whose redshift distribution is much broader and peaks at lower values, $z \sim 5$ compared to $z \sim 7$ for the rest of subtypes. The timescale for their appearance is then in the hundred Myr scale, rather than a few Myr.

A further piece of evidence about the timescales governing LRDs (and their subtypes) comes from their number densities. Leaving aside the ^bLRD, which can be identified with a more evolved stage, LRDs present a relatively flat redshift distribution covering the $4 < z < 9$ range, and a number density around $5 - 8 \times 10^{-5} \text{ Mpc}^{-3}$ (e.g., V. Kokorev et al. 2024; D. D. Kocevski et al. 2025). Considering a stellar mass of around $10^{8.3} M_{\odot}$, and comparing with the stellar mass function at the same redshifts (e.g., A. Weibel et al. 2024), which provides number densities around $3 - 6 \times 10^{-3} \text{ Mpc}^{-3}$, LRDs account for 1-3% of the general galaxy population. If all galaxies experience an LRD phase, this would mean that the timescale is around 20 Myr. For the ^xLRD, which are $\sim 16\%$ of the global population, the timescale would be $\sim 3\text{Myr}$, consistent with the WR discussion.

There are two more important points. After the WR phase, one could expect a high abundance of red supergiants. These stars could contribute significantly to the optical and near-infrared spectrum of LRDs. Indeed, the typical temperature of red supergiants is $\sim 4000 \text{ K}$, which is similar to the temperatures found with fits to modified black bodies by A. de Graaff et al. (2025b). The second point is that all subtypes of LRDs present significant iron emission. This would be consistent with an enrichment due to the most massive stars.

Drawing on all the information, all LRD subtypes except the bluest would be coeval, with mild indications of a possible evolutionary sequence from ^xLRD to ⁺LRDs and ⁻LRDs, and finally ^bLRDs. The separation between ^xLRD and ⁺LRDs and ⁻LRDs, however, seems to be dominated by BH mass (Figure 15) and gas density differences (Figure 12). The typical timescale is 20 Myr for the full LRD population, 3 Myr for the most extreme cases.

6.8. *Is there a credible alternative scenario to LRDs “being” AGN?*

As we mentioned in the Introduction, several alternative scenarios have been proposed to explain the observational characteristics of LRDs. The solution that dominates the literature is the identification of LRDs with a very unique phase of SMBH evolution with distinct AGN signatures. The most direct evidence for the LRD core being dominated by an AGN is the broad hydrogen lines which are identified with a BLR and also a narrow component identified with a NLR or, most probably, surrounding star formation. The other distinctive spectral feature of LRDs, the V-shape SED, has been explained with the presence of a dense gas envelope, possibly in the form of a black hole star, or quasi-star.

However, the two main observational characteristics (i.e., V-shape and broad emission lines) of LRDs can still have a stellar origin. In this paper, we present some evidence of the presence of massive hot stars in virtually all LRDs, including the most extreme, (^xLRDs), whose SED seems to be dominated by the LRD core at all wavelengths. This contrasts with bluer LRDs, which present significant emission in the UV with less prominent spectral features, more similar to star formation with relatively low dust content. If the blue bump in the ^xLRD stacked spectrum is identified with WR stars, if their luminosity is similar to those observed in nearby galaxies, and if the IMF is universal and follows a G. Chabrier (2003) law, a nearly $10^8 M_{\odot}$ burst would be embedded in ^xLRDs.

The problem is then how to explain the red spectral slope in the optical. Dust has been invoked in a number of papers (P. G. Pérez-González et al. 2024a; C. C. Williams et al. 2024), i.e., part of the recent starburst could be enshrouded by dust. Typical attenuations should exceed $A^V \sim 2 \text{ mag}$ and present a gray attenuation law or differential extinction (G. Barro et al. 2026). The presence of dust also implies that stellar masses should reach values around $10^{9.5} M_{\odot}$ or even higher which, jointly with the small sizes of LRDs, would imply very high densities. Although these densities could explain the broadening of the emission lines

(see J. F. W. Baggen et al. 2024), their values are similar to those observed for the regions with the highest mass concentrations in nearby galaxies (e.g., globular clusters). Those mass densities could be even exceeded if the stellar masses of LRDs are significantly higher than $10^{9.5} M_{\odot}$, something that was claimed in the first papers about LRDs (e.g., I. Labbé et al. 2023), although now the mass estimates are 1.0-1.5 dex lower, more consistent with dynamical constraints (e.g., I. Juodžbalis et al. 2024, 2025; F. D’Eugenio et al. 2026b). Another problem is the thermal emission of the dust associated with that intense star formation, which should be radiated in the mid-IR rather than the far-IR, i.e., the dust should be warmer than typical (U)LIRGs.

Although the presence of warm/hot dust is supported by the SEDs at wavelengths longer than $\sim 0.7 \mu\text{m}$ for some LRDs (in fact, the bluest, see next subsection), the \times LRD stack is bluer than the other stacks, which would point to a lower dust content. However, the Balmer decrement is quite high for \times LRDs, implying attenuations of $A^V \gtrsim 3$ mag, which is not consistent with the A^V values from SED fitting and is best reproduced with radiative transfer effects in dense gas clouds (S.-J. Chang et al. 2026).

If dust is not the main culprit for the red optical spectrum of LRDs, the alternative is some type of red star. Supermassive stars (SMS) have been claimed to produce the spectral signatures of LRDs (D. Nandal & A. Loeb 2025; L. Zwick et al. 2025), and in fact were claimed to be detectable by JWST prior to launch (M. Surace et al. 2018; F. Martins et al. 2020). The presence of supermassive stars in LRDs does not rule out their identification with SMBHs, since the seeds for the latter have been claimed to come from the remnants of these red supermassive stars (e.g. V. Bromm & A. Loeb 2003; J. A. Regan & M. G. Haehnelt 2009; T. E. Woods et al. 2019)

Taking the median LRDs ($+$ LRD and $-$ LRD subtypes) as example, our calculations point to the presence of a $\sim 10^{7.7} M_{\odot}$ starburst in the core of LRDs, which, being identified with the \times LRD subtype, also presents feature that can be linked to WR stars in a young starburst. A 4 Myr old burst with that mass would emit $L^{\text{bol}} = 10^{44.1} \text{ erg s}^{-1}$, which is similar to the median bolometric luminosity $L^{\text{bol}} = 10^{44.2} \text{ erg s}^{-1}$. The supermassive star should then be less luminous than $10^{10} L_{\odot}$. Using the evolution in the HR diagram from D. Nandal & A. Loeb (2025), the LRD emission would then need a moderate mass SMS, around $10^5 M_{\odot}$. For $10^5 M_{\odot}$, the temperature would be around 6000-7000 K, which is higher than the temperatures obtained from directly fitting the LRD spectra to modified black bodies (e.g., A. de Graaff et al. 2025b; H. Umeda et al. 2025), rang-

ing from 3000 to 6500 K (typically, ~ 5000 K). That range of temperatures would instead favor a number of $10^{3-4} M_{\odot}$ stars rather than a more massive single object. However, SMSs can be as cool 4000–5000 K (similar to supergiants), depending on their formation process (M. Gieles et al. 2018), so $10^{3-5} M_{\odot}$ could be consistent with an SED similar to a ~ 4000 K blackbody, more massive (and hot) in more extreme, reddest LRDs.

Several pieces of evidence could suggest the presence of a SMS. The \times LRDs present very low $[\text{OIII}]/\text{H}\beta$ ratios, which could indicate the infall (consistent with the $\text{H}\alpha$ profile) of low metallicity gas, favoring the formation of very massive stars (also direct collapse BHs, see F. Pacucci et al. 2026). The presence of prominent nitrogen lines and large N/O ratios have also been interpreted to favor the presence of massive stars while forming proto globular clusters in the early Universe (R. Marques-Chaves et al. 2024).

As the $[\text{OIII}]/\text{H}\beta$ ratio increases toward bluer LRDs, likely reflecting higher metallicity and chemical enrichment, the total bolometric luminosity decreases, even for similar LRD core masses. If the LRD core is a SMBH, its mass increases with time, naturally implying lower Eddington ratios. At the same time, enriched star formation becomes progressively more important, building stellar mass and dominating the UV emission, while conditions become less favorable for the formation of SMSs, leading to a decrease in the optical-to-UV luminosity ratio. Feedback from massive stars (including WR stars and possible SMSs), the SMBH, or both, together with gas exhaustion, would then quench further star formation. In parallel, dust production increases and the global attenuation rises. We summarize this evolutionary picture and its main physical ingredients in the schematic cartoon in Figure 16.

The evolutionary timescales also constrain the nature of any putative SMS component. Supermassive stars evolve rapidly. According to D. Nandal & A. Loeb (2025), the ages for which SMS would reach optical luminosity densities similar to the most extreme LRDs would be ~ 1 Myr for $10^4 M_{\odot}$ objects and even shorter for higher masses. For stars more massive than 300–500 M_{\odot} , the lifetime of stars becomes independent of mass. The typical main sequence timescale for stars up to 150 kM_{\odot} is 1.5 Myr (T. E. Woods et al. 2020). If SMSs accrete, their lifetime can be significantly longer (M. Gieles et al. 2018).

According to our analysis, the presence of WR features implies ages of $\lesssim 5$ –6 Myr, and number-density arguments suggest LRD phases lasting several Myr. This indicates that the LRD phenomenon cannot be instant-

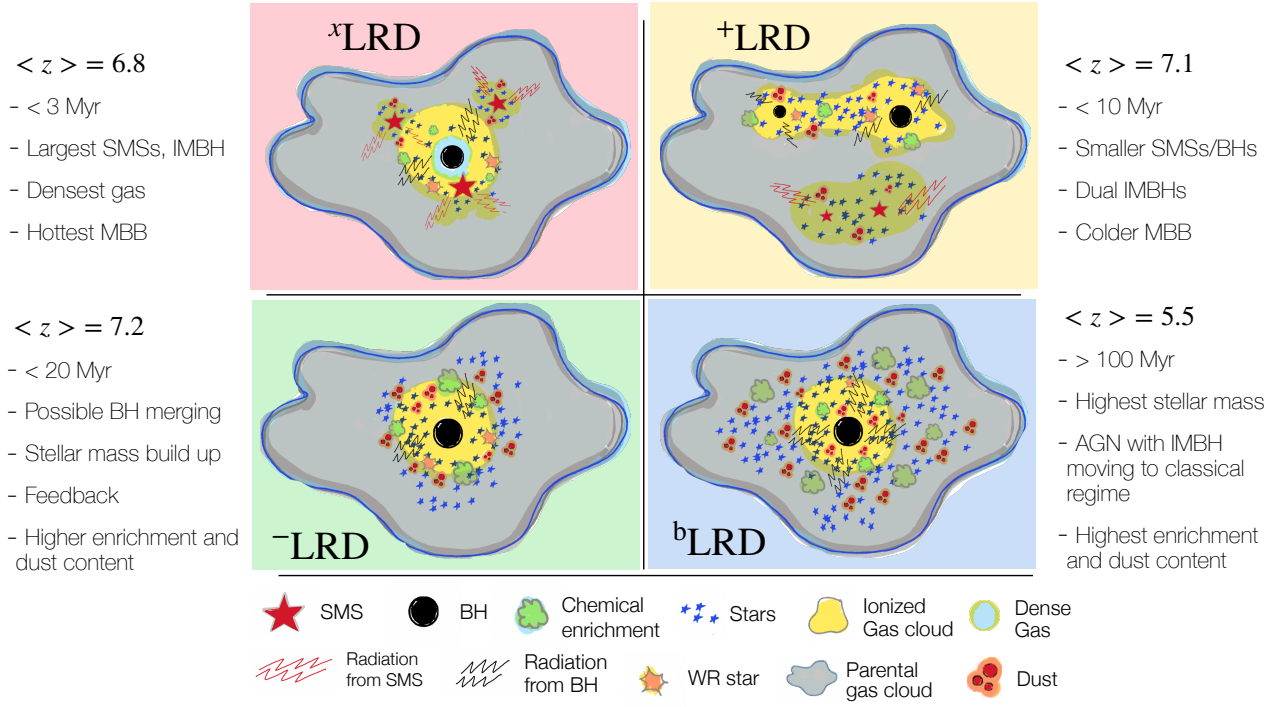


Figure 16. Cartoon of the different subtypes of LRDs and the emitting components discussed in the paper. Each panel represent a different subtype of LRD: x LRD with the background in red, $^+$ LRD in orange, $^-$ LRD in green, and b LRD in blue. Star formation complexes are shown with yellow circles, with regular stars in blue, massive stars (rapidly evolving into red supergiants) in red, WR stars in cyan, black holes in black. The whole compact structure is embedded in a dense gas environment (gray cloud), with some dust content which gets higher as we move to bluer LRDs. Some relevant points introduced in the Discussion section are given in text boxes by each cartoon.

neous and favors either moderately massive ($\lesssim 10^4 M_\odot$) SMSs or clusters hosting multiple such objects, consistent with the tendency of massive stars to form in binaries or multiple systems (e.g., H. Sana et al. 2012). We note that an intense and very compact star formation event extending along several Myr is consistent with the formation of globular clusters (see N. Bastian & C. Lardo 2018 and references therein; see also the connection between LRDs and globular clusters in J. Chisholm et al. 2026).

Recently, H. Yanagisawa et al. (2026) reported the discovery of two LRDs, separated by ≈ 70 pc and embedded in a star-forming galaxy with $M_{UV} \sim -19$ mag at $z \sim 7$, dubbed “The Red Eyes”. The galaxy is highly magnified ($\mu \sim 20$) by the gravitational lensing field of cluster PLCKG004.5-10.5, observed as part of the Cycle 4 JWST program VENUS (GO-6882; PIs: S. Fujimoto & D. Coe), and thanks to the increased resolution, they could establish that the LRD pair is not located in the center of the hosting galaxy but offset by roughly r_e , the effective radius. In other words, the LRDs are not “nuclear”. This might point to merging as playing a significant role in the early assembly of AGN. But

it might also provide evidence that LRD are not necessarily always “galactic nuclei”, and that they might form around black holes of suitable mass. This favors a scenario where LRDs are young galaxies observed early in their evolution with massive star formation involving WR phenomena, possibly SMSs, and rapid evolution to red supergiants (with cold atmospheres), quickly leading to the appearance of IMBHs which might then merge to form SMBHs. This scenario would be consistent with the formation of the most massive, earliest globular clusters, also taking into account the nitrogen enrichment mentioned above (see J. Chisholm et al. 2026).

7. SUMMARY AND CONCLUSIONS

We have compiled all publicly available NIR-Spec/prism spectroscopy ($R \sim 100$) and MIRI imaging for a sample of 249 LRDs distributed across six independent JWST fields, spanning redshifts $2.3 < z < 9.3$ (median and quartiles $z = 5.7_{4.0}^{7.4}$). Using high SNR stacked spectra covering the rest-frame wavelength range $0.1\text{--}4 \mu\text{m}$, we investigate the physical properties and nature of LRDs across their full observed diversity.

The sample encompasses the entire heterogeneity of LRD properties, from the reddest and most extreme systems to the bluest LRDs, whose characteristics approach those of classical AGN and QSOs while still retaining the defining observational features of the LRD class, namely, their compact morphology and distinctive V-shaped UV–optical SED. To capture this diversity quantitatively, we construct stacked spectra for four subtypes defined by their optical-to-UV luminosity density ratios, L_{5100}/L_{2500} : the most extreme ^xLRDs, the above-median ⁺LRDs, the below-median ⁻LRDs, and the bluest ^bLRDs.

The spectroscopic sample is broadly representative of the photometrically selected LRD population identified with NIRC*am*. Nevertheless, current follow-up programs show a modest bias toward lower redshifts, particularly for the reddest subtypes (median $z \sim 5.2$ in the NIRSpec sample compared to $z \sim 6.9$ in the corresponding NIRC*am*-selected sample).

The stacked spectra allow us to identify a set of robust observational characteristics of LRDs, summarized below.

- All stacked spectra of LRDs, independent of L_{5100}/L_{2500} , show spectral features consistent with a stellar origin.
- Stellar emission has a non-negligible contribution to the far-UV spectral region for the ^xLRDs (including extreme examples such as The Cliff and MoM-BH*-1) and rest of LRDs, as inferred from C III] equivalent widths and C III]/He II $\lambda 1640$ ratios.
- Optical spectral signatures associated with young massive stars in a Wolf–Rayet phase (e.g., He II $\lambda 4687$, carbon and especially nitrogen features) are detected in all LRD subtypes.
- An absorption feature near 4550 Å of uncertain origin (stellar atmospheres of cold stars -e.g., supergiants- or interstellar medium lines, most plausibly, Fe II absorption) is present in all LRD stacks.
- Clear AGN signatures are found in all LRDs. In addition to broad H α and H β components (the broad He II $\lambda 4687$ could also be linked to an AGN), we detect ubiquitous Fe II emission in both the optical (notably around ~ 5300 Å) and the UV (2200–3000 Å).
- Using Fe II emission jointly with Mg II and Balmer-line measurements, and assuming an AGN origin, we infer high accretion rates with $\lambda_{\text{Edd}} \sim 0.6 \pm 0.2$ for all LRD subtypes, except for the bluest systems, where reliable constraints are not possible.
- Compared to classical AGN, LRDs exhibit enhanced H α /optical and Fe II/optical luminosity ratios, indicating a higher efficiency in producing line emission relative to the optical continuum and suggesting a distinct structure and/or accretion mode relative to local AGN and QSOs.
- Emission-line diagnostics such as [O III]/H β , Balmer decrements (H α /H β , H β /H γ , H β /H δ), Paschen-to-Balmer ratios (H β /Pa γ), and Balmer break strength correlate systematically with L_{5100}/L_{2500} . Redder LRDs show lower [O III]/H β , stronger Balmer decrements, weaker Paschen-to-Balmer ratios, and larger Balmer breaks.
- The observed line and flux ratios likely arise from multiple physical effects. The Balmer and Paschen decrements are broadly consistent with radiative-transfer processes (e.g., collisional excitation and/or Raman scattering) in high-density gas enshrouding a SMBH or intense nuclear burst. In contrast, the systematic variation in [O III]/H β with L_{5100}/L_{2500} is also naturally explained by changes in the relative contribution of the host galaxy and the LRD core, with stronger narrow-line emission emerging toward bluer, more host-dominated systems.
- We detect differences in the width of H α and H β which depend on the LRD subtype. $\text{FWHM}(\text{H}\beta)/\text{FWHM}(\text{H}\alpha) = 1.2 \pm 0.1$ for ^xLRD (consistent with the average for local AGN and QSO), and $\text{FWHM}(\text{H}\beta)/\text{FWHM}(\text{H}\alpha) = 0.6 \pm 0.2$ for the rest of subtypes. This can be interpreted as Raman scattering, which would point to an intense radiation source present in all LRDs except the reddest.
- He I line ratios also point to significant effects linked to dense gas, with densities $n_e > 10^5 \text{ cm}^{-3}$, optically thick material, and temperatures around 5000-7000 K being necessary to explain the large measured values for the reddest LRDs.

We also perform SED fitting to the NIRSpec+MIRI stacks using a two-component model consisting of an LRD core and a stellar host. The LRD core is modeled empirically after the ^xLRD stacked spectrum, which includes intrinsic (non-stellar) UV emission, or a MBB

without it. In both approaches, the shape of the LRD core is allowed to vary through a free attenuation parameter to account for dust and/or gas obscuration. The core emission is interpreted as arising from an accreting SMBH and/or a compact nuclear starburst embedded in dense gas. The stellar host includes a very young (< 5 Myr) population to reproduce the emission-line features and is modeled with its own independent attenuation. This analysis provides the following main results:

- The observed diversity in continuum slopes is largely explained by variations in the host-to-core luminosity ratio. At $\lambda = 5100 \text{ \AA}$, $L_{\star}/L_{\text{core}}$ increases from 0 in the “naked” $^{\times}$ LRD template to 0.3, 0.6, and 2.0 toward progressively bluer subtypes, indicating a transition from BH-dominated to host-dominated optical emission. This trend is accompanied by a modest increase in attenuation of the BH core, with A_{BH}^V rising from 0.4 to 1.6 mag toward the bluest LRDs.
- The stellar masses are remarkably uniform across LRD subtypes, with $M_{\star} \sim 10^{8.3} M_{\odot}$ and a scatter of ~ 0.3 dex.
- Stellar emission contributes more than 50% of the flux at $\lambda < 0.4 \mu\text{m}$ for most subtypes (and more than 80% for the bluest LRDs), while remaining non-negligible ($\sim 20\%$) at optical and near-infrared wavelengths.
- The BH masses of all subtypes are $M_{\text{BH}} \sim 10^{6.0-6.5} M_{\odot}$. This means that the BH-to-stellar mass ratio is around 1%, with up to 2% for the reddest LRDs, and 0.7% for the bluest. These ratios are similar to the ones found for other AGN at high redshift. They are more than an order of magnitude larger than what is observed for galaxies of the same stellar mass at $z = 0$, and a factor of 3–4 larger than the ratios observed for the most massive galaxies in the local Universe.
- Smaller BH masses, within the intermediate-mass range ($M_{\text{BH}} < 10^6 M_{\odot}$), would be obtained if the LRD core emission is not completely dominated by nuclear activity.
- A modified blackbody with $T \sim 4000$ K reproduces the rest-frame optical SED reasonably well, but fails to account for the excess emission in the rest-frame 1–4 μm range probed by MIRI. This near-infrared excess becomes progressively stronger toward bluer LRDs, suggesting the presence of an additional hot (1000–1500 K) dust

component and/or emission from cooler dense gas clouds.

- The presence of dust increasing towards bluer LRDs would be consistent with a decreasing BH-to-stellar mass ratio, as the galaxy’s ability to create more dust grows. The dust would then need to be channeled to the LRD core, with mechanisms that depend how far away the stars are from the nucleus.
- Based on the SED-fitting analysis, as well as number-density arguments and the relative abundance of LRD subtypes, we estimate that the LRD phase lasts $\lesssim 20$ Myr, with the most extreme (reddest, $^{\times}$ LRD) phase lasting only ~ 3 Myr, consistent with age constraints from Wolf–Rayet features.

We discuss all spectro-photometric properties together, jointly with results in the literature, in terms of nuclear activity linked to super-massive (or even intermediate-mass) BHs, intense and compact starbursts with the possible presence of super-massive stars (with a mass around $10^5 M_{\odot}$), and a link to globular clusters (e.g., based on strong nitrogen emission). Further spectro-photometric analysis of large samples of LRDs will be needed to constrain their nature more securely, taking into account their heterogeneity.

ACKNOWLEDGMENTS

We thank Roberto Maiolino and Kimihiko Nakajima for useful comments on the manuscript. We want to thank the PIs and co-Is of all the programs listed in Table 1, and acknowledge funding linked to some of those programs for many of the co-authors of the paper. PGP-G acknowledges support from grant PID2022-139567NB-I00 funded by Spanish Ministerio de Ciencia, Innovación y Universidades MCIU/AEI/10.13039/501100011033, FEDER *Una manera de hacer Europa*. S.C. and G.V. acknowledge support by European Union’s HE ERC Starting Grant No. 101040227 - WINGS. F.D. and X.J. acknowledge support by the Science and Technology Facilities Council (STFC), by the ERC through Advanced Grant 695671 “QUENCH”, and by the UKRI Frontier Research grant RISEandFALL. S.A. and B.R.P. acknowledge support from the research project PID2021-127718NB-I00 funded by the Spanish Ministry of Science and Innovation/State Agency of Research (MICIN/AEI/10.13039/501100011033). A.J.B. and J.C. acknowledge funding from the “FirstGalaxies” Advanced Grant from the European Research Council (ERC) under the European Union’s Horizon 2020

research and innovation programme (Grant agreement No. 789056). E.C.L. acknowledges support of an STFC Webb Fellowship (ST/W001438/1). D.J.E. is supported as a Simons Investigator and by JWST/NIRCam contract to the University of Arizona, NAS5-02105. Support for program #3215 was provided by NASA through a grant from the Space Telescope Science Institute, which is operated by the Association of Universities for Research in Astronomy, Inc., under NASA contract NAS 5-03127. J.S. acknowledges support by the Science and Technology Facilities Council (STFC) and ERC Advanced Grant 695671 “QUENCH”. The research of C.C.W. is supported by NOIRLab, which is managed by the Association of Universities for Research in Astronomy (AURA) under a cooperative agreement with the National Science Foundation. C.T.D. acknowledges support from JWST program number GO-6368, provided through a grant from the STScI under NASA contract NAS5-03127. The work of GHR was supported in part by grant 80NSSC18K0555, from NASA Goddard Space Flight Center to the University of Arizona. HÜ acknowledges funding by the European Union (ERC APEX, 101164796). Views and opinions expressed are however those of the authors only and do not necessarily reflect those of the European Union or the European Research Council Executive Agency. Neither the European Union nor the granting authority can be held responsible for them. JW gratefully acknowledges support from the

Cosmic Dawn Center through the DAWN Fellowship. The Cosmic Dawn Center (DAWN) is funded by the Danish National Research Foundation under grant No. 140. C.N.A.W. and Y.Z. acknowledge support from the JWST/NIRCam contract to the University of Arizona NAS5-02105. ST acknowledges support by the Royal Society Research Grant G125142. JSD and DJM acknowledge the support of the Royal Society through the award of a Royal Society University Research Professorship to JSD. B.R.P acknowledges support from grant PID2024-158856NA-I00 funded by Spanish Ministerio de Ciencia e Innovación MCIN/AEI/10.13039/501100011033 and by “ERDF A way of making Europ”. This work is based on observations made with the NASA/ESA/CSA James Webb Space Telescope. The data were obtained from the Mikulski Archive for Space Telescopes at the Space Telescope Science Institute, which is operated by the Association of Universities for Research in Astronomy, Inc., under NASA contract NAS5-03127 for JWST.

Facilities: JWST (NIRCam), JWST (MIRI), HST (ACS), HST (WFC3). All the JWST data used in this paper can be found in MAST: [10.17909/jmxxm-1695](https://mast.stsci.edu/portal/#doc/obs/10.17909/jmxxm-1695) and [10.17909/8tdj-8n28](https://mast.stsci.edu/portal/#doc/obs/10.17909/8tdj-8n28).

Software: astropy (Astropy Collaboration et al. 2013, 2018), Cloudy (G. J. Ferland et al. 2013), PROSPECTOR (J. Leja et al. 2017, 2019; B. D. Johnson et al. 2021), SYNTHESIZER (P. G. Pérez-González et al. 2003, 2008).

REFERENCES

- Adamo, A., Atek, H., Bagley, M. B., et al. 2025, *Nature Astronomy*, 9, 1134, doi: [10.1038/s41550-025-02624-5](https://doi.org/10.1038/s41550-025-02624-5)
- Akins, H. B., Casey, C. M., Lambrides, E., et al. 2025a, *ApJ*, 991, 37, doi: [10.3847/1538-4357/ade984](https://doi.org/10.3847/1538-4357/ade984)
- Akins, H. B., Casey, C. M., Berg, D. A., et al. 2025b, *ApJL*, 980, L29, doi: [10.3847/2041-8213/adab76](https://doi.org/10.3847/2041-8213/adab76)
- Arevalo-Gonzalez, F., Tripodi, R., Llerena, M., et al. 2025, arXiv e-prints, arXiv:2512.16365, doi: [10.48550/arXiv.2512.16365](https://doi.org/10.48550/arXiv.2512.16365)
- Arrabal Haro, P., Dickinson, M., Finkelstein, S. L., et al. 2023a, *Nature*, 622, 707, doi: [10.1038/s41586-023-06521-7](https://doi.org/10.1038/s41586-023-06521-7)
- Arrabal Haro, P., Dickinson, M., Finkelstein, S. L., et al. 2023b, *ApJL*, 951, L22, doi: [10.3847/2041-8213/acdd54](https://doi.org/10.3847/2041-8213/acdd54)
- Astropy Collaboration, Robitaille, T. P., Tollerud, E. J., et al. 2013, *A&A*, 558, A33, doi: [10.1051/0004-6361/201322068](https://doi.org/10.1051/0004-6361/201322068)
- Astropy Collaboration, Price-Whelan, A. M., Sipőcz, B. M., et al. 2018, *AJ*, 156, 123, doi: [10.3847/1538-3881/aabc4f](https://doi.org/10.3847/1538-3881/aabc4f)
- Backhaus, B. E., Trump, J. R., Pirzkal, N., et al. 2024, *ApJ*, 962, 195, doi: [10.3847/1538-4357/ad1520](https://doi.org/10.3847/1538-4357/ad1520)
- Baggen, J. F. W., Scoggins, M. T., van Dokkum, P., et al. 2026, arXiv e-prints, arXiv:2602.02702, doi: [10.48550/arXiv.2602.02702](https://doi.org/10.48550/arXiv.2602.02702)
- Baggen, J. F. W., van Dokkum, P., Brammer, G., et al. 2024, *ApJL*, 977, L13, doi: [10.3847/2041-8213/ad90b8](https://doi.org/10.3847/2041-8213/ad90b8)
- Barro, G., Pérez-González, P. G., Kocevski, D. D., et al. 2024, *ApJ*, 963, 128, doi: [10.3847/1538-4357/ad167e](https://doi.org/10.3847/1538-4357/ad167e)
- Barro, G., Perez-Gonzalez, P. G., Kocevski, D., et al. 2025, arXiv e-prints, arXiv:2512.15853, doi: [10.48550/arXiv.2512.15853](https://doi.org/10.48550/arXiv.2512.15853)
- Barro, G., Pérez-González, P. G., Kocevski, D. D., et al. 2026, *ApJ*, 997, 48, doi: [10.3847/1538-4357/ae0704](https://doi.org/10.3847/1538-4357/ae0704)
- Bastian, N., & Lardo, C. 2018, *ARA&A*, 56, 83, doi: [10.1146/annurev-astro-081817-051839](https://doi.org/10.1146/annurev-astro-081817-051839)
- Bate, M. R. 2025, *MNRAS*, 537, 752, doi: [10.1093/mnras/staf059](https://doi.org/10.1093/mnras/staf059)

Table 1. Summary of spectroscopic and photometric observations used in this paper.

Field	Number of spectra	Number of photometric LRDs		NIRSpec PIDs		MIRI PIDs	
GDS	29	82	1180, 1210, 1212, 1286, 1287, 2198, 5997, 6541, 8060	1180, 1207, 1283, 2516, 3954, 4498, 5279, 5407, 6511			
GDN	31	144	1181, 8018	1181, 1264, 2926, 4530, 4586, 4762, 5407			
UDS	84	318	1215, 2565, 4233, 5224, 6368	1657, 1837, 7814			
COSMOS	36	164	2565, 5224, 6368, 6585	1284, 1727, 1762, 1837, 2417, 2775, 3954, 5893, 6595			
EGS	52	144	1345, 2750, 4106, 4233, 6368	1345, 1448, 3794, 4586			
A2744	17	43	2561, 3073	4530, 6743			

NOTE.—Table with information about the data used in the paper, including program IDs (PIDs) for NIRSpec and MIRI observations.

Table 2. Statistics of observational imaging properties of photometric and spectroscopic samples of LRDs.

Sample (N_{gal})	F444W	F277W-F444W	F115W-F200W	F200W-F444W	F444W-F770W	F770W-F1800W
Photometric NIRCam (NC) sample (849)	25.9 ^{26.6} _{25.0}	1.2 ^{1.6} _{1.0}	0.3 ^{0.6} _{0.0}	1.7 ^{2.2} _{1.3}	0.3 ^{0.7} _{0.1}	1.6 ^{2.3} _{0.6} (301)
Spectroscopic NIRSpec (NS) sample: NS (249)	25.9 ^{26.5} _{25.0}	1.2 ^{1.6} _{1.0}	0.3 ^{0.7} _{0.0}	1.7 ^{2.3} _{1.4}	0.3 ^{0.7} _{0.0}	1.2 ^{2.0} _{0.5} (84)
NC ^x LRD, $L_{\text{opt}}/L_{\text{UV}} > 6.3$ (137)	25.3 ^{26.0} _{24.5}	1.7 ^{2.1} _{1.2}	0.4 ^{0.8} _{0.1}	2.7 ^{3.1} _{2.5}	0.3 ^{0.7} _{0.1}	1.0 ^{1.9} _{1.9} (60)
NC ⁺ LRD, $3.1 < L_{\text{opt}}/L_{\text{UV}} < 6.3$ (290)	25.8 ^{26.5} _{26.0}	1.4 ^{1.7} _{1.3}	0.3 ^{0.8} _{0.0}	2.0 ^{2.2} _{1.8}	0.4 ^{0.0} _{0.0} (148)	1.1 ^{0.5} _{0.0} (80)
NC ⁻ LRD, $1.8 < L_{\text{opt}}/L_{\text{UV}} < 3.1$ (288)	26.3 ^{25.4} _{26.0}	1.1 ^{1.3} _{1.0}	0.2 ^{0.0} _{0.0}	1.4 ^{1.2} _{1.6}	0.3 ^{0.2} _{0.2} (159)	1.7 ^{2.4} _{2.0} (95)
NC ^b LRD, $L_{\text{opt}}/L_{\text{UV}} < 1.8$ (134)	26.1 ^{27.0} _{24.8}	1.1 ^{1.4} _{1.0}	0.3 ^{0.5} _{0.0}	1.0 ^{1.5} _{0.7}	0.4 ^{1.1} _{0.1} (95)	2.1 ^{2.6} _{1.6} (66)
NS ^x LRD, $L_{\text{opt}}/L_{\text{UV}} > 6.3$ (29)	24.5 ^{25.2} _{23.6}	1.6 ^{2.0} _{1.7}	0.7 ^{1.3} _{0.4}	2.5 ^{3.1} _{2.3}	0.1 ^{0.6} _{0.0} (21)	0.6 ^{1.1} _{0.0} (11)
NS ⁺ LRD, $3.1 < L_{\text{opt}}/L_{\text{UV}} < 6.3$ (74)	25.6 ^{24.9} _{24.9}	1.3 ^{1.0} _{1.0}	0.3 ^{0.1} _{0.1}	2.1 ^{1.6} _{1.6}	0.4 ^{0.1} _{0.1} (46)	0.9 ^{0.4} _{0.4} (26)
NS ⁻ LRD, $1.8 < L_{\text{opt}}/L_{\text{UV}} < 3.1$ (77)	26.3 ^{25.4} _{26.0}	1.2 ^{1.4} _{1.0}	0.2 ^{0.4} _{0.1}	1.6 ^{2.0} _{1.3}	0.1 ^{0.6} _{0.2} (37)	0.6 ^{2.4} _{0.3} (23)
NS ^b LRD, $L_{\text{opt}}/L_{\text{UV}} < 1.8$ (69)	26.1 ^{26.6} _{25.4}	1.1 ^{1.3} _{1.0}	0.2 ^{0.7} _{0.1}	1.4 ^{1.7} _{1.2}	0.4 ^{0.8} _{0.1} (39)	2.0 ^{2.3} _{1.5} (24)

NOTE—Table with statistical observational properties of the sample of LRDs in this paper. We provide medians and quartiles for the F444W magnitude and several colors involving NIRCam and MIRI bands, for the whole sample of LRDs selected in the six fields considered in this paper, the subsample observed by NIRSpec, as well as for several subtypes of LRDs (see main text for definitions) constructed with cuts in optical-to-UV luminosity ratio.

Table 3. Spectroscopic properties of LRDs

Property	^x LRD	⁺ LRD	⁻ LRD	^b LRD
Spec-z NS	5.2 ^{7.1} _{3.8}	5.7 ^{7.4} _{4.0}	6.2 ^{7.3} _{4.2}	5.9 ^{7.9} _{4.0}
Photo-z NC	6.9 ^{7.8} _{5.0}	7.1 ^{8.1} _{5.0}	7.1 ^{8.0} _{4.7}	5.2 ^{7.6} _{1.5}
log L ₅₁₀₀ NS [erg s ⁻¹ Hz ⁻¹]	29.2 ^{29.5} _{28.9}	28.8 ^{29.2} _{28.5}	28.7 ^{29.1} _{28.3}	28.5 ^{28.9} _{28.1}
log L ₅₁₀₀ NC [erg s ⁻¹ Hz ⁻¹]	29.2 ^{29.6} _{28.8}	29.0 ^{29.4} _{28.6}	28.9 ^{29.2} _{28.5}	28.4 ^{29.0} _{27.6}
L ₅₁₀₀ /L ₂₅₀₀ NS	10.4 ^{18.6} _{7.8}	3.8 ^{5.1} _{3.3}	2.5 ^{3.0} _{2.0}	1.4 ^{1.6} _{0.7}
L ₅₁₀₀ /L ₂₅₀₀ NC	9.2 ^{14.6} _{7.0}	4.0 ^{5.3} _{3.4}	2.4 ^{2.9} _{2.0}	1.2 ^{1.7} _{0.7}
EW ₀ (C III]λ1908) [Å]	18.9 ± 5.2	13.3 ± 4.6	20.3 ± 3.9	11.6 ± 4.1
C III]λ1908/He IIλ1640	> 5.1	1.5 ± 0.6	3.2 ± 1.7	2.9 ± 0.9
log M _T ^{WR} [M _⊙]	8.0 ± 0.3	7.7 ± 0.2	7.8 ± 0.2	7.4 ± 0.2
He Iλ7067/He Iλ5877	1.7 ± 0.3	1.4 ± 0.2	1.2 ± 0.2	1.0 ± 0.1
He Iλ10833/He Iλ5877	10.0 ± 1.5	12.0 ± 1.1	7.1 ± 1.0	7.0 ± 0.7
[O III]λ5008/Hβ	1.1 ± 0.1	3.2 ± 0.1	4.4 ± 0.3	4.9 ± 0.5
Hα/Hβ	10.1 ± 0.8	8.0 ± 0.3	6.4 ± 0.3	5.5 ± 0.5
Hβ/Hγ	8.5 ± 2.8	4.4 ± 1.0	3.4 ± 0.9	3.0 ± 1.0
Hβ/Hδ	13.4 ± 3.7	8.3 ± 1.3	7.1 ± 1.3	5.2 ± 1.3
Hβ/Paγ	2.3 ± 0.9	2.6 ± 0.5	3.6 ± 2.3	3.0 ± 1.0
Balmer break	3.3 ± 0.7	1.4 ± 0.3	1.2 ± 0.2	1.1 ± 0.2
[O III]λ4363/Hγ	1.1 ± 0.0	1.0 ± 0.5	0.6 ± 0.0	1.0 ± 0.5
[O III]λ5008/[O II]λ3728	14.8 ± 4.6	21.8 ± 6.6	23.6 ± 4.7	17.5 ± 5.4
[Ne III]λ3870/Hγ	1.9 ± 0.6	1.1 ± 0.3	2.3 ± 0.5	1.5 ± 0.5
M _★ [M _⊙]	< 8.1	8.3 ± 0.3	8.4 ± 0.3	8.3 ± 0.3
M _{BH} [M _⊙]	6.6 ± 0.3	6.4 ± 0.3	6.4 ± 0.4	6.2 ± 0.4
log L _★ ^{IR} [L _⊙]	–	10.8 ± 0.2	10.9 ± 0.2	10.8 ± 0.2
log L _{BH} ^{bol} [erg s ⁻¹]	44.4 ± 0.2	44.2 ± 0.3	44.2 ± 0.3	44.1 ± 0.3
A _★ ^V [mag]	–	0.8 ± 0.2	0.8 ± 0.2	0.9 ± 0.2
A _{BH} ^V [mag]	–	0.4 ± 0.1	0.7 ± 0.2	1.6 ± 0.6
λ _{peak} ^{Fν} [μm]	1.1 ± 0.1	1.1 ± 0.1	0.8 ± 0.1	0.9 ± 0.1
λ _{peak} ^{Fλ} [μm]	0.7 ± 0.1	0.7 ± 0.1	1.2 ± 0.1	2.0 ± 0.1
T _{MBB} [K]	4100 ± 100	3200 ± 100	3100 ± 100	3600 ± 200
β _{MBB}	+0.4 ± 0.1	+1.2 ± 0.1	+0.9 ± 0.2	-0.7 ± 0.3

NOTE—Table with spectroscopic information and physical properties of the sample of LRDs in this paper. The first set of properties provide statistical information (median and scatter given as 16%–84% quantiles) about the spectroscopic (NS) and photometric (NC) samples. The second set gives line ratios and equivalent widths measured (with their uncertainties) in the stacks (only for spectroscopic samples). The third set provides physical properties inferred from analysis of the stacks (only for spectroscopic samples).

Begelman, M. C., & Dexter, J. 2026, ApJ, 996, 48,

doi: [10.3847/1538-4357/ae274a](https://doi.org/10.3847/1538-4357/ae274a)

Berg, D. A., Naidu, R. P., Chisholm, J., et al. 2025, arXiv

e-prints, arXiv:2511.13591,

doi: [10.48550/arXiv.2511.13591](https://doi.org/10.48550/arXiv.2511.13591)

Berg, D. A., Sanders, R. L., Shapley, A. E., et al. 2026,

ApJ, 996, 68, doi: [10.3847/1538-4357/ae18db](https://doi.org/10.3847/1538-4357/ae18db)

Bezanson, R., Labbe, I., Whitaker, K. E., et al. 2024, ApJ,

974, 92, doi: [10.3847/1538-4357/ad66cf](https://doi.org/10.3847/1538-4357/ad66cf)

Boroson, T. A., & Green, R. F. 1992, ApJS, 80, 109,

doi: [10.1086/191661](https://doi.org/10.1086/191661)

Boyet, K., Bunker, A. J., Curtis-Lake, E., et al. 2024,

MNRAS, 535, 1796, doi: [10.1093/mnras/stae2430](https://doi.org/10.1093/mnras/stae2430)

Boylan-Kolchin, M. 2023, Nature Astronomy, 7, 731,

doi: [10.1038/s41550-023-01937-7](https://doi.org/10.1038/s41550-023-01937-7)

Brazzini, M., D’Eugenio, F., Maiolino, R., et al. 2026,

arXiv e-prints, arXiv:2601.22214,

doi: [10.48550/arXiv.2601.22214](https://doi.org/10.48550/arXiv.2601.22214)

Brinchmann, J., Kunth, D., & Durret, F. 2008, A&A, 485,

657, doi: [10.1051/0004-6361:200809783](https://doi.org/10.1051/0004-6361:200809783)

Bromm, V., & Loeb, A. 2003, ApJ, 596, 34,

doi: [10.1086/377529](https://doi.org/10.1086/377529)

Brooks, M., Trump, J. R., Simons, R. C., et al. 2025, arXiv

e-prints, arXiv:2511.19609,

doi: [10.48550/arXiv.2511.19609](https://doi.org/10.48550/arXiv.2511.19609)

Bruhweiler, F., & Verner, E. 2008, ApJ, 675, 83,

doi: [10.1086/525557](https://doi.org/10.1086/525557)

Bruhweiler, F. C., Miskey, C. L., & Smith Neubig, M. 2003,

AJ, 125, 3082, doi: [10.1086/374988](https://doi.org/10.1086/374988)

Bruzual, G., & Charlot, S. 2003, MNRAS, 344, 1000,

doi: [10.1046/j.1365-8711.2003.06897.x](https://doi.org/10.1046/j.1365-8711.2003.06897.x)

- Bunker, A. J., NIRSPEC Instrument Science Team, & JAESs Collaboration. 2020, in IAU Symposium, Vol. 352, Uncovering Early Galaxy Evolution in the ALMA and JWST Era, ed. E. da Cunha, J. Hodge, J. Afonso, L. Pentericci, & D. Sobral, 342–346, doi: [10.1017/S1743921319009463](https://doi.org/10.1017/S1743921319009463)
- Bunker, A. J., Saxena, A., Cameron, A. J., et al. 2023, *A&A*, 677, A88, doi: [10.1051/0004-6361/202346159](https://doi.org/10.1051/0004-6361/202346159)
- Calzetti, D., Armus, L., Bohlin, R. C., et al. 2000, *ApJ*, 533, 682, doi: [10.1086/308692](https://doi.org/10.1086/308692)
- Cameron, A. J., Katz, H., Rey, M. P., & Saxena, A. 2023, *MNRAS*, 523, 3516, doi: [10.1093/mnras/stad1579](https://doi.org/10.1093/mnras/stad1579)
- Carniani, S., Hainline, K., D’Eugenio, F., et al. 2024, *Nature*, 633, 318, doi: [10.1038/s41586-024-07860-9](https://doi.org/10.1038/s41586-024-07860-9)
- Casey, C. M., Akins, H. B., Kokorev, V., et al. 2024, *ApJL*, 975, L4, doi: [10.3847/2041-8213/ad7ba7](https://doi.org/10.3847/2041-8213/ad7ba7)
- Castellano, M., Fontana, A., Treu, T., et al. 2023, *ApJL*, 948, L14, doi: [10.3847/2041-8213/accea5](https://doi.org/10.3847/2041-8213/accea5)
- Castellano, M., Napolitano, L., Fontana, A., et al. 2024, *ApJ*, 972, 143, doi: [10.3847/1538-4357/ad5f88](https://doi.org/10.3847/1538-4357/ad5f88)
- Castellano, M., Napolitano, L., Moreschini, B., et al. 2025, arXiv e-prints, arXiv:2512.08490, doi: [10.48550/arXiv.2512.08490](https://doi.org/10.48550/arXiv.2512.08490)
- Chabrier, G. 2003, *PASP*, 115, 763, doi: [10.1086/376392](https://doi.org/10.1086/376392)
- Chang, S.-J., Gronke, M., Matthee, J., & Mason, C. 2026, *MNRAS*, 545, staf2131, doi: [10.1093/mnras/staf2131](https://doi.org/10.1093/mnras/staf2131)
- Chen, C.-H., Ho, L. C., Li, R., & Zhuang, M.-Y. 2025, *ApJ*, 983, 60, doi: [10.3847/1538-4357/ada93a](https://doi.org/10.3847/1538-4357/ada93a)
- Chen, Y.-X., Liu, H., Li, R., et al. 2026, arXiv e-prints, arXiv:2602.06954, doi: [10.48550/arXiv.2602.06954](https://doi.org/10.48550/arXiv.2602.06954)
- Chisholm, J., Berg, D. A., Boylan-Kolchin, M., et al. 2026, arXiv e-prints, arXiv:2602.15935, <https://arxiv.org/abs/2602.15935>
- Chon, S., Ono, H., Omukai, K., & Schneider, R. 2022, *MNRAS*, 514, 4639, doi: [10.1093/mnras/stac1549](https://doi.org/10.1093/mnras/stac1549)
- Clarke, L., Lam, N., Shapley, A. E., et al. 2026, arXiv e-prints, arXiv:2601.11092, doi: [10.48550/arXiv.2601.11092](https://doi.org/10.48550/arXiv.2601.11092)
- Cleri, N. J., Olivier, G. M., Backhaus, B. E., et al. 2025, *ApJ*, 994, 146, doi: [10.3847/1538-4357/ae0f17](https://doi.org/10.3847/1538-4357/ae0f17)
- Coughlin, E. R., & Begelman, M. C. 2024, *ApJ*, 970, 158, doi: [10.3847/1538-4357/ad5723](https://doi.org/10.3847/1538-4357/ad5723)
- Crowther, P. A. 2007, *ARA&A*, 45, 177, doi: [10.1146/annurev.astro.45.051806.110615](https://doi.org/10.1146/annurev.astro.45.051806.110615)
- Crowther, P. A., & Hadfield, L. J. 2006, *A&A*, 449, 711, doi: [10.1051/0004-6361:20054298](https://doi.org/10.1051/0004-6361:20054298)
- Cullen, F., McLeod, D. J., McLure, R. J., et al. 2024, *MNRAS*, 531, 997, doi: [10.1093/mnras/stae1211](https://doi.org/10.1093/mnras/stae1211)
- Cullen, F., Carnall, A. C., Scholte, D., et al. 2025, *MNRAS*, 540, 2176, doi: [10.1093/mnras/staf838](https://doi.org/10.1093/mnras/staf838)
- Curti, M., D’Eugenio, F., Carniani, S., et al. 2023, *MNRAS*, 518, 425, doi: [10.1093/mnras/stac2737](https://doi.org/10.1093/mnras/stac2737)
- Curtis-Lake, E., Carniani, S., Cameron, A., et al. 2023, *Nature Astronomy*, 7, 622, doi: [10.1038/s41550-023-01918-w](https://doi.org/10.1038/s41550-023-01918-w)
- de Graaff, A., Rix, H.-W., Naidu, R. P., et al. 2025a, *A&A*, 701, A168, doi: [10.1051/0004-6361/202554681](https://doi.org/10.1051/0004-6361/202554681)
- de Graaff, A., Hviding, R. E., Naidu, R. P., et al. 2025b, arXiv e-prints, arXiv:2511.21820, <https://arxiv.org/abs/2511.21820>
- Dekel, A., Sarkar, K. C., Birnboim, Y., Mandelker, N., & Li, Z. 2023, *MNRAS*, 523, 3201, doi: [10.1093/mnras/stad1557](https://doi.org/10.1093/mnras/stad1557)
- Delvecchio, I., Daddi, E., Magnelli, B., et al. 2025, *A&A*, 704, A313, doi: [10.1051/0004-6361/202557164](https://doi.org/10.1051/0004-6361/202557164)
- D’Eugenio, F., Nelson, E., Ji, X., et al. 2025, arXiv e-prints, arXiv:2510.00101, doi: [10.48550/arXiv.2510.00101](https://doi.org/10.48550/arXiv.2510.00101)
- D’Eugenio, F., Juodžbalis, I., Ji, X., et al. 2026a, *MNRAS*, 545, staf2117, doi: [10.1093/mnras/staf2117](https://doi.org/10.1093/mnras/staf2117)
- D’Eugenio, F., Juodžbalis, I., Ji, X., et al. 2026b, *MNRAS*, 545, staf2117, doi: [10.1093/mnras/staf2117](https://doi.org/10.1093/mnras/staf2117)
- Dietrich, M., Hamann, F., Appenzeller, I., & Vestergaard, M. 2003, *ApJ*, 596, 817, doi: [10.1086/378045](https://doi.org/10.1086/378045)
- Dong, X.-B., Wang, J.-G., Ho, L. C., et al. 2011, *ApJ*, 736, 86, doi: [10.1088/0004-637X/736/2/86](https://doi.org/10.1088/0004-637X/736/2/86)
- Donnan, C. T., McLeod, D. J., Dunlop, J. S., et al. 2023, *MNRAS*, 518, 6011, doi: [10.1093/mnras/stac3472](https://doi.org/10.1093/mnras/stac3472)
- Donnan, C. T., Dickinson, M., Taylor, A. J., et al. 2025, *ApJ*, 993, 224, doi: [10.3847/1538-4357/ae0a1f](https://doi.org/10.3847/1538-4357/ae0a1f)
- Draine, B. T. 2006, *ApJ*, 636, 1114, doi: [10.1086/498130](https://doi.org/10.1086/498130)
- Dwek, E. 2016, *ApJ*, 825, 136, doi: [10.3847/0004-637X/825/2/136](https://doi.org/10.3847/0004-637X/825/2/136)
- Eisenstein, D. J., Willott, C., Alberts, S., et al. 2023, arXiv e-prints, arXiv:2306.02465, doi: [10.48550/arXiv.2306.02465](https://doi.org/10.48550/arXiv.2306.02465)
- Eisenstein, D. J., Johnson, B. D., Robertson, B., et al. 2025, *ApJS*, 281, 50, doi: [10.3847/1538-4365/ae1137](https://doi.org/10.3847/1538-4365/ae1137)
- Fei, Q., Fujimoto, S., Brammer, G., et al. 2026, arXiv e-prints, arXiv:2602.12325, doi: [10.48550/arXiv.2602.12325](https://doi.org/10.48550/arXiv.2602.12325)
- Ferland, G. J., Porter, R. L., van Hoof, P. A. M., et al. 2013, *RMxAA*, 49, 137, doi: [10.48550/arXiv.1302.4485](https://doi.org/10.48550/arXiv.1302.4485)
- Fernández, V., Amorín, R., Firpo, V., & Morisset, C. 2024, *A&A*, 688, A69, doi: [10.1051/0004-6361/202449224](https://doi.org/10.1051/0004-6361/202449224)
- Finkelstein, S. L., Bagley, M. B., Arrabal Haro, P., et al. 2022, *ApJL*, 940, L55, doi: [10.3847/2041-8213/ac966e](https://doi.org/10.3847/2041-8213/ac966e)
- Finkelstein, S. L., Bagley, M. B., Ferguson, H. C., et al. 2023, *ApJL*, 946, L13, doi: [10.3847/2041-8213/acade4](https://doi.org/10.3847/2041-8213/acade4)
- Finkelstein, S. L., Bagley, M. B., Arrabal Haro, P., et al. 2025, *ApJL*, 983, L4, doi: [10.3847/2041-8213/adbbd3](https://doi.org/10.3847/2041-8213/adbbd3)

- Furtak, L. J., Zitrin, A., Plat, A., et al. 2023, *ApJ*, 952, 142, doi: [10.3847/1538-4357/acdc9d](https://doi.org/10.3847/1538-4357/acdc9d)
- Gardner, J. P., Mather, J. C., Clampin, M., et al. 2006, *SSRv*, 123, 485, doi: [10.1007/s11214-006-8315-7](https://doi.org/10.1007/s11214-006-8315-7)
- Gardner, J. P., Mather, J. C., Abbott, R., et al. 2023, *PASP*, 135, 068001, doi: [10.1088/1538-3873/acd1b5](https://doi.org/10.1088/1538-3873/acd1b5)
- Gieles, M., Charbonnel, C., Krause, M. G. H., et al. 2018, *MNRAS*, 478, 2461, doi: [10.1093/mnras/sty1059](https://doi.org/10.1093/mnras/sty1059)
- González Delgado, R. M., & Pérez, E. 2000, *MNRAS*, 317, 64, doi: [10.1046/j.1365-8711.2000.03545.x](https://doi.org/10.1046/j.1365-8711.2000.03545.x)
- Greene, J. E., & Ho, L. C. 2005, *ApJ*, 630, 122, doi: [10.1086/431897](https://doi.org/10.1086/431897)
- Greene, J. E., Strader, J., & Ho, L. C. 2020, *ARA&A*, 58, 257, doi: [10.1146/annurev-astro-032620-021835](https://doi.org/10.1146/annurev-astro-032620-021835)
- Greene, J. E., Labbe, I., Goulding, A. D., et al. 2024, *ApJ*, 964, 39, doi: [10.3847/1538-4357/ad1e5f](https://doi.org/10.3847/1538-4357/ad1e5f)
- Greene, J. E., Setton, D. J., Furtak, L. J., et al. 2026, *ApJ*, 996, 129, doi: [10.3847/1538-4357/ae1836](https://doi.org/10.3847/1538-4357/ae1836)
- Gruppioni, C., Béthermin, M., Loiacono, F., et al. 2020, *A&A*, 643, A8, doi: [10.1051/0004-6361/202038487](https://doi.org/10.1051/0004-6361/202038487)
- Hainline, K. N., Johnson, B. D., Robertson, B., et al. 2024a, *ApJ*, 964, 71, doi: [10.3847/1538-4357/ad1ee4](https://doi.org/10.3847/1538-4357/ad1ee4)
- Hainline, K. N., Helton, J. M., Johnson, B. D., et al. 2024b, *ApJ*, 964, 66, doi: [10.3847/1538-4357/ad20d1](https://doi.org/10.3847/1538-4357/ad20d1)
- Hainline, K. N., Maiolino, R., Juodžbalis, I., et al. 2025, *ApJ*, 979, 138, doi: [10.3847/1538-4357/ad9920](https://doi.org/10.3847/1538-4357/ad9920)
- Han, X. H., Hammer, F., Liang, Y. C., et al. 2010, *A&A*, 514, A24, doi: [10.1051/0004-6361/200912475](https://doi.org/10.1051/0004-6361/200912475)
- Harikane, Y., Nakajima, K., Ouchi, M., et al. 2024, *ApJ*, 960, 56, doi: [10.3847/1538-4357/ad0b7e](https://doi.org/10.3847/1538-4357/ad0b7e)
- Harikane, Y., Ouchi, M., Oguri, M., et al. 2023a, *ApJS*, 265, 5, doi: [10.3847/1538-4365/acaaa9](https://doi.org/10.3847/1538-4365/acaaa9)
- Harikane, Y., Zhang, Y., Nakajima, K., et al. 2023b, *ApJ*, 959, 39, doi: [10.3847/1538-4357/ad029e](https://doi.org/10.3847/1538-4357/ad029e)
- Haslbauer, M., Kroupa, P., Zonoozi, A. H., & Haggi, H. 2022, *ApJL*, 939, L31, doi: [10.3847/2041-8213/ac9a50](https://doi.org/10.3847/2041-8213/ac9a50)
- Helton, J. M., Morrison, J. E., Hainline, K. N., et al. 2025a, *arXiv e-prints*, arXiv:2512.19695, doi: [10.48550/arXiv.2512.19695](https://doi.org/10.48550/arXiv.2512.19695)
- Helton, J. M., Rieke, G. H., Alberts, S., et al. 2025b, *Nature Astronomy*, 9, 729, doi: [10.1038/s41550-025-02503-z](https://doi.org/10.1038/s41550-025-02503-z)
- Hsiao, T. Y.-Y., Sun, F., Lin, X., et al. 2025, *arXiv e-prints*, arXiv:2505.03873, doi: [10.48550/arXiv.2505.03873](https://doi.org/10.48550/arXiv.2505.03873)
- Hviding, R. E., de Graaff, A., Miller, T. B., et al. 2025, *A&A*, 702, A57, doi: [10.1051/0004-6361/202555816](https://doi.org/10.1051/0004-6361/202555816)
- Hviding, R. E., de Graaff, A., Liu, H., et al. 2026, *arXiv e-prints*, arXiv:2601.09778, doi: [10.48550/arXiv.2601.09778](https://doi.org/10.48550/arXiv.2601.09778)
- Iani, E., Rinaldi, P., Caputi, K. I., et al. 2025, *ApJ*, 989, 160, doi: [10.3847/1538-4357/ade5a6](https://doi.org/10.3847/1538-4357/ade5a6)
- Ilić, D., Rakić, N., & Popović, L. Č. 2023, *ApJS*, 267, 19, doi: [10.3847/1538-4365/acd783](https://doi.org/10.3847/1538-4365/acd783)
- Inayoshi, K., & Ho, L. C. 2025, *arXiv e-prints*, arXiv:2512.03130, doi: [10.48550/arXiv.2512.03130](https://doi.org/10.48550/arXiv.2512.03130)
- Inayoshi, K., & Maiolino, R. 2025, *ApJL*, 980, L27, doi: [10.3847/2041-8213/adaebd](https://doi.org/10.3847/2041-8213/adaebd)
- Ishibashi, W., Fabian, A. C., Maiolino, R., Gursahani, Y., & Reynolds, C. S. 2025, *MNRAS*, 544, 726, doi: [10.1093/mnras/staf1439](https://doi.org/10.1093/mnras/staf1439)
- Jakobsen, P., Ferruit, P., Alves de Oliveira, C., et al. 2022, *A&A*, 661, A80, doi: [10.1051/0004-6361/202142663](https://doi.org/10.1051/0004-6361/202142663)
- Ji, X., Belokurov, V., Maiolino, R., et al. 2026a, *MNRAS*, 545, staf2110, doi: [10.1093/mnras/staf2110](https://doi.org/10.1093/mnras/staf2110)
- Ji, X., Übler, H., Maiolino, R., et al. 2024, *MNRAS*, 535, 881, doi: [10.1093/mnras/stae2375](https://doi.org/10.1093/mnras/stae2375)
- Ji, X., Maiolino, R., Übler, H., et al. 2025, *MNRAS*, 544, 3900, doi: [10.1093/mnras/staf1867](https://doi.org/10.1093/mnras/staf1867)
- Ji, X., D'Eugenio, F., Juodžbalis, I., et al. 2026b, *MNRAS*, 545, staf2235, doi: [10.1093/mnras/staf2235](https://doi.org/10.1093/mnras/staf2235)
- Johnson, B. D., Leja, J., Conroy, C., & Speagle, J. S. 2021, *ApJS*, 254, 22, doi: [10.3847/1538-4365/abef67](https://doi.org/10.3847/1538-4365/abef67)
- Jones, B. L., Kocevski, D. D., Pacucci, F., et al. 2025, *arXiv e-prints*, arXiv:2510.07376, doi: [10.48550/arXiv.2510.07376](https://doi.org/10.48550/arXiv.2510.07376)
- Juodžbalis, I., Ji, X., Maiolino, R., et al. 2024, *MNRAS*, 535, 853, doi: [10.1093/mnras/stae2367](https://doi.org/10.1093/mnras/stae2367)
- Juodžbalis, I., Marconcini, C., D'Eugenio, F., et al. 2025, *arXiv e-prints*, arXiv:2508.21748, doi: [10.48550/arXiv.2508.21748](https://doi.org/10.48550/arXiv.2508.21748)
- Kaspi, S., Smith, P. S., Netzer, H., et al. 2000, *ApJ*, 533, 631, doi: [10.1086/308704](https://doi.org/10.1086/308704)
- Kido, D., Ioka, K., Hotokezaka, K., Inayoshi, K., & Irwin, C. M. 2025, *MNRAS*, 544, 3407, doi: [10.1093/mnras/staf1898](https://doi.org/10.1093/mnras/staf1898)
- Killi, M., Watson, D., Brammer, G., et al. 2024, *A&A*, 691, A52, doi: [10.1051/0004-6361/202348857](https://doi.org/10.1051/0004-6361/202348857)
- Kocevski, D. D., Onoue, M., Inayoshi, K., et al. 2023, *ApJL*, 954, L4, doi: [10.3847/2041-8213/ace5a0](https://doi.org/10.3847/2041-8213/ace5a0)
- Kocevski, D. D., Finkelstein, S. L., Barro, G., et al. 2025, *ApJ*, 986, 126, doi: [10.3847/1538-4357/adbc7d](https://doi.org/10.3847/1538-4357/adbc7d)
- Kokorev, V., Fujimoto, S., Labbe, I., et al. 2023, *ApJL*, 957, L7, doi: [10.3847/2041-8213/ad037a](https://doi.org/10.3847/2041-8213/ad037a)
- Kokorev, V., Caputi, K. I., Greene, J. E., et al. 2024, *ApJ*, 968, 38, doi: [10.3847/1538-4357/ad4265](https://doi.org/10.3847/1538-4357/ad4265)
- Kokubo, M., & Harikane, Y. 2025, *ApJ*, 995, 24, doi: [10.3847/1538-4357/ae119e](https://doi.org/10.3847/1538-4357/ae119e)
- Kormendy, J., & Ho, L. C. 2013, *ARA&A*, 51, 511, doi: [10.1146/annurev-astro-082708-101811](https://doi.org/10.1146/annurev-astro-082708-101811)
- Korotin, S. A., Andrievsky, S. M., Hansen, C. J., et al. 2015, *A&A*, 581, A70, doi: [10.1051/0004-6361/201526558](https://doi.org/10.1051/0004-6361/201526558)

- Kovačević, J., Popović, L. Č., & Dimitrijević, M. S. 2010, *ApJS*, 189, 15, doi: [10.1088/0067-0049/189/1/15](https://doi.org/10.1088/0067-0049/189/1/15)
- Kovačević-Dojčinović, J., Dojčinović, I., Lakićević, M., & Popović, L. Č. 2025, *A&A*, 694, A289, doi: [10.1051/0004-6361/202450516](https://doi.org/10.1051/0004-6361/202450516)
- Kron, R. G. 1980, *ApJS*, 43, 305, doi: [10.1086/190669](https://doi.org/10.1086/190669)
- Labbé, I., van Dokkum, P., Nelson, E., et al. 2023, *Nature*, 616, 266, doi: [10.1038/s41586-023-05786-2](https://doi.org/10.1038/s41586-023-05786-2)
- Labbé, I., Greene, J. E., Matthee, J., et al. 2024, arXiv e-prints, arXiv:2412.04557, doi: [10.48550/arXiv.2412.04557](https://doi.org/10.48550/arXiv.2412.04557)
- Labbe, I., Greene, J. E., Bezanson, R., et al. 2025, *ApJ*, 978, 92, doi: [10.3847/1538-4357/ad3551](https://doi.org/10.3847/1538-4357/ad3551)
- Lambrides, E., Larson, R., Hutchison, T., et al. 2025, arXiv e-prints, arXiv:2509.09607, doi: [10.48550/arXiv.2509.09607](https://doi.org/10.48550/arXiv.2509.09607)
- Laor, A., Jannuzi, B. T., Green, R. F., & Boroson, T. A. 1997, *ApJ*, 489, 656, doi: [10.1086/304816](https://doi.org/10.1086/304816)
- Larson, R. L., Finkelstein, S. L., Kocevski, D. D., et al. 2023, *ApJL*, 953, L29, doi: [10.3847/2041-8213/ace619](https://doi.org/10.3847/2041-8213/ace619)
- Leitherer, C., Lee, J. C., & Faisst, A. 2019, *AJ*, 158, 192, doi: [10.3847/1538-3881/ab44c0](https://doi.org/10.3847/1538-3881/ab44c0)
- Leja, J., Carnall, A. C., Johnson, B. D., Conroy, C., & Speagle, J. S. 2019, *ApJ*, 876, 3, doi: [10.3847/1538-4357/ab133c](https://doi.org/10.3847/1538-4357/ab133c)
- Leja, J., Johnson, B. D., Conroy, C., van Dokkum, P. G., & Byler, N. 2017, *ApJ*, 837, 170, doi: [10.3847/1538-4357/aa5ffe](https://doi.org/10.3847/1538-4357/aa5ffe)
- Leung, G. C. K., Bagley, M. B., Finkelstein, S. L., et al. 2023, *ApJL*, 954, L46, doi: [10.3847/2041-8213/acf365](https://doi.org/10.3847/2041-8213/acf365)
- Leung, G. C. K., Finkelstein, S. L., Pérez-González, P. G., et al. 2025, *ApJ*, 992, 26, doi: [10.3847/1538-4357/adfcee](https://doi.org/10.3847/1538-4357/adfcee)
- Li, J., Silverman, J. D., Shen, Y., et al. 2025, *ApJ*, 981, 19, doi: [10.3847/1538-4357/ada603](https://doi.org/10.3847/1538-4357/ada603)
- Lin, X., Fan, X., Cai, Z., et al. 2025, arXiv e-prints, arXiv:2507.10659, doi: [10.48550/arXiv.2507.10659](https://doi.org/10.48550/arXiv.2507.10659)
- Llerena, M., Amorín, R., Cullen, F., et al. 2022, *A&A*, 659, A16, doi: [10.1051/0004-6361/202141651](https://doi.org/10.1051/0004-6361/202141651)
- Loiacono, F., Gilli, R., Mignoli, M., et al. 2025, *A&A*, 703, A36, doi: [10.1051/0004-6361/202555946](https://doi.org/10.1051/0004-6361/202555946)
- López-Sánchez, Á. R., & Esteban, C. 2010, *A&A*, 516, A104, doi: [10.1051/0004-6361/200913434](https://doi.org/10.1051/0004-6361/200913434)
- Ma, Y., Greene, J. E., Volonteri, M., et al. 2025a, arXiv e-prints, arXiv:2509.02662, doi: [10.48550/arXiv.2509.02662](https://doi.org/10.48550/arXiv.2509.02662)
- Ma, Y., Greene, J. E., Setton, D. J., et al. 2025b, *ApJ*, 981, 191, doi: [10.3847/1538-4357/ada613](https://doi.org/10.3847/1538-4357/ada613)
- Ma, Z., Egami, E., Zhu, Y., et al. 2026, arXiv e-prints, arXiv:2601.15962, doi: [10.48550/arXiv.2601.15962](https://doi.org/10.48550/arXiv.2601.15962)
- Maiolino, R., Juarez, Y., Mujica, R., Nagar, N. M., & Oliva, E. 2003, *ApJL*, 596, L155, doi: [10.1086/379600](https://doi.org/10.1086/379600)
- Maiolino, R., Marconi, A., Salvati, M., et al. 2001, *A&A*, 365, 28, doi: [10.1051/0004-6361:20000177](https://doi.org/10.1051/0004-6361:20000177)
- Maiolino, R., Scholtz, J., Curtis-Lake, E., et al. 2024, *A&A*, 691, A145, doi: [10.1051/0004-6361/202347640](https://doi.org/10.1051/0004-6361/202347640)
- Maiolino, R., Risaliti, G., Signorini, M., et al. 2025a, *MNRAS*, 538, 1921, doi: [10.1093/mnras/staf359](https://doi.org/10.1093/mnras/staf359)
- Maiolino, R., Uebler, H., D'Eugenio, F., et al. 2025b, arXiv e-prints, arXiv:2505.22567, doi: [10.48550/arXiv.2505.22567](https://doi.org/10.48550/arXiv.2505.22567)
- Marques-Chaves, R., Schaerer, D., Kuruvanthodi, A., et al. 2024, *A&A*, 681, A30, doi: [10.1051/0004-6361/202347411](https://doi.org/10.1051/0004-6361/202347411)
- Martins, F., Schaerer, D., Haemmerlé, L., & Charbonnel, C. 2020, *A&A*, 633, A9, doi: [10.1051/0004-6361/201936963](https://doi.org/10.1051/0004-6361/201936963)
- Marziani, P., Dultzin, D., Sulentic, J. W., et al. 2018, *Frontiers in Astronomy and Space Sciences*, 5, 6, doi: [10.3389/fspas.2018.00006](https://doi.org/10.3389/fspas.2018.00006)
- Matthee, J., Naidu, R. P., Brammer, G., et al. 2024, *ApJ*, 963, 129, doi: [10.3847/1538-4357/ad2345](https://doi.org/10.3847/1538-4357/ad2345)
- Matthee, J., Naidu, R. P., Kotiwale, G., et al. 2025, *ApJ*, 988, 246, doi: [10.3847/1538-4357/ade886](https://doi.org/10.3847/1538-4357/ade886)
- Mazzolari, G., Scholtz, J., Maiolino, R., et al. 2025, *A&A*, 700, A12, doi: [10.1051/0004-6361/202451860](https://doi.org/10.1051/0004-6361/202451860)
- Merlin, E., Santini, P., Paris, D., et al. 2024, *A&A*, 691, A240, doi: [10.1051/0004-6361/202451409](https://doi.org/10.1051/0004-6361/202451409)
- Morales, A. M., Finkelstein, S. L., Arrabal Haro, P., et al. 2025, *ApJ*, 994, 212, doi: [10.3847/1538-4357/ae145c](https://doi.org/10.3847/1538-4357/ae145c)
- Morishita, T., Liu, Z., Stiavelli, M., et al. 2025a, arXiv e-prints, arXiv:2507.10521, doi: [10.48550/arXiv.2507.10521](https://doi.org/10.48550/arXiv.2507.10521)
- Morishita, T., Stiavelli, M., Schuldt, S., & Grillo, C. 2025b, *ApJ*, 979, 87, doi: [10.3847/1538-4357/ad9aa2](https://doi.org/10.3847/1538-4357/ad9aa2)
- Naidu, R. P., Oesch, P. A., van Dokkum, P., et al. 2022, *ApJL*, 940, L14, doi: [10.3847/2041-8213/ac9b22](https://doi.org/10.3847/2041-8213/ac9b22)
- Naidu, R. P., Matthee, J., Katz, H., et al. 2025, arXiv e-prints, arXiv:2503.16596, doi: [10.48550/arXiv.2503.16596](https://doi.org/10.48550/arXiv.2503.16596)
- Nakajima, K., & Maiolino, R. 2022, *MNRAS*, 513, 5134, doi: [10.1093/mnras/stac1242](https://doi.org/10.1093/mnras/stac1242)
- Nakajima, K., Ouchi, M., Isobe, Y., et al. 2023, *ApJS*, 269, 33, doi: [10.3847/1538-4365/acd556](https://doi.org/10.3847/1538-4365/acd556)
- Nakajima, K., Schaerer, D., Le Fèvre, O., et al. 2018, *A&A*, 612, A94, doi: [10.1051/0004-6361/201731935](https://doi.org/10.1051/0004-6361/201731935)
- Nandal, D., & Loeb, A. 2025, arXiv e-prints, arXiv:2507.12618, doi: [10.48550/arXiv.2507.12618](https://doi.org/10.48550/arXiv.2507.12618)
- Netzer, H., & Wills, B. J. 1983, *ApJ*, 275, 445, doi: [10.1086/161545](https://doi.org/10.1086/161545)

- Nikopoulos, G. P., Watson, D., Sneppen, A., et al. 2025, arXiv e-prints, arXiv:2510.06362, doi: [10.48550/arXiv.2510.06362](https://doi.org/10.48550/arXiv.2510.06362)
- Oke, J. B., & Gunn, J. E. 1983, ApJ, 266, 713, doi: [10.1086/160817](https://doi.org/10.1086/160817)
- Östlin, G., Pérez-González, P. G., Melinder, J., et al. 2025, A&A, 696, A57, doi: [10.1051/0004-6361/202451723](https://doi.org/10.1051/0004-6361/202451723)
- Pacucci, F., Ferrara, A., & Kocevski, D. D. 2026, arXiv e-prints, arXiv:2601.14368, doi: [10.48550/arXiv.2601.14368](https://doi.org/10.48550/arXiv.2601.14368)
- Pacucci, F., & Loeb, A. 2024, ApJ, 964, 154, doi: [10.3847/1538-4357/ad3044](https://doi.org/10.3847/1538-4357/ad3044)
- Pacucci, F., & Narayan, R. 2024, ApJ, 976, 96, doi: [10.3847/1538-4357/ad84f7](https://doi.org/10.3847/1538-4357/ad84f7)
- Pacucci, F., Nguyen, B., Carniani, S., Maiolino, R., & Fan, X. 2023, ApJL, 957, L3, doi: [10.3847/2041-8213/ad0158](https://doi.org/10.3847/2041-8213/ad0158)
- Pang, Y., Wang, X., Cheng, C., et al. 2026, arXiv e-prints, arXiv:2602.12548, doi: [10.48550/arXiv.2602.12548](https://doi.org/10.48550/arXiv.2602.12548)
- Pérez-González, P. G., Gil de Paz, A., Zamorano, J., et al. 2003, MNRAS, 338, 508, doi: [10.1046/j.1365-8711.2003.06077.x](https://doi.org/10.1046/j.1365-8711.2003.06077.x)
- Pérez-González, P. G., Rieke, G. H., Villar, V., et al. 2008, ApJ, 675, 234, doi: [10.1086/523690](https://doi.org/10.1086/523690)
- Pérez-González, P. G., Costantin, L., Langeroodi, D., et al. 2023a, ApJL, 951, L1, doi: [10.3847/2041-8213/acd9d0](https://doi.org/10.3847/2041-8213/acd9d0)
- Pérez-González, P. G., Barro, G., Annunziatella, M., et al. 2023b, ApJL, 946, L16, doi: [10.3847/2041-8213/acb3a5](https://doi.org/10.3847/2041-8213/acb3a5)
- Pérez-González, P. G., Barro, G., Rieke, G. H., et al. 2024a, ApJ, 968, 4, doi: [10.3847/1538-4357/ad38bb](https://doi.org/10.3847/1538-4357/ad38bb)
- Pérez-González, P. G., Rinaldi, P., Caputi, K. I., et al. 2024b, ApJL, 969, L10, doi: [10.3847/2041-8213/ad517b](https://doi.org/10.3847/2041-8213/ad517b)
- Pérez-González, P. G., Östlin, G., Costantin, L., et al. 2025, ApJ, 991, 179, doi: [10.3847/1538-4357/adf8c9](https://doi.org/10.3847/1538-4357/adf8c9)
- Pizzati, E., Hennawi, J. F., Schaye, J., et al. 2025, MNRAS, 539, 2910, doi: [10.1093/mnras/staf660](https://doi.org/10.1093/mnras/staf660)
- Porter, R. L., Ferland, G. J., Storey, P. J., & Detisch, M. J. 2012, MNRAS, 425, L28, doi: [10.1111/j.1745-3933.2012.01300.x](https://doi.org/10.1111/j.1745-3933.2012.01300.x)
- Regan, J. A., & Haehnelt, M. G. 2009, MNRAS, 396, 343, doi: [10.1111/j.1365-2966.2009.14579.x](https://doi.org/10.1111/j.1365-2966.2009.14579.x)
- Reines, A. E., Greene, J. E., & Geha, M. 2013, ApJ, 775, 116, doi: [10.1088/0004-637X/775/2/116](https://doi.org/10.1088/0004-637X/775/2/116)
- Reines, A. E., & Volonteri, M. 2015, ApJ, 813, 82, doi: [10.1088/0004-637X/813/2/82](https://doi.org/10.1088/0004-637X/813/2/82)
- Rieke, M. 2020, in IAU Symposium, Vol. 352, Uncovering Early Galaxy Evolution in the ALMA and JWST Era, ed. E. da Cunha, J. Hodge, J. Afonso, L. Pentericci, & D. Sobral, 337–341, doi: [10.1017/S17439213190008950](https://doi.org/10.1017/S17439213190008950)
- Riffel, R., Rodríguez-Ardila, A., & Pastoriza, M. G. 2006, A&A, 457, 61, doi: [10.1051/0004-6361:20065291](https://doi.org/10.1051/0004-6361:20065291)
- Rinaldi, P., Bonaventura, N., Rieke, G. H., et al. 2025, ApJ, 992, 71, doi: [10.3847/1538-4357/adfa10](https://doi.org/10.3847/1538-4357/adfa10)
- Rivera-Thorsen, T. E., Chisholm, J., Welch, B., et al. 2024, A&A, 690, A269, doi: [10.1051/0004-6361/202450359](https://doi.org/10.1051/0004-6361/202450359)
- Roberts-Borsani, G., Treu, T., Shapley, A., et al. 2024, ApJ, 976, 193, doi: [10.3847/1538-4357/ad85d3](https://doi.org/10.3847/1538-4357/ad85d3)
- Ronayne, K., Papovich, C., Kirkpatrick, A., et al. 2025, arXiv e-prints, arXiv:2508.20177, doi: [10.48550/arXiv.2508.20177](https://doi.org/10.48550/arXiv.2508.20177)
- Rusakov, V., Watson, D., Nikopoulos, G. P., et al. 2026, Nature, 649, 574, doi: [10.1038/s41586-025-09900-4](https://doi.org/10.1038/s41586-025-09900-4)
- Sacchi, A., & Bogdán, Á. 2025, ApJL, 989, L30, doi: [10.3847/2041-8213/adf5c8](https://doi.org/10.3847/2041-8213/adf5c8)
- Sana, H., de Mink, S. E., de Koter, A., et al. 2012, Science, 337, 444, doi: [10.1126/science.1223344](https://doi.org/10.1126/science.1223344)
- Sanders, R. L., Shapley, A. E., Topping, M. W., Reddy, N. A., & Brammer, G. B. 2023, ApJ, 955, 54, doi: [10.3847/1538-4357/acedad](https://doi.org/10.3847/1538-4357/acedad)
- Sargent, W. L. W. 1968, ApJL, 152, L31, doi: [10.1086/180172](https://doi.org/10.1086/180172)
- Schaerer, D., Marques-Chaves, R., Xiao, M., & Korber, D. 2024, A&A, 687, L11, doi: [10.1051/0004-6361/202450721](https://doi.org/10.1051/0004-6361/202450721)
- Schaerer, D., & Vacca, W. D. 1998, ApJ, 497, 618, doi: [10.1086/305487](https://doi.org/10.1086/305487)
- Scholtz, J., Maiolino, R., D'Eugenio, F., et al. 2025, A&A, 697, A175, doi: [10.1051/0004-6361/202348804](https://doi.org/10.1051/0004-6361/202348804)
- Shajib, A. J., Treu, T., Melo, A., et al. 2025, A&A, 702, L12, doi: [10.1051/0004-6361/202556281](https://doi.org/10.1051/0004-6361/202556281)
- Shapley, A. E., Sanders, R. L., Topping, M. W., et al. 2025, ApJ, 980, 242, doi: [10.3847/1538-4357/adad68](https://doi.org/10.3847/1538-4357/adad68)
- Shields, G. A., Ludwig, R. R., & Salvander, S. 2010, ApJ, 721, 1835, doi: [10.1088/0004-637X/721/2/1835](https://doi.org/10.1088/0004-637X/721/2/1835)
- Shin, J., Nagao, T., Woo, J.-H., & Le, H. A. N. 2019, ApJ, 874, 22, doi: [10.3847/1538-4357/ab05da](https://doi.org/10.3847/1538-4357/ab05da)
- Shin, J., Woo, J.-H., Nagao, T., Kim, M., & Bahk, H. 2021, ApJ, 917, 107, doi: [10.3847/1538-4357/ac0adf](https://doi.org/10.3847/1538-4357/ac0adf)
- Siebenmorgen, R., Heymann, F., & Efstathiou, A. 2015, A&A, 583, A120, doi: [10.1051/0004-6361/201526034](https://doi.org/10.1051/0004-6361/201526034)
- Smith, K. C., & Howarth, I. D. 1998, MNRAS, 299, 1146, doi: [10.1046/j.1365-8711.1998.01873.x](https://doi.org/10.1046/j.1365-8711.1998.01873.x)
- Stark, D. P., Topping, M. W., Endsley, R., & Tang, M. 2026, in Encyclopedia of Astrophysics, Volume 4, Vol. 4, 453–499, doi: [10.1016/B978-0-443-21439-4.00128-0](https://doi.org/10.1016/B978-0-443-21439-4.00128-0)
- Stark, D. P., Richard, J., Siana, B., et al. 2014, MNRAS, 445, 3200, doi: [10.1093/mnras/stu1618](https://doi.org/10.1093/mnras/stu1618)
- Steinhardt, C. L., Kokorev, V., Rusakov, V., Garcia, E., & Sneppen, A. 2023, ApJL, 951, L40, doi: [10.3847/2041-8213/acdef6](https://doi.org/10.3847/2041-8213/acdef6)

- Sun, W. Q., Naidu, R. P., Matthee, J., et al. 2026, arXiv e-prints, arXiv:2601.20929.
<https://arxiv.org/abs/2601.20929>
- Surace, M., Whalen, D. J., Hartwig, T., et al. 2018, *ApJL*, 869, L39, doi: [10.3847/2041-8213/aaf80d](https://doi.org/10.3847/2041-8213/aaf80d)
- Tanaka, T. S., Akins, H. B., Harikane, Y., et al. 2025, *ApJ*, 995, 21, doi: [10.3847/1538-4357/ae145f](https://doi.org/10.3847/1538-4357/ae145f)
- Tang, M., Stark, D. P., Plat, A., et al. 2025, *ApJ*, 991, 217, doi: [10.3847/1538-4357/adfd57](https://doi.org/10.3847/1538-4357/adfd57)
- Taylor, A. J., Finkelstein, S. L., Kocevski, D. D., et al. 2025a, *ApJ*, 986, 165, doi: [10.3847/1538-4357/add15b](https://doi.org/10.3847/1538-4357/add15b)
- Taylor, A. J., Kokorev, V., Kocevski, D. D., et al. 2025b, *ApJL*, 989, L7, doi: [10.3847/2041-8213/ade789](https://doi.org/10.3847/2041-8213/ade789)
- Temple, M. J., Hewett, P. C., & Banerji, M. 2021, *MNRAS*, 508, 737, doi: [10.1093/mnras/stab2586](https://doi.org/10.1093/mnras/stab2586)
- Topping, M. W., Stark, D. P., Endsley, R., et al. 2022, *ApJ*, 941, 153, doi: [10.3847/1538-4357/aca522](https://doi.org/10.3847/1538-4357/aca522)
- Topping, M. W., Stark, D. P., Senchyna, P., et al. 2024, *MNRAS*, 529, 3301, doi: [10.1093/mnras/stae682](https://doi.org/10.1093/mnras/stae682)
- Torrallba, A., Matthee, J., Pezzulli, G., et al. 2025, arXiv e-prints, arXiv:2510.00103, doi: [10.48550/arXiv.2510.00103](https://doi.org/10.48550/arXiv.2510.00103)
- Trefoloni, B., Ji, X., Maiolino, R., et al. 2025, *A&A*, 700, A203, doi: [10.1051/0004-6361/202452795](https://doi.org/10.1051/0004-6361/202452795)
- Treu, T., Roberts-Borsani, G., Bradac, M., et al. 2022, *ApJ*, 935, 110, doi: [10.3847/1538-4357/ac8158](https://doi.org/10.3847/1538-4357/ac8158)
- Tripodi, R., Martis, N., Markov, V., et al. 2025a, *Nature Communications*, 16, 9830, doi: [10.1038/s41467-025-65070-x](https://doi.org/10.1038/s41467-025-65070-x)
- Tripodi, R., Bradač, M., D'Eugenio, F., et al. 2025b, *ApJL*, 994, L6, doi: [10.3847/2041-8213/ae13a9](https://doi.org/10.3847/2041-8213/ae13a9)
- Trouille, L., Barger, A. J., & Tremonti, C. 2011, *ApJ*, 742, 46, doi: [10.1088/0004-637X/742/1/46](https://doi.org/10.1088/0004-637X/742/1/46)
- Trump, J. R., Arrabal Haro, P., Simons, R. C., et al. 2023, *ApJ*, 945, 35, doi: [10.3847/1538-4357/acba8a](https://doi.org/10.3847/1538-4357/acba8a)
- Übler, H., Maiolino, R., Curtis-Lake, E., et al. 2023, *A&A*, 677, A145, doi: [10.1051/0004-6361/202346137](https://doi.org/10.1051/0004-6361/202346137)
- Umeda, H., Inayoshi, K., Harikane, Y., & Murase, K. 2025, arXiv e-prints, arXiv:2512.04208, doi: [10.48550/arXiv.2512.04208](https://doi.org/10.48550/arXiv.2512.04208)
- Vacca, W. D., & Conti, P. S. 1992, *ApJ*, 401, 543, doi: [10.1086/172085](https://doi.org/10.1086/172085)
- Vanden Berk, D. E., Richards, G. T., Bauer, A., et al. 2001, *AJ*, 122, 549, doi: [10.1086/321167](https://doi.org/10.1086/321167)
- Vanzella, E., Castellano, M., Meneghetti, M., et al. 2017, *ApJ*, 842, 47, doi: [10.3847/1538-4357/aa74ae](https://doi.org/10.3847/1538-4357/aa74ae)
- Vanzella, E., Messa, M., Zanella, A., et al. 2025, arXiv e-prints, arXiv:2509.07073, doi: [10.48550/arXiv.2509.07073](https://doi.org/10.48550/arXiv.2509.07073)
- Venturi, G., Carniani, S., Bertola, E., et al. 2025, arXiv e-prints, arXiv:2512.09996, doi: [10.48550/arXiv.2512.09996](https://doi.org/10.48550/arXiv.2512.09996)
- Verner, E. M., Verner, D. A., Korista, K. T., et al. 1999, *ApJS*, 120, 101, doi: [10.1086/313171](https://doi.org/10.1086/313171)
- Vestergaard, M., & Wilkes, B. J. 2001, *ApJS*, 134, 1, doi: [10.1086/320357](https://doi.org/10.1086/320357)
- Wampler, E. J., & Oke, J. B. 1967, *ApJ*, 148, 695, doi: [10.1086/149194](https://doi.org/10.1086/149194)
- Wang, B., Fujimoto, S., Labbé, I., et al. 2023, *ApJL*, 957, L34, doi: [10.3847/2041-8213/acfe07](https://doi.org/10.3847/2041-8213/acfe07)
- Wang, B., Leja, J., de Graaff, A., et al. 2024, *ApJL*, 969, L13, doi: [10.3847/2041-8213/ad55f7](https://doi.org/10.3847/2041-8213/ad55f7)
- Wang, B., Leja, J., Katz, H., et al. 2025a, arXiv e-prints, arXiv:2508.18358, doi: [10.48550/arXiv.2508.18358](https://doi.org/10.48550/arXiv.2508.18358)
- Wang, B., de Graaff, A., Davies, R. L., et al. 2025b, *ApJ*, 984, 121, doi: [10.3847/1538-4357/adc1ca](https://doi.org/10.3847/1538-4357/adc1ca)
- Weibel, A., Oesch, P. A., Barrufet, L., et al. 2024, *MNRAS*, 533, 1808, doi: [10.1093/mnras/stae1891](https://doi.org/10.1093/mnras/stae1891)
- Williams, C. C., Alberts, S., Ji, Z., et al. 2024, *ApJ*, 968, 34, doi: [10.3847/1538-4357/ad3f17](https://doi.org/10.3847/1538-4357/ad3f17)
- Wills, B. J., Netzer, H., & Wills, D. 1985, *ApJ*, 288, 94, doi: [10.1086/162767](https://doi.org/10.1086/162767)
- Witstok, J., Jones, G. C., Maiolino, R., Smit, R., & Schneider, R. 2023, *MNRAS*, 523, 3119, doi: [10.1093/mnras/stad1470](https://doi.org/10.1093/mnras/stad1470)
- Woods, T. E., Heger, A., & Haemmerlé, L. 2020, *MNRAS*, 494, 2236, doi: [10.1093/mnras/staa763](https://doi.org/10.1093/mnras/staa763)
- Woods, T. E., Agarwal, B., Bromm, V., et al. 2019, *PASA*, 36, e027, doi: [10.1017/pasa.2019.14](https://doi.org/10.1017/pasa.2019.14)
- Yanagisawa, H., Ouchi, M., Golubchik, M., et al. 2026, arXiv e-prints, arXiv:2601.06015, doi: [10.48550/arXiv.2601.06015](https://doi.org/10.48550/arXiv.2601.06015)
- Yue, M., Eilers, A.-C., Ananna, T. T., et al. 2024, *ApJL*, 974, L26, doi: [10.3847/2041-8213/ad7eba](https://doi.org/10.3847/2041-8213/ad7eba)
- Zeimann, G. R., Ciardullo, R., Gebhardt, H., et al. 2015, *ApJ*, 798, 29, doi: [10.1088/0004-637X/798/1/29](https://doi.org/10.1088/0004-637X/798/1/29)
- Zwick, L., Tiede, C., & Mayer, L. 2025, arXiv e-prints, arXiv:2507.22014, doi: [10.48550/arXiv.2507.22014](https://doi.org/10.48550/arXiv.2507.22014)